NEAR-EQUATORIAL DEEP CIRCULATION IN THE INDIAN AND PACIFIC OCEANS

by

Gregory Conrad Johnson

B.S. Bates College
(1985)

Submitted in partial fulfillment of the
requirements for the degree of

Doctor of Philosophy

at the

MASSACHUSETTS INSTITUTE OF TECHNOLOGY

and the

WOODS HOLE OCEANOGRAPHIC INSTITUTION

September 1990

Signature of Author ....
Joint Program in Physical Oceanography
Massachusetts Institute of Technology
Woods Hole Oceanographic Institution
October 2, 1990
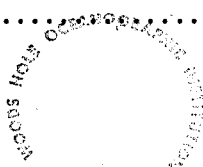
Certified by. ....
Bruce A. Warren
Senior Scientist
Thesis Supervisor

Accepted by.................. ....
Carl Wunsch
Chairman, Joint Committee for Physical Oceanography
Massachusetts Institute of Technology
Woods Hole Oceanographic Institution

NEAR-EQUATORIAL DEEP CIRCULATION IN THE INDIAN AND PACIFIC OCEANS

by

Gregory Conrad Johnson

Abstract

Theory and observations of deep circulation in the near-equatorial Atlantic, Indian and Pacific Oceans are reviewed. Flow of deep and bottom water in the near-equatorial Indian and Pacific oceans, the two oceans with only a southern source of bottom water, is described through analysis of recent CTD data. Zero-velocity surfaces are chosen through use of water-mass properties and transports are estimated. Effects of basin geometry, bottom bathymetry and vertical diffusivity as well as a model meridional inertial current on a sloping bottom near the equator are all discussed in conjunction with the flow patterns inferred from observations.

In the western equatorial Indian Ocean, repeat CTD surveys in the Somali Basin at the height of subsequent northeast and southwest monsoons show only small differences in the strength of the circulation of the bottom water (potential temperature $\theta \leq 1.2°C$). A deep western boundary current (DWBC) carrying about 4×10^6 m^3 s^{-1} of this water is observed moving north along the continental rise of Africa at 3°S. The cross-equatorial sections suggest that the current turns eastward at the equator. The northern sections show a large mass of the coldest water in the interior east of the Chain Ridge, augmenting the evidence that the DWBC observed south of the equator turns east at the equator rather than remaining on the boundary, and feeds the interior circulation in the northern part of the basin from the equator. The circulation of deep water ($1.2°C < \theta \leq 1.7°C$) in the Somali and Arabian Basins is also analyzed. A DWBC flowing southward along the Carlsberg ridge in the Arabian Basin is described.

In the central equatorial Pacific Ocean a recent zonal CTD section at 10°N, allows estimation that 5.0×10^6 m^3 s^{-1} of Lower Circumpolar Water (LCPW, $\theta \leq 1.2°C$) moves northward as a DWBC along the Caroline Seamounts in the East Mariana Basin. In the Central Pacific Basin, 8.1×10^6 m^3 s^{-1} of LCPW is estimated to move northward along the Marshal Seamounts as a DWBC at this latitude. An estimated 4.7×10^6 m^3 s^{-1} of the LCPW moves back southward across 10°N in the Northeast Pacific Basin along the western flank of the East Pacific Rise and an equatorial jet is observed to flow westward from 138°W to 148°W shifting south of the Line Islands at 2.5°S, 159°W. The net northward flow of LCPW across 10°N in the Pacific Ocean is estimated at 8.4×10^6 m^3 s^{-1}. The net southward flow of

the silica-rich North Pacific Deep Water (NPDW, $1.2 < \theta \le 2.0°C$) in the central Pacific Ocean estimated at 2.7×10^6 m^3 s^{-1} is also discussed.

In the Indian Ocean, the eastward equatorial flow in the the bottom water of the Somali Basin differs from the prediction of a flat-bottom uniform-upwelling Stommel-Arons calculation with realistic basin geometry and source location. The behavior of a uniform potential vorticity meridional jet on a sloping bottom is examined in an attempt to explain the observed behavior at the equator. The inertial jet does not cross the equator in a physically plausible fashion owing to the constraint of conservation of potential vorticity. Mass and heat budgets for the bottom water of the Somali Basin are of interest with respect to the equatorial feature. Upwelling through the $\theta = 1.2°C$ surface is estimated at $12 \pm 4 \times 10^{-5}$ cm s^{-1} and a rough heat budget for the deep Somali Basin results in an estimate of vertical diffusivity of 9 ± 5 cm^2 s^{-1} at 3800 m. Numerical model results indicate that large vertical diffusivities result in eastward jets in the bottom water at the equator.

In the Pacific Ocean the DWBC observed flowing northward south of the equator crosses the equator with transport nearly intact, albeit split into two at 10°N by the tortuous bathymetry. However the southward flow along the East Pacific Rise in the Northeast Pacific Basin and the westward equatorial jet this flow feeds are puzzling. The basin depth decreases equatorward and eastward, which may allow some southeastward flow in the Stommel-Arons framework. However, the equatorial jet is still unexplained. The estimated vertical velocity and diffusivity at 3600 db of $2 \pm 2 \times 10^{-5}$ cm s^{-1} and 4 ± 3 cm^2 s^{-1} for the area between 12°S and 10°N are much smaller than estimates in the Somali Basin.

Thus the two oceans, similar in their single southern source of bottom water, have DWBC's which behave remarkably differently near the equator. In the Somali Basin of the Indian Ocean the DWBC appears to turn eastward at the equator, with large vertical upwelling velocity and large vertical diffusivity estimates for the bottom water of the basin. In the Pacific Ocean the DWBC appears to cross the equator, but there is a puzzling westward flowing equatorial jet in the bottom water of the Northeast Pacific Basin.

Thesis Supervisor:
Dr. Bruce A. Warren, Senior Scientist
Woods Hole Oceanographic Institution

Acknowledgments

So many students, faculty, staff, family and friends have made my time spent in the Joint Program and the research and writing of this thesis enjoyable that some regrettably go unnamed here. My advisors; William Young, Nelson Hogg and Bruce Warren (in chronological order) have all given me much support. I have had many useful talks with my thesis committee members; Harry Bryden, Glenn Flierl, Nelson Hogg, Michael McCartney and Bruce Warren. John Toole and Joseph Pedlosky, while not on my committee, were always helpful and willing to talk. George Knapp, Carol MacMurray and Ruth Gorski all lent a hand in data processing and programing. Social and scientific association with many great students here vastly improved the tone of my tenure. Lastly, my wife LuAnne Thompson deserves special thanks for the support she gave me throughout my time here.

I thank Bruce Warren and Don Olson for allowing me to use the CTD data from R.R.S. *Charles Darwin* cruises 86–19 and 87–25, and Harry Bryden and John Toole for making the hydrographic data from R.V. *Moana Wave* cruise 89–3 available for use before publication. Analysis of the data from these two cruises make up the bulk of this thesis. I also thank E. D. Barton and E. A. Hill for making the CTD data they took in the Amirante Passage available, and B. A. Taft, S. P. Hayes, G. E. Frederich and L. A. Codispoti for allowing me to use the CTD data they took at 12°S in the Pacific. Without these two data sets deep heat budgets would have been difficult to make and certainly less accurate. Finally I thank John Toole for bringing the cross-equatorial U.S.-P.R.C. TOGA sections at 165°E to my attention and allowing me to use them, and Rui Ponte for sending me the average zonal velocity profiles for the PEQUOD White Horse stations in the eastern equatorial Pacific. These two data sets helped to make the picture of the circulation of LCPW in the Pacific more complete.

Contents

Chapter 1

Introduction and Literature Review

This thesis examines observational and theoretical aspects of the near-equatorial deep circulation primarily in the western Indian and the central Pacific Oceans. An outline of recent theoretical work on deep interior and boundary flow is presented to put the observations in context. Then a literature review of deep observational work in the western Atlantic (for completeness), the western Indian, and the central Pacific Oceans is given to provide an historical framework for the results and analysis of CTD surveys in the near-equatorial western Indian and central Pacific that follow in subsequent chapters.

1.1 Deep Circulation Theory

By 1960, Stommel and Arons proposed a framework for modeling the deep circulation that stands today (Stommel et. al., 1958; Stommel and Arons, 1960a,b). They assume that the deep circulation of the world oceans is dominated by the effects of sharply localized sinking to form deep and bottom water (in such places as the Weddell, Norwegian-Greenland, and Labrador Seas) balanced by deep upwelling elsewhere. The interior flow satisfies the planetary geostrophic vorticity balance,

$$\beta v = f w_z \, , \tag{1.1}$$

and the kinematic boundary condition on eastern boundaries. Boundary currents of unspecified dynamics are assumed to exist as needed to balance mass on the other boundaries and satisfy the boundary conditions.

1.1.1 Interior Circulation Dynamics

Several simplifications are made within the bounds of the framework above which allow an analytic solution (Stommel and Arons, 1960a,b). The deep water is introduced at point sources. The deep upwelling in the interior is horizontally uniform. The ocean bottom is level and basins are bounded by meridians and parallels. Only the vertically integrated deep circulation is solved for.

These assumptions lead to a slow, broad, poleward flow in the interior, driven by the uniform upwelling (Figure 1.1). The interior flow is supplied by deep western boundary currents (DWBC's) which extend equatorward from high latitude origins. In areas far removed from these sources, such as the North Pacific and Indian Oceans, the DWBC's consist of water from the interior which reaches the northern boundary and turns west then south. These DWBC's flow back toward the high latitude source along the western boundary until they reach a point where they have fed all their water into the interior. At this stagnation point they meet the DWBC flowing in the opposite direction, away from the source. Westward flowing boundary currents on the northern and southern walls return poleward interior flow to the western boundary.

Recently, extensions of these dynamics have been explored. A reduced-gravity shallow-water model is used to investigate deep flow (Kawase, 1987). The model is 1–1/2 layer and inverted, with the active layer on the bottom. The equations are linear, on the equatorial beta plane, with Rayleigh friction in the momentum equations and Newtonian damping in the continuity equation. The introduction of the damping results in upwelling being proportional to the deviation of the interface height from an equilibrium position, rather than the constant assumed in the Stommel-Arons framework. The friction allows for the formation of vorticity dissipating boundary currents (Stommel, 1948). When the damping is small, the interior upwelling is uniform as in Stommel-Arons. However, with a large damping term most of the upwelling occurs on the equator and the eastern boundary. When the DWBC reaches the equator it flows east until it reaches the eastern boundary,
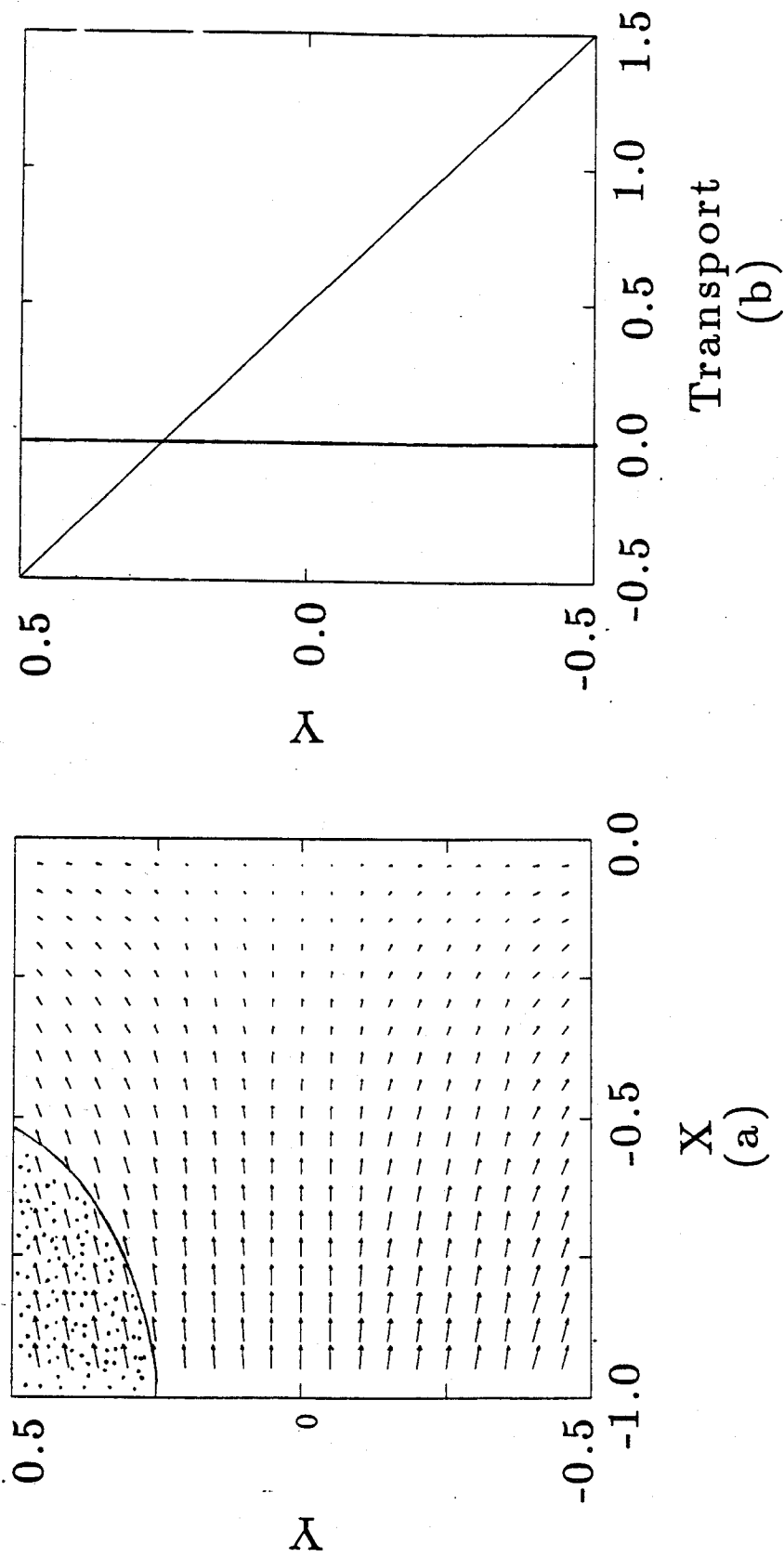
Figure 1.1: Stommel-Arons circulation for a basin centered about the equator bounded by parallels and meridians of equal length on an equatorial β-plane with a unit strength source in the southwest corner. (a) Interior velocity. The stippled portion is fed by southward flowing DWBC. (b) DWBC strength. The DWBC reverses direction in top quarter of the basin. Extra transport is supplied in the north and south by a westward flowing boundary currents at these walls.

where it bifurcates into a pair of northward and southward flowing currents. This pattern of flow trapped to the equator and eastern boundary is a concentration of the interior flow, a result of the Newtonian damping.

Numerical investigations of the deep circulation using the primitive equations with a linear equation of state and multiple layers on a β–plane also yield interesting results near the equator (Suginohara and Fukasawa, 1988). The Stommel-Arons circulation with a northward flowing DWBC is limited to the deepest layers, so the maximum interior upwelling occurs at the top of these layers. In the layers above, where upwelling diminishes with decreasing depth a return circulation with a DWBC moving southward results. The DWBC's maintain a Munk balance. A structure of vertically alternating zonal jets is observed at the equator. The dynamics of these jets is not well understood. However, the use of a stronger vertical diffusivity results in stronger jets.

1.1.2   Deep Western Boundary Current Dynamics

The dynamics of the DWBC's is unspecified in the original Stommel-Arons framework. However, observations of these DWBC's indicate a horizontal scale much larger than a Stommel or Munk boundary layer thickness (Warren, 1981a). Thus, the boundary layers in recent studies (Kawase, 1987; Suginohara and Fukasawa, 1988) do not satisfactorily describe the dynamics of the DWBC's. However, some other attempts have been made to study the physics of these DWBC's in isolation.

An inertial current of uniform potential vorticity on a sloping bottom was first proposed to explain the observed great width of the DWBC's (Stommel and Arons, 1972). The model uses the reduced gravity shallow water equations. The structure is inverted with respect to most 1–1/2 layer models, with the lower layer moving and an upper motionless layer. Potential vorticity and transport are conserved. The current flows equatorward from high latitudes. The evolution of the current with latitude is calculated, and a change in character near the equator found. However,

the model has several weaknesses. The main difficulty is that the conservation of potential vorticity does not allow the DWBC to cross over the equator into the other hemisphere in a realistic fashion. In addition, the formulation is for mid-latitudes. Reformulation of this model on an equatorial β–plane gives a refined description of the meridional evolution of a DWBC conserving potential vorticity and transport (Section 4.2).

Not all equatorward flowing DWBC's exist on a slope, so a model predicting the great width of these currents in the absence of a slope has been introduced (Warren, 1976). The model is applied to the DWBC observed in the SCORPIO section at 28°S in the Pacific, where the abyssal plain is met by the steep Tonga-Kermadec Ridge. The equations used are linear and diffusive, and a pair of nested boundary layers result. The taller narrower one, order 50 km in width, is a mixed balance among horizontal diffusion, planetary vorticity advection and vortex stretching. The wider shorter layer, of order 500 km width, involves a balance between advection of planetary vorticity and vortex stretching. The model does not allow for the study of the evolution of the DWBC with latitude, so the behavior of such a current impinging on the equator is difficult to determine.

1.2 Deep Circulation Observations

A map of bottom potential density anomaly referenced to 4000 db (σ_4, see Appendix A for an explanation) shows plumes of dense bottom water flowing away from its southern sources along western boundaries in the deep basins of the Atlantic, Indian and Pacific Oceans, and its northen source in the Atlantic Ocean (Figure 1.2). This review section discusses recent observational results concerning the circulation of bottom water in the Atlantic, Indian and Pacific Oceans with a focus on the circulation near the equator in these three oceans in the context of an excellent review of the deep circulation of the World Ocean published a decade ago (Warren, 1981a).

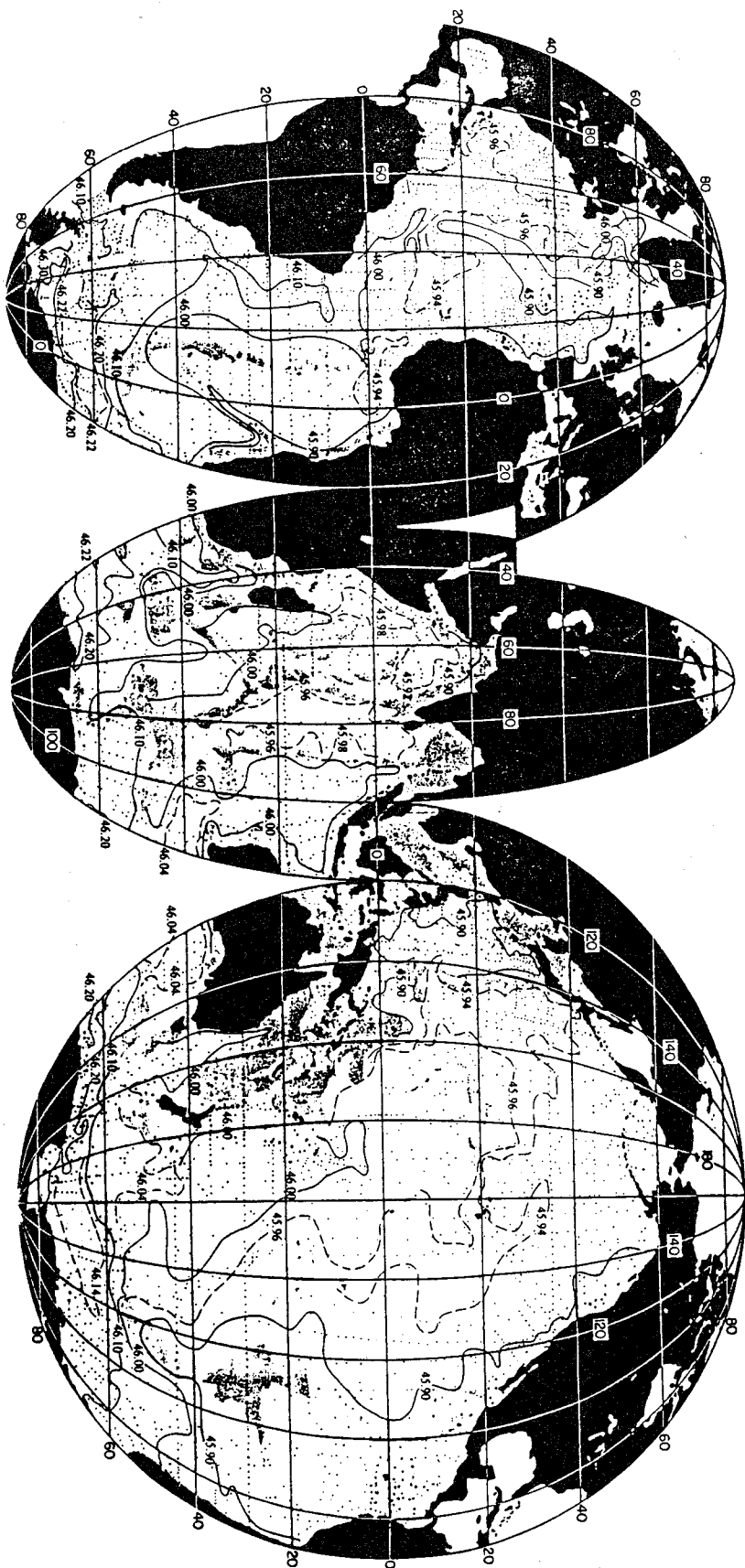The deep circulation of the Atlantic Ocean is perhaps the most complicated of

Figure 1.2: Map of bottom potential density anomaly referenced to 4000 db, σ_4, in kg m^{-3} (see Appendix A for an explanation). Plumes of the densest water flow away from their polar sources along western boundaries of the major deep basins. Dots show station locations and areas shallower than 3.5 km are shaded. From Mantyla and Reid (1983).

the three oceans near the equator, because there are formation regions for deep water in high latitudes at both ends. To the north, flow out of the Norwegian-Greenland Seas and the deep convection in the Labrador Sea make up the North Atlantic Deep Water, (NADW), which flows southward off the east coast of the Americas. In the southern polar regions the Antarctic Bottom Water (AABW) is formed. It mixes with the NADW in the Southern Ocean to form Lower Circumpolar Water (LCPW) before it moves north. This dense water mass flows north under the southward flowing NADW along the western boundary as far as the equator. After crossing the equator the LCPW switches sides, flowing north along the western flank of the Mid-Atlantic Ridge. The Indian Ocean has no northern high-latitude sources of deep water, but is divided into three sets of deep basins by mid-ocean ridges. The deep water is supplied only from the south. Here only circulation in the westernmost set of the Madagascar, Mascarene, Somali and Arabian Basins is discussed. The Pacific, again with no high-latitude northern deep water sources, is also divided into basins by the topography. Here the circulation in the central basins, where the coldest densest waters are located, is examined.

1.2.1 The Atlantic Ocean

The Atlantic Ocean has high latitude deep water sources at both its northern and southern extremes. The deep water from the south, the LCPW, is denser than that from the north, the NADW, and thus the latter rides over the former. The complex behavior of the water masses in the vicinity of the equator is discussed below.

The North Atlantic Deep Water

The NADW originates from the Norwegian-Greenland Sea overflows and deep convection events in the Labrador Sea. This water flows southward from these sources in a DWBC. Upon reaching the equator the current tends to branch, with one branch flowing eastward along the equator, and the other continuing southward

on the western boundary in the South Atlantic. Evidence for this circulation is seen in a map of dissolved oxygen concentration, O_2, with a tongue of oxygen-rich water from the north extending eastward along the equator and southward along the coast of South America (Wüst, 1935). Chlorofluorocarbons corroborate this pattern (Weiss et al., 1985). A recent vertical profile of velocity on the equator compounds the evidence, with strong eastward jets on the equator centered at 1000 and 2000 db (Ponte et al., 1990).

Little more than this is known about the near-equatorial circulation of the NADW. Reliable measurements of the relative magnitudes of the transports and velocities of the two current branches do not exist. Estimates for the southward transport of the DWBC are 19×10^6 m^3 s^{-1} below T= 7°C at 24°N (Schmitz and Richardson, 1990) and about 23×10^6 m^3 s^{-1} below 1200 to 1400 db at various southern latitudes (Wüst, 1957) Other estimates from International Geophysical Year, (IGY), data give a southward transport of 10×10^6 m^3 s^{-1} of NADW in both the North and South Atlantic (Wright, 1969). Thus, the DWBC does not appear to lose transport to the equatorial branch, despite the tracer signal. The problem of cross-equatorial flow in the NADW may be different dynamically from that in the LCPW as described below because the NADW does not sit on the bottom.

The Lower Circumpolar Water

The LCPW rides up along the continental rise of South America below an *in situ* temperature T= 2°C. The thermal wind signature of the DWBC is evident in the slope of the isotherms below this level. Using this level as a zero-velocity surface (ZVS) or level of no motion gives estimated transports of the DWBC rangeing from $5-6 \times 10^6$ m^3 s^{-1} at 32°S and 24°S to a minimum of 1×10^6 m^3 s^{-1} at 16°N with the IGY data (Wright, 1970). North of the equator, the slope of the isopycnals is reversed, as required by geostrophy for a current continuing northward across the equator with the same ZVS. The signal in the thermal wind vanishes by 24°N in the IGY data (Wright, 1970). North of the equator, however, the current is transposed, and rides along the western flank of the Mid-Atlantic Ridge. Other more recent observations

16

north of the equator allow the LCPW to be traced all the way around the western basin with an implied cyclonic circulation (Weatherly and Kelley, 1985).

There are a few possible explanations for this behavior near the equator. The transposed bottom water may be northward interior flow. Another explanation involves the deepening of the western trough of the North Atlantic to the north. This deepening may be sufficient for topographic-β to overcome planetary-β, and effectively turn the eastern boundary into a western boundary, in which case the transposed bottom water may be a DWBC.

1.2.2   The Indian Ocean

The Indian Ocean has no high latitude deep water sources in the north, thus the deep water must originate from the south. This water has the characteristics of LCPW. The movement of this deep water which supplies the slow upwelling and consequent poleward flow in the interior should be apparent in DWBC's in the Indian Ocean. There are two chains of meridional mid-ocean ridges which divide the deep Indian Ocean into three sets of basins, each set with its own southern source of LCPW. The Somali and Arabian Basins are at the end of the westernmost set of basins through which the DWBC flows northward. (See Figures 1.2 and 2.2 for the following discussion). Results of analysis of recent CTD data concerning the circulation of deep and bottom waters in these last two basins are discussed in Chapter 2.

The Madagascar and Mascarene Basins

The flow of cold fresh LCPW from the Crozet Basin into the Madagascar Basin through the Southwest Indian Ridge is discussed using Nansen bottle data taken between 23°S and 32°S on the north side of the ridge (Warren, 1978). A net northwestward transport of 6.1×10^6 m^3 s^{-1} is estimated using a ZVS of 3500 m. The bulk of the northwestward flow, 4×10^6 m^3 s^{-1}, emerges in a current through a large fracture in the ridge.

Farther west between 20°S and 35°S, deep flow crossing the Madagascar Basin from the Southwest Indian Ridge to the coast of Madagascar is examined with CTD data (Swallow and Pollard, 1988). The choice of a 3500 db ZVS results in a net northwestward transport estimate of 5.2×10^6 m^3 s^{-1} below this surface across the basin. The bulk of the water, 3.9×10^6 m^3 s^{-1}, flows northwestward across the basin in a current which originates from the Southwest Indian Ridge at about 30°S and reaches the continental rise off Madagascar at 23°S.

Farther north at the coast of Madagascar, a section of Nansen bottle stations at 23°S reveals the presence of a DWBC in the Madagascar Basin (Warren, 1974). Using a ZVS of 3100 db a net transport of 5.7×10^6 m^3 s^{-1} northward is estimated. The DWBC strength is estimated at 5.2×10^6 m^3 s^{-1}. Using the ZVS of 3100 db with a more recent section of CTD stations at 23°S results in an estimated northward DWBC transport of 3.8×10^6 m^3 s^{-1} and a net transport of 3.6×10^6 m^3 s^{-1} northward (Fieux et al., 1986). This recent section does not extend fully across the basin.

At 16°S in the Mascarene Basin a section of Nansen bottle stations reveals the DWBC. On the basis of water property distributions a variable ZVS is chosen from 1400 db near the coast descending to as low as 4200 db offshore (Warren, 1981b). Below 2000 db an estimated northward transport of 5.2×10^6 m^3 s^{-1} is found on the western side of the basin. Water properties do not help in fixing a ZVS to the east, so transports are not estimated there.

A Nansen bottle section at 12°S in the Mascarene Basin gives evidence for a DWBC there as well (Warren, 1974). A ZVS of 3600 db results in an estimated northward transport of 4.1×10^6 m^3 s^{-1} for the DWBC and 4.4×10^6 m^3 s^{-1} across the section below this surface.

The Amirante Passage

Once the water in this DWBC passes through the Southwest Indian Ridge its northward path through the Madagascar and Mascarene Basins is unobstructed. However to reach the Somali Basin from the Mascarene Basin it must travel through the relatively narrow Amirante Passage. There is geological evidence from bedform and

18

bottom composition that water flows sometimes strongly northward through the passage between 3800 and 4200 m depth (Johnson and Damuth, 1979). These investigators also use nephelometer data taken in the passage showing a relatively high sediment content of the water between 3500 m and the bottom (the deepest passage has a sill depth of perhaps 4500 to 4600 m) to infer, in conjunction with the geological evidence, a fast northward movement of this water from the Mascarene to the Somali Basin.

Estimates of the geostrophic transport of the deep water through the passage are made with CTD station pairs taken in the passage (Fieux and Swallow, 1988). An estimated transport of 0.80–2.05×10^6 m^3 s^{-1} is found below a ZVS of 3800 db. Various schemes to estimate the transport below the deepest common level (DCL) account for the range in the estimate. The DCL is the highest pressure of the shallower station in a station pair, below which geostrophic velocities cannot be calculated. Their best estimate of 1×10^6 m^3 s^{-1} of flow through the passage is disturbingly small with respect to DWBC transport estimates directly to the south. A more recent and closely sampled CTD survey in the passage results in a estimate of $4 \pm 1 \times 10^6$ m^3 s^{-1} flowing northward into the Somali Basin below a ZVS of 3800 db (Barton and Hill, 1989). This estimate preserves continuity with the estimates of transport of the DWBC to the south. The choice of 3800 db as a ZVS restricts inflow to the Somali Basin to waters with potential temperature $\theta \leq 1.2°$C.

The Somali and Arabian Basins

Observations of the path the DWBC takes once it flows through the Amirante passage into the Somali Basin (Warren et al., 1966; Fieux et al., 1986; Schott et al., 1989) are not consistent. However, the Somali Basin is assumed to supply the bottom water of the Arabian Basin (Wyrtki, 1971).

Stations taken during August and September of 1964 reveal a fresh band of water along the coast on maps of salinity, S, on potential temperature, θ, surfaces from 1.8°C to 1.0°C (Warren et al., 1966). This feature indicates the presence of a DWBC moving northeastward in the Somali Basin. Geostrophic velocities and

19

transports are not published in this work, but the slopes of the isotherms in the deep water, tending to fall toward the coast below 2000 m, indicate a northward DWBC with the assumption of a ZVS somewhere above it. This data set was taken with the southwest monsoon well established, and the authors speculated that flow in the deep water might be linked to the seasonal reversal in the Somali current associated with the reversal of monsoon winds. The second set of published data support this speculation. Stations taken in April 1985, after the wane of the northeast monsoon but before the advent of the southwest monsoon indicate a different circulation from that inferred from the 1964 survey (Fieux et. al., 1986). A map of salinity on the $\theta = 1.8°C$ surface shows a wedge of salty water penetrating southward along the coast. Calculations of geostrophic velocity and transport with a ZVS of 2000 db indicate southwestward velocities along the foot of the slope as high as 22 cm s^{-1} in one section and a net westward transport of 3.6x10^6 m^3 s^{-1} in another.

This reversal in circulation and water properties after the monsoons is difficult to link with the surface dynamics because two decades separated the surveys. Between October 1984 and 1986 an array of moorings was set out underneath the Somali Current at the equator. During the second year an instrument was placed at 3000 m depth in about 3500 m of water. This instrument was the only one to record significant four month monsoon seasonal means among 9 instruments placed at 1000, 1500, 2000 and 3000 m depths (Schott et al., 1989). From November 1985 through February 1986 the flow was southwestward at 6.6±2.7 cm s^{-1} at 3000 m depth. From June 1986 through September 1986 the flow was to the northeast at 10.3±1.8 cm s^{-1}. Thus the record shows a seasonal reversal of the deep flow along the western boundary on the equator in the Somali Basin. In addition, salinity is mapped on the $\theta = 1.8°C$ surface using CTD data taken during April 1986. While not so straightforward as the April 1985 data, a similar wedge of salty water penetrates southward on the map (Schott et al., 1989). The results of geostrophic calculations are also slightly more difficult to interpret than those in the prior survey (Fieux, 1988, personal communication).

During INDEX 1979 a few deep moored instruments were put out north of

the equator in the Somali Basin from the middle of May to the middle of June (Quadfasel, 1980). The deep current meter closest to the bottom (2198 m deep in 3851 m of water at about 4°N) started out with little velocity but toward the beginning of June, recorded a speed of about 10–20 cm s^{-1} magnitude flowing to the northeast. While the record is too short to infer any mean circulation, it was in accord with the reversing flow found at 3000 m on the equator. Finally, between 18 and 28 June, 1979, profiles of current were taken on the equator in the Somali Basin with a White Horse instrument. An eastward velocity exceeding 20 cm s^{-1} was observed at 4000 m depth at latitude 47° 10' E (Ponte and Luyten, 1990).

The literature on the deep flow in the Arabian Basin is sparse. While there are no publications on the subject, two atlases do provide some insight into the circulation. In the Oceanographic Atlas of the International Indian Ocean Expedition the sill depth between the Somali Basin and Arabian basin is estimated to be about 3800 m, the depth that the coldest water observed in the Arabian Basin is found in the Somali Basin (Wyrtki, 1971). The relatively homogeneous character of the deep water north of 10°N at and below 3000 m can also be seen in the maps of this atlas. The GEOSECS Indian Ocean Expedition atlas has less coverage, but a more synoptic data set (Spencer et al., 1982). The intrusion of bottom water into the Arabian Basin below 3000 m can be seen in the western Indian Ocean sections.

In summary, deep water flows steadily toward and through the Amirante passage into the Somali Basin. However, hydrographic surveys, current meter arrays, and vertical velocity profiles concentrating on the Somali Basin at and north of the equator indicate that the northward flow of deep water across the equator on the western boundary in the Somali Basin may only occur seasonally, with deep flow north of the equator reversing with the reversal of upper water currents.

1.2.3 The Pacific Ocean

Like the Indian Ocean, the Pacific Ocean has no high-latitude northern sources of bottom water. The bottom water is supplied from the south, and has the char-

acteristics of LCPW. The Pacific Ocean's great size and lack of extreme northern water masses make the water mass contrasts in the deep and bottom water relatively weak north of the equator. Here the peripheral basins will be ignored, and only the literature discussing the central basins, those with the coldest, densest bottom water, will be reviewed. (See Figures 1.2 and 3.1 for following discussion). Results from the analysis of recent CTD data and direct velocity measurements in the deep and bottom waters of the near-equatorial Pacific are discussed in Chapter 3.

The South Pacific

In the South Pacific, the strong northward flow of LCPW along the western boundary is documented at 43°S and 28°S (Warren, 1973). The transport of this DWBC below a ZVS of 2000 db is about 19×10^6 m^3 s^{-1}. Alternatively, an inversion of the same hydrographic data with an initial ZVS of 3500 db results in an estimated deep transport of 14×10^6 m^3 s^{-1} below about 3100 db at 43°S and 3600 db at 28°S (Wunsch et al., 1983). At 22°S a hydrographic section and deep floats are used to set a ZVS ranging from 3100 to 4300 db with a net northward transport of 12.9×10^6 m^3 s^{-1} below (Warren and Voorhis, 1970).

Near the Samoan passage a northward flow of up to 7 cm s^{-1} below a ZVS of about 4000 db is estimated at about 12°S (Reid and Lonsdale, 1974). A more recent thorough survey at about 12°S yeilds an estimate of 12.2×10^6 m^3 s^{-1} moving northward below a ZVS which varies from $\theta = 1.26°$C ($\approx$ 3400 db) at the boundary down to $\theta = 1.22°$C ($\approx$ 3600 db) in the interior (Taft et al., 1990). This choice of ZVS is based on features in the θ–S and θ–O$_2$ curves which reveal salty, oxygen-poor LCPW in high-shear regions near the western boundary below these potential isotherms. The DWBC transport is reduced in magnitude by nearly a factor of two in its northward travel from 43°S to 12°S. Most of this water is presumably lost to interior poleward flow which the DWBC's feed in the Stommel-Arons framework.

The Equatorial Pacific

The determination of the path of the DWBC in the vicinity of the equator is compli-cated in the Pacific by a near-equatorial zonal deep jet at 159°W, 2.5°S and 4000 m with a westward transport of order 6×10^6 m^3 s^{-1} (Firing, 1989). Observations from 138°W to 148°W reveal a westward flowing jet in the bottom water at the equator (Ponte and Luyten, 1989). This current is remarkably similar to that observed at 159°W, and it is possible they are connected, with the shift in latitude induced by the Line Islands as discussed below (Section 3.4). Measurements at 168°E and 179°E near the Gilbert Islands reveal no such structure (Eriksen, 1981), except for a strong southwestward flow measured through a passage at 0° 20'S, 173° 55'E, which is found near strongly variable topography in a deep passage between two seamounts.

The North Pacific

In the North Pacific, topography was thought too complex (Warren, 1981a), and the deep flow too slow (Joyce et al., 1986) to allow observation of a DWBC, al-though the existence of one in the central Pacific Basin is suggested (Edmond et al., 1971). Analysis of a recently acquired trans-Pacific CTD section at 24°N results in a northward transport of 4.9×10^6 m^3 s^{-1} below $\theta = 1.05$°C (≈ 4600 db), most of which occurs in a broad slow flow between 160°E and the dateline (Bryden et al., 1990). However, there is no evidence of a DWBC in the North Pacific data in either the density field or the water mass properties, as this northward flow is spread over 20 degrees of longitude. Evidence for a small (0.4×10^6 m^3 s^{-1}) northward flow east of the Hawaiian Ridge is found in the deep *in situ* temperature field (Edmond et al., 1971).

Farther north, at 35°N, there is no evidence of a DWBC (Kenyon, 1983). How-ever, as in the 24°N section, water of the most extreme southern characteristics is found in the interior near 165°E. In addition, the deep shear indicates that with a mid-depth ZVS the flow in this basin is northward. One speculation for the ab-

sence of a DWBC is that the section may be north of the stagnation point in the Stommel-Arons scheme (Subsections 1.1.1 and 4.1.3) where the DWBC is expected to be weak and southward. Even farther north, the observed flow pattern is of deep westward flow off the Aleutian Islands and eastward flow just to the south. The offshore eastward flow is explained by introducing a topographic effect into the Stommel-Arons framework, so that the westward flow is thought to be the deep northern boundary current (Section 1.1) (Warren and Owens, 1988).

1.3 Deep Circulation Questions

The observational literature does little to clear up questions concerning the near-equatorial deep circulation in any of the the regions discussed. The nature of cross-equatorial flow of the DWBC's remains obscure in all the oceans. In the Atlantic the dynamics and relative magnitude of the equatorial branch of the NADW are unclear. Neither the meridional extent of the branch nor its transport are estimated. The transposition of the LCPW in the equatorial Atlantic could be the signal of the interior flow, of the result of topographic-β effects, or of some other effect. In the Indian Ocean the deep circulation in the Somali Basin may be linked with the seasonal signal of the monsoon, but the paucity of observations makes this assertion tenuous. In the North Pacific Ocean the tortuous bathymetry and low density of hydrographic observations in the tropics has served to obscure the near-equatorial deep circulation. In all three oceans deep equatorial zonal jets are documented.

Theoretical studies leave several questions unanswered concerning the deep circulation, especially in the vicinity of the equator. The dynamics of the DWBC is unclear. The nature of cross-equatorial flow of these DWBC's is not well understood. The dynamics of the deep equatorial zonal jets have yet to be completely explained. These questions are explored below through analysis of recent near-equatorial CTD sections in the western Indian and central Pacific Oceans and in light of some theoretical work.
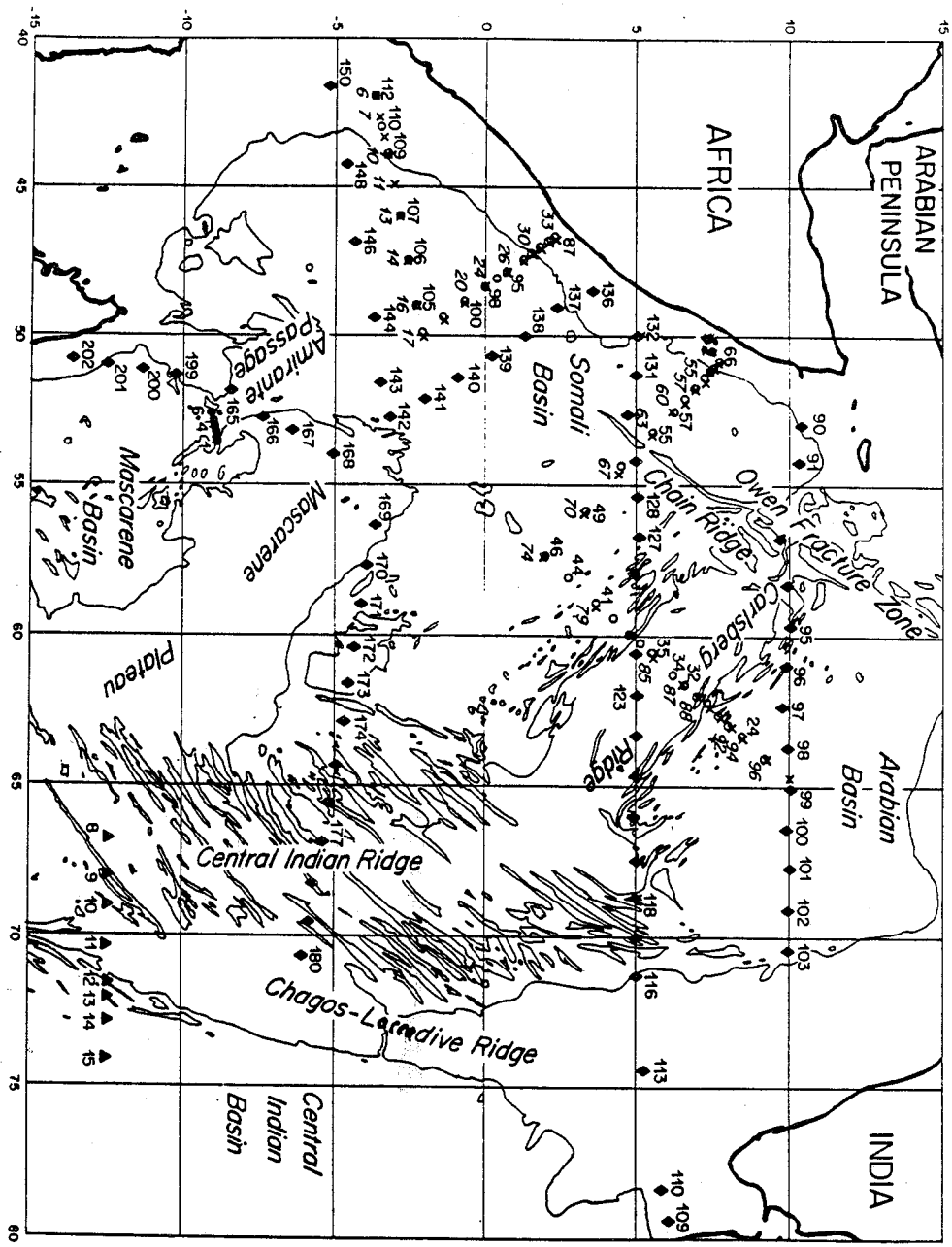
Chapter 2

Indian Ocean Observations

This chapter describes the deep circulation in the Somali and Arabian Basins primarily using recent CTD data taken on the R.R.S. *Charles Darwin* during consecutive northeast (cruise CD 86–19) and southwest (cruise CD 87–25) monsoons. Unpublished historical data taken in the Somali and Arabian Basins by the R.V. *Atlantis II* cruise 8 as a part of the International Indian Ocean Expedition (IIOE) during and after the southwest monsoon in 1963 are available from the National Oceanographic Data Center (NODC) and are useful in describing the deep circulation. While the vertical and horizontal resolution of this data set leaves something to be desired, it augments the description of the bottom water circulation. The southern section of Barton and Hill (1989) in the Amirante Passage is also used. (See Figure 2.1 for station locations).

Other cruises during the IIOE which included deep casts in the region were made by the R.V. *Argo* (cruise Dodo), the R.R.S. *Discovery*, the R.V. *Meteor* and the R.V. *Atlantis II* (cruise 15). The data from the former two cruises are published (Warren et al., 1966). And upon examination both of the latter cruises are inadequate as deep synoptic data sets, important if a possible seasonal signal in the deep circulation is to be detected. The reduced data from the IIOE are presented in an atlas (Wyrtki, 1971).

Figure 2.1: Locations and numbers of CTD stations reaching deeper than $\theta = 1.8°C$ from CD 86-19 (o's, numbers above), CD 87-25 (x's, numbers below), R.V. *Atlantis II* cruise 8 sections used (filled ◇'s), the southern section from CD 87-24 (Barton and Hill, 1989) (•'s) and stations 9-15 from U.S.N.S. *Wilkes* cruise 343907 (filled △'s) (Warren, 1982). The 4000 m isobath is adapted from GEBCO (1984).

ARABIAN PENINSULA

AFRICA

INDIA

Somali Basin

Owen Fracture Zone

Chain Ridge

Carlsberg Ridge

Arabian Basin

Amirante Passage

Mascarene Basin

Mascarene Plateau

Central Indian Ridge

Chagos-Laccadive Ridge

Central Indian Basin

2.1 The Data Set

The R.R.S. *Charles Darwin* recently completed two cruises in the Somali and Arabian Basins with repeat cruise tracks during subsequent monsoons (see Figure 2.2 for deep cruise tracks). Cruise CD 86–19 from Muscat to Mombasa during December 1986 and January 1987 gathered hydrographic data during the northeast monsoon. In the Somali Basin 41 stations reaching deeper than potential temperature $\theta = 1.8°C$ were taken, with an additional 8 in the Arabian Basin. Cruise CD 87–25 during July and August 1987 from Mombasa to Muscat followed roughly the same cruise track under the southwest monsoon. In the Somali Basin 35 stations reaching deeper than $\theta = 1.8°C$ were taken in the Somali Basin and again 8 in the Arabian Basin. Additional shallow stations reaching a maximum pressure of P≤ 1200 db, were taken during both cruises to study aspects of the upper water dynamics and kinematics. These shallow stations will be ignored here.

CTD data were taken with a Neil-Brown CTD fitted with a Beckman polarographic oxygen sensor and bottle samples with a General Oceanics rosette sampler carrying 12 10– *l* Niskin bottles. Natural Environment Research Council technicians measured the water sample salinities, which were standardized using Standard Sea Water batch P104. R. J. Stanley Jr. and G. P. Knapp III performed the oxygen titrations by a modified Winkler method (Knapp and Stalcup, 1987). B. A. Warren edited the water sample data. D. B. Olson, his group and I calibrated the CTD data at the University of Miami, RSMAS (Kearns et al., 1989).

During CD 86–19 wire problems limited the depth of stations to a pressure of about 4600 db during and after station 58. This means that transport estimates made in water deeper than this from station 58 on are biased low owing to a lack of sampling of the deepest water. However, the calibration went well, with deep (P>1500 db) CTD salinity, S, measurements having a precision of ±0.001 psu, and deep CTD dissolved-oxygen concentration, O_2, measurements a precision of ±0.02 *ml l⁻¹*.

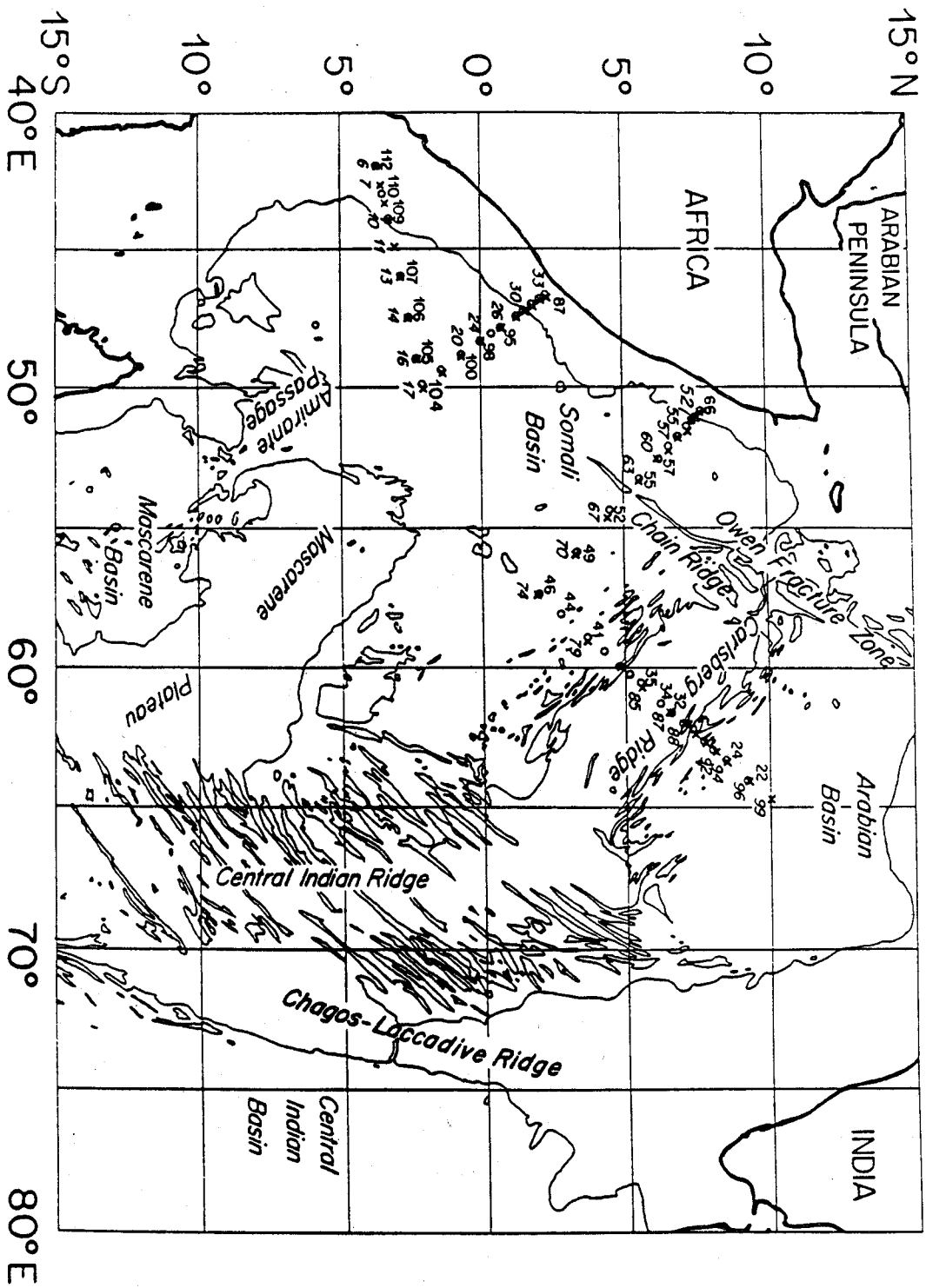The significant problems during CD 87–25 were the loss of three Niskin bottles

27

Figure 2.2: Cruise track for CTD stations reaching deeper than $\theta = 1.8°C$ taken by the R.R.S. *Charles Darwin* on CD 86–19 (omitting stations 73–78, a short section) and CD 87–25 with the 4000 m isobath adapted from GEBCO (1984).

at station 16, an ageing oxygen sensor and the failure of the conductivity cell at station 67. Each of these losses affected the data collection for the remainder of the cruise. Thus the calibration of CD 87–25 is less satisfactory than CD 86–19. Deep CTD salinities have a precision of around ±0.002 psu before the failure of the conductivity cell. Deep CTD dissolved-oxygen concentration measurements have a precision of ±0.04 $ml\ l^{-1}$.

The consistent, linear T–S (T is *in situ* temperature) curve in the deep water of the interior western Indian Ocean north of the equator allows manufacture of an accurate T–S curve for T≤ 3°C using the deep bottle data of stations 52–99 from CD 87–25. A linear least squares fit is applied to the bottle data for these stations for T≤ 3°C. The worst case error in salinity at T= 3°C using the standard deviations for the slope and intercept is ±0.004 psu, assuming the temperature calibrations are perfect. The error decreases with decreasing temperature. The fit is used to construct artificial salinity data for stations 67–99 for T≤ 3°C ($\approx$ 2000 db) for deep dynamic height and potential density calculations. The accuracy of this fit is seen upon examination of the bottle data for stations 52–99 (Figure 2.3).

The southwest monsoon in 1987 was weak in comparison with other years. India suffered a severe drought in 1987, with anomalously weak low-level (850 mb) monsoon winds and with precipitation less than 50% of normal over most of India from April through July (Krishnamurti et al., 1989). During the cruise there were only a few days when the seas approached Beaufort Force 7, and these days were toward the end of the cruise when all of the deep stations had been taken. These events make inferences about the correlation of the deep circulation with the surface forcing difficult. However, the Somali Current was well developed during the cruise, with peak velocities of order 200-250 cm s^{-1} observed with the Acoustic Doppler Current Profiler (D. B. Olson, personal communication 1989).

These difficulties notwithstanding, the data set comprises information of a quality and quantity previously unavailable in the Somali Basin. The R.V. *Argo* and R.R.S. *Discovery* data taken during August and September 1964 comprises 38 Nansen-bottle stations reaching deeper than $\theta = 1.8$°C (Warren et al., 1966, their
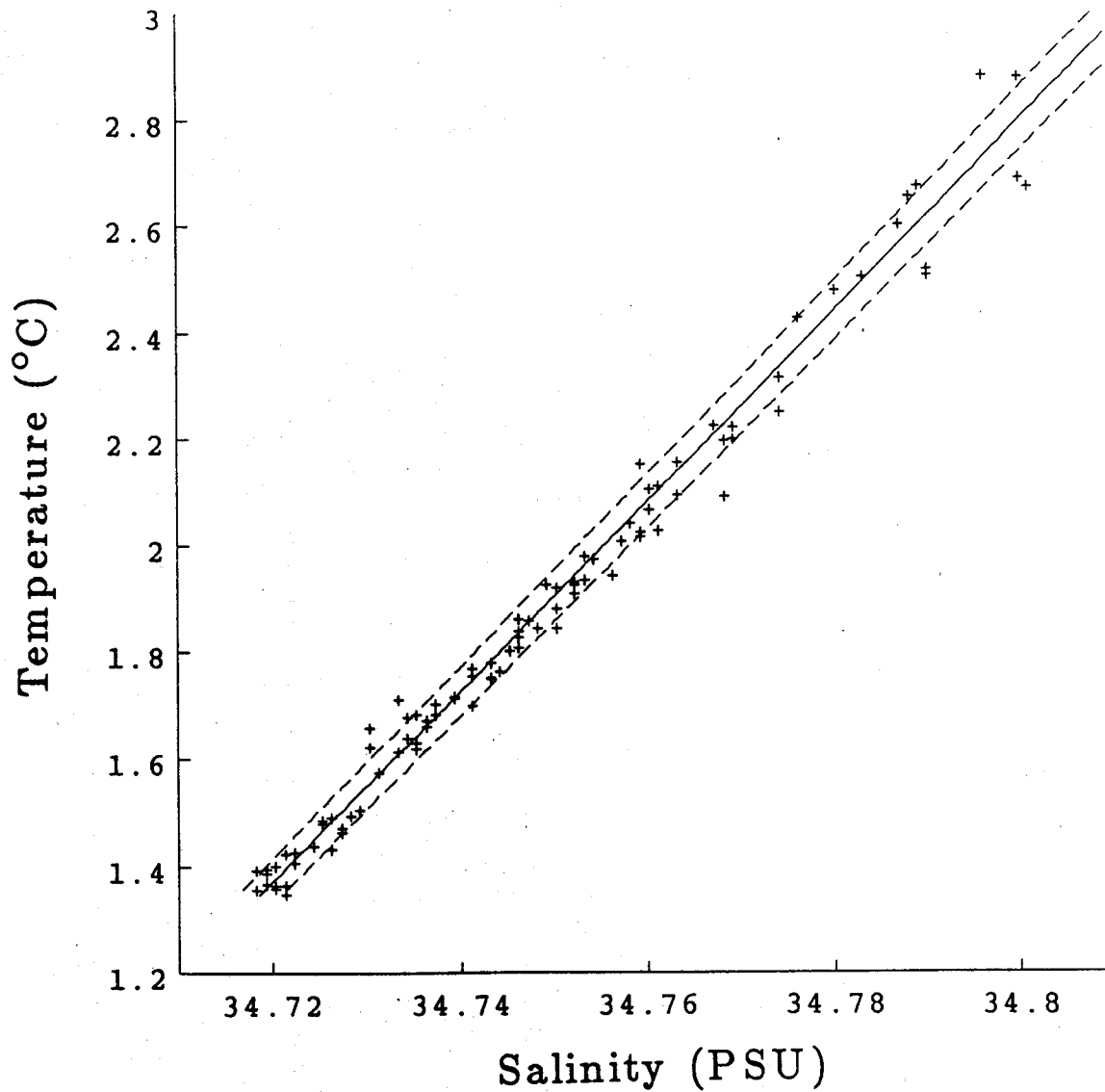
Figure 2.3: Least-squares linear fit (solid line) with standard deviation (dashed lines) for bottle T–S values from CD 87–25 stations 52–99 (crosses). Fit is used in constructing CTD salinity for T≤ 3°C for CD 87–25 stations 67–99. See Figure 2.2 for station locations.

Figure 15). The R.V. *Marion Dufresne* took 22 CTD stations which reached below that potential isotherm in April 1985 (Fieux et al., 1986, their Figure 6), and 21 stations in a similar survey a year later (Schott et al., 1989). The data from the two R.R.S. *Charles Darwin* cruises gives more comprehensive vertical and horizontal coverage in synoptic data sets than that from any previous hydrographic data set.

The stations are divided into four sections for contouring and discussion (Figure 2.2). One short deep section taken during CD 86–19 and not repeated on CD 87–25 does not add to the knowledge of the deep circulation and is not discussed. The southern section extends from Mombasa at roughly 4°S 40°E northeastward to the southern interior of the Somali Basin at roughly 2°S 50°E. The equatorial section extends southeastward from the coast of Somalia at roughly 2.5°N 46.5°E across the equator to the interior end of the southern section at roughly 2°S 50°E. The northern section extends from the Somali Coast at about 8°N 50.5°E southeastward across the Chain Ridge to the northern interior of the Somali Basin at about 2°N 57.5°E. The Carlsberg Ridge section extends southwestward from the interior of the Arabian Basin at 10°N 64°E across the Carlsberg Ridge to the interior end of the northern section at about 2°N 57.5°E.

The deep circulation splits into two layers in the vertical. These different layers are defined by potential temperature classes, which are chosen by θ–S and θ–O_2 characteristics in the region as well as the geographic potential temperature distribution. The bottom water of the Somali Basin is defined as that of $\theta \leq 1.2°$C. The Somali Basin bottom water enters from the south below 3800 db through the Amirante Passage near 9°S, 53°E (Barton and Hill, 1989). There is no horizontal exit for this water, so it is all upwelled and converted into deep water within the basin. The deep water of the Somali Basin and the bottom water of the Arabian Basin are defined as that water of 1.2°C< $\theta \leq 1.7°$C. The lower boundary separates the deep water from the bottom water in the Somali Basin. The upper boundary is determined by water-mass properties and zero-velocity surfaces (ZVS's) which separate the deep water of the Somali Basin and bottom water of the Arabian Basin from that above. Below, it is argued that the Somali Basin deep water is supplied

by the upwelled bottom water below and a deep western boundary current (DWBC) that runs along the Central Indian Ridge to the east. In addition, evidence is presented for a southward flowing DWBC of Arabian Basin bottom water along the Carlsberg Ridge supplied by Somali Basin deep water flowing through the Owen Fracture Zone.

Geostrophic transport estimates are presented for these layers for some of the sections. The ZVS's are not applied on constant pressure surfaces, but on potential isotherms, applying the averaged pressure for the isotherm chosen as the ZVS to each station pair. Transport below the deepest common level (DCL) is estimated by applying the velocity at the DCL of each station pair to the bottom triangle, the right triangular area where the vertical leg is defined by the difference in pressure of the DCL and the greatest pressure of the deeper station and the horizontal leg by the width of the station pair. The extrapolation is a conservative one, and yields a smaller value of transport than would the extrapolation of the shear just above the DCL into the unsampled area. However, in view of the reduced information in the bottom triangle this approximation is appropriate. It is also the same procedure used in all the studies to the south (Subsection 1.2.2).

Hand-contoured section profiles of potential temperature, salinity, dissolved-oxygen concentration and potential density anomaly are prepared for the repeat deep sections. These section profiles are referred to often in the chapter. They can be found in Appendix A, where the procedures used for their production are described.

The circulation of the Somali Basin bottom water is described below section by section from south to north in the Somali Basin. Following this the Somali Basin deep water circulation is discussed in the same order, ending with a description of the Arabian Basin bottom water circulation using the Carlsberg Ridge section.

2.2 The Circulation for $\theta \leq 1.2°C$

Using stations 1–6 of Barton and Hill (1989) (See Figure 2.1 for station locations) and a ZVS of $\theta = 1.2°C$ (about 3800 db) 4×10^6 m^3 s^{-1} is estimated to enter the Somali Basin though the Amirante Passage below the ZVS. The net transport for $1.2°C < \theta \leq 2.2°C$ is only 0.7×10^6 m^3 s^{-1} to the south. There is minimal vertical shear from about 2200–3800 db in this survey of the passage and thus a relative insensitivity of transport estimates below the ZVS to upward shifts in the ZVS. Little or no water above the ZVS appears to be moving northward through the Amirante Passage to renew the Somali Basin deep water. None of the water of $\theta \leq 1.2°C$ entering the basin leaves it without warming, since the coldest water observed in the Arabian Basin in the CD 86–19 and CD 87–25 surveys is of $\theta = 1.24°C$ at station 22 of CD 86–19 and bathymetric charts indicate the region is closed but for the Amirante Passage at least to 4000 m (GEBCO, 1984). The θ–S and θ–O_2 curves for $\theta \leq 1.2°C$ are effectively the same for all the stations taken in the Somali Basin, with salinity increasing and dissolved-oxygen concentration decreasing gradually with increasing potential temperature (Figure 2.4). For $\theta > 1.2°C$ the slopes are greater. Generally salinity increases and dissolved-oxygen concentration decreases to the north and west.

Below it is argued that the bottom water flows northward in a DWBC at 3°S, and appears to branch eastward at the equator, feeding the northern interior from the equator, and not the western boundary (Figure 2.5).

2.2.1 The Southern Section

This geographic uniformity of θ–S and θ–O_2 curves in the bottom water of the Somali Basin supports the choice of ZVS at $\theta = 1.2°C$ for the Amirante Passage transport estimations, since a constant supply of water below this level will suppress horizontal gradients and maintain smaller vertical gradients. In addition transport estimates agree well with those upstream from the Amirante Passage in the Madagascar and Mascarene Basins, which have ZVS's at a slightly higher po-
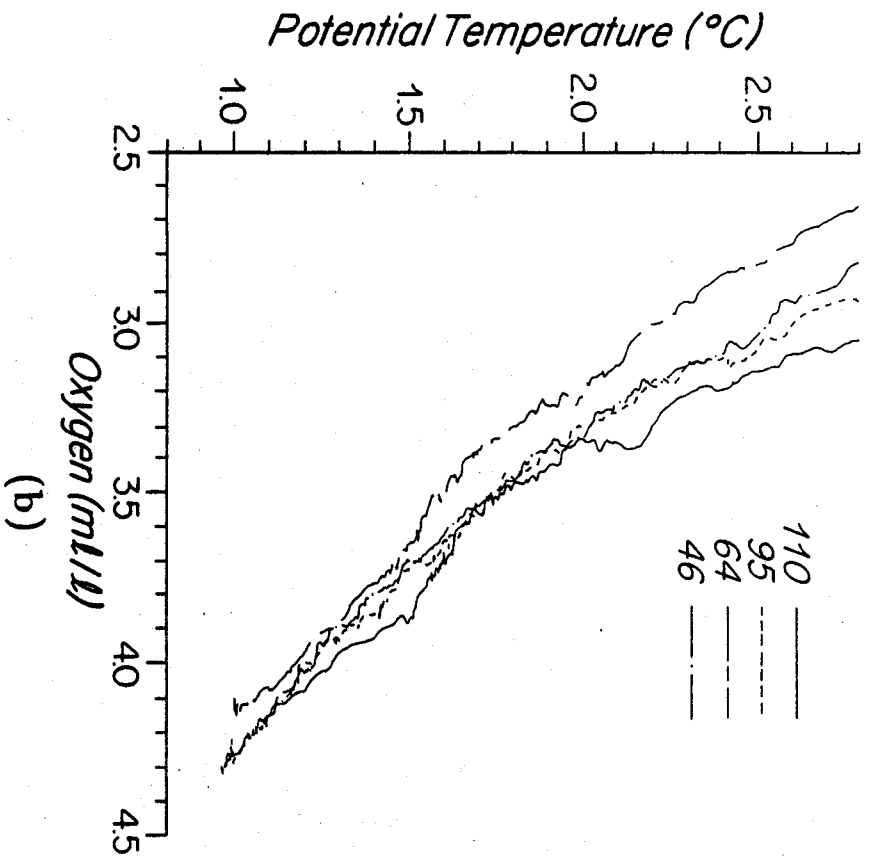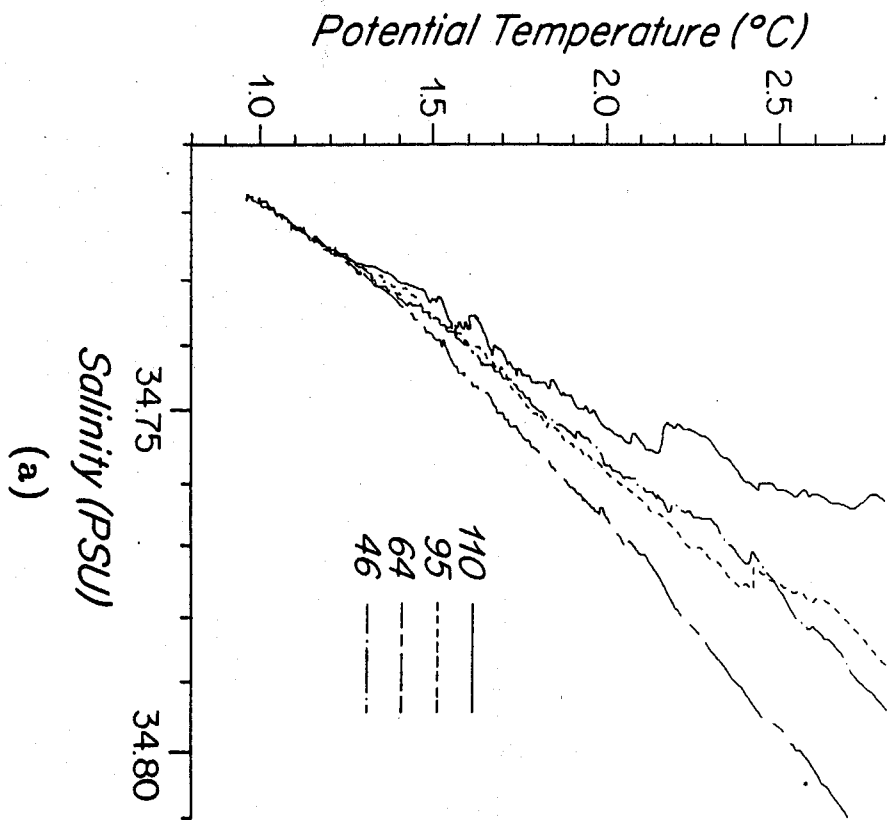
Figure 2.4: Water-mass uniformity for $\theta \leq 1.2°C$ in the Somali Basin. See Figure 2.2 for station locations. Stations from CD 86–89 are used, but there is little difference between these and similar stations from CD 87–25. (a) Deep θ–S curves of stations 110 (solid), 95 (dashed), 64 (chain dashed), and 46 (chain dotted). (b) Deep θ–O_2 curves of the same stations.

34
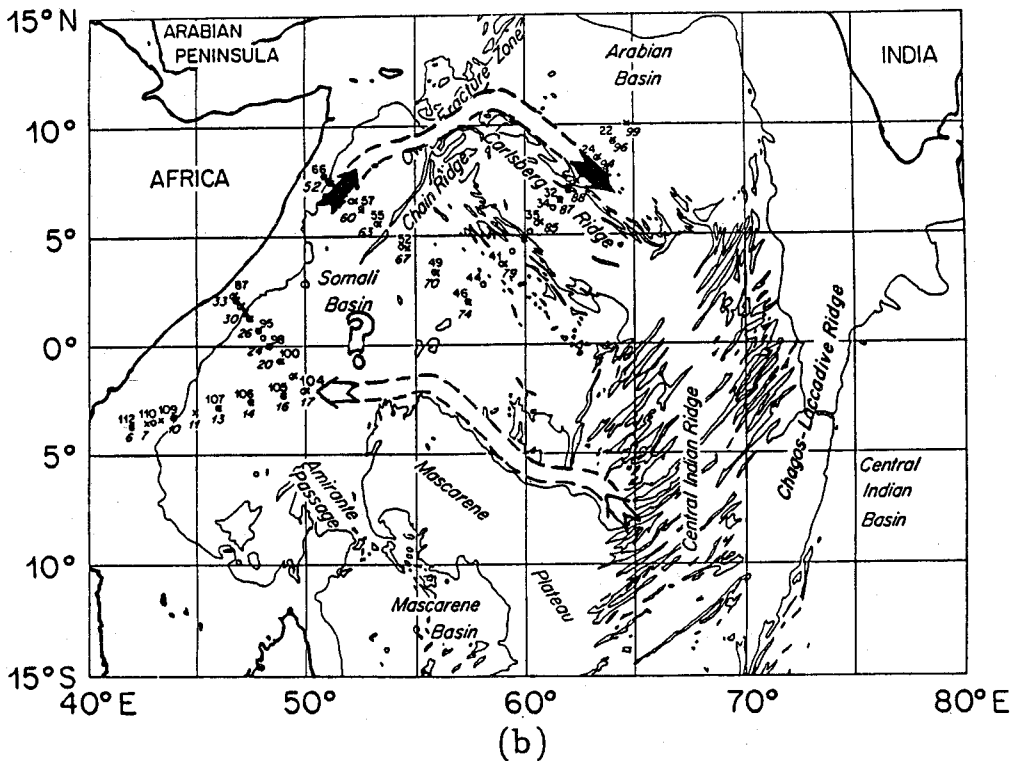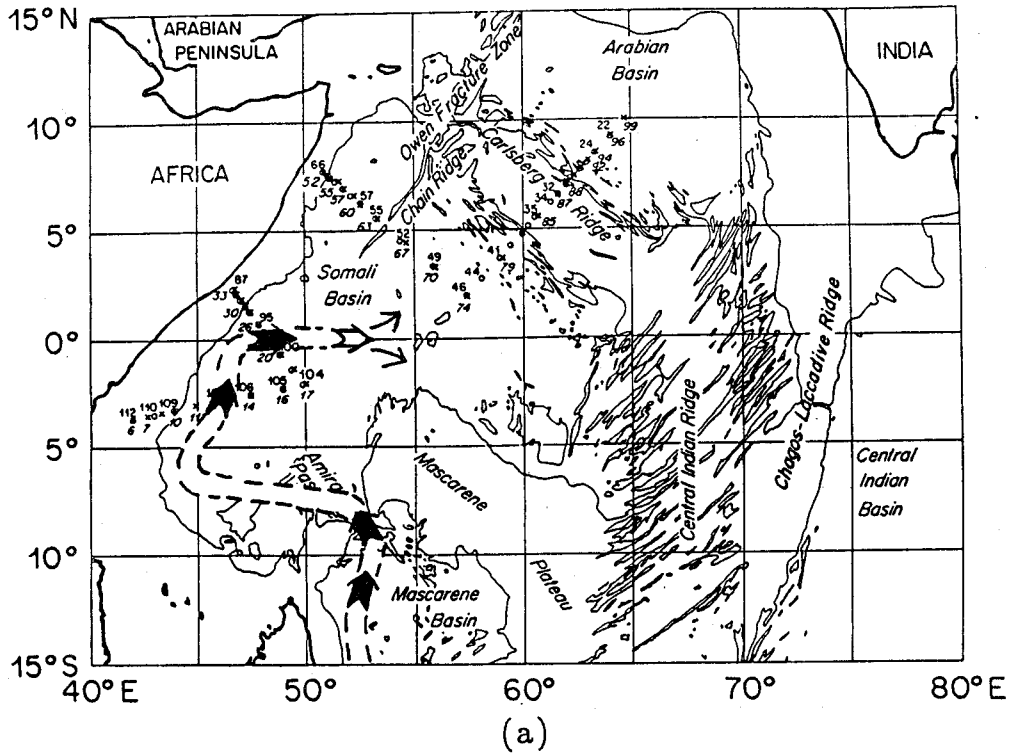
Figure 2.5: (a). Schematic of the circulation in the Somali Basin for $\theta < 1.2°$C. Solid thick arrows are proportional to geostrophic transport estimates, with 4×10^6 m^3 s^{-1} entering the basin through the Amirante Passage. (b). Schematic of the circulation in the Somali and Arabian Basins for $1.2°$C$< \theta \leq 1.7°$C.

tential temperature (Subsection 1.2.2). Below (Section 2.3) it is argued that the deep water of the Somali Basin is supplied from a DWBC to the east and upwelled bottom water from below and not directly from the DWBC to the south.

In the southern section profiles, over the gentle continental rise off of Mombasa, the water property isopleths ride up at the western boundary parallel to the rise, so cold, fresh, oxygen-rich water is found higher up in the water column on the western boundary than in the interior (Figures A.1 through A.4 and A.17 through A.20). Stations 109 and 110 from CD 86–19 show a nearly homogeneous layer of this water with $1.0°C \leq \theta \leq 1.1°C$ about 100 m thick on the rise. This layer is capped by a strongly stratified layer of about 150 m thickness over which a change in potential temperature of 0.4–0.5°C is observed (Figure 2.6). This strong thermal gradient parallel to the sloping bottom in such proximity to the equator indicates a large geostrophic shear. The section profiles from CD 87–25 shows a similar structure in stations 8, 10 and 11, although the homogeneous layer either was not there or was much thinner, within the unsampled bottom 20 m above the rise (Figure 2.6). The deep water-masss properties slightly offshore also ride up on the rise out to about the 5000 m isobath, near the inshore edge of the abyssal plain. This strong density gradient rides up along the continental rise in the southern section profiles, over the water with uniform θ–S and O_2 curves (Figures A.4 and A.20).

The nearly vertically homogeneous layer of water from 20–150 m thick below the region of strong density gradient may be a bottom-boundary layer, well mixed as a result of the high geostrophic velocities in the DWBC. One simple theoretical prediction of the boundary layer thickness h is $h = 0.4u_*/f \approx 140$ m, where the frictional velocity $u_* = 0.03u_g \approx 0.003$ m s^{-1} (Weatherly and Martin, 1978) with the geostrophic velocity outside the layer $u_g \approx 0.1$ m s^{-1} and the Coriolis parameter $f = 8.5 \times 10^{-6}$ s^{-1} (the values calculated at 3.35°S where the boundary layer is observed). A more sophisticated formula for h which takes the effect of ambient stratification outside the bottom boundary layer $N_o^2 = (g/\rho)(\Delta\rho/\Delta z) \approx 4.7 \times 10^{-7}$ s^{-2} into account is $h = 1.3u_*/f(1 + N_o^2/f^2)^{1/4} \approx 40$ m (Weatherly and Martin, 1978). Here the
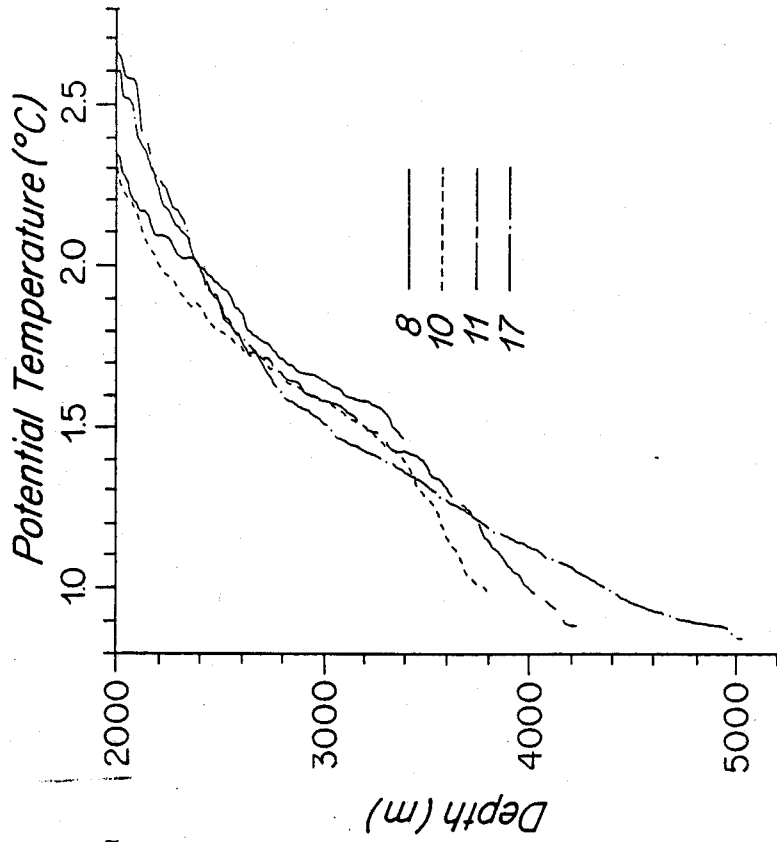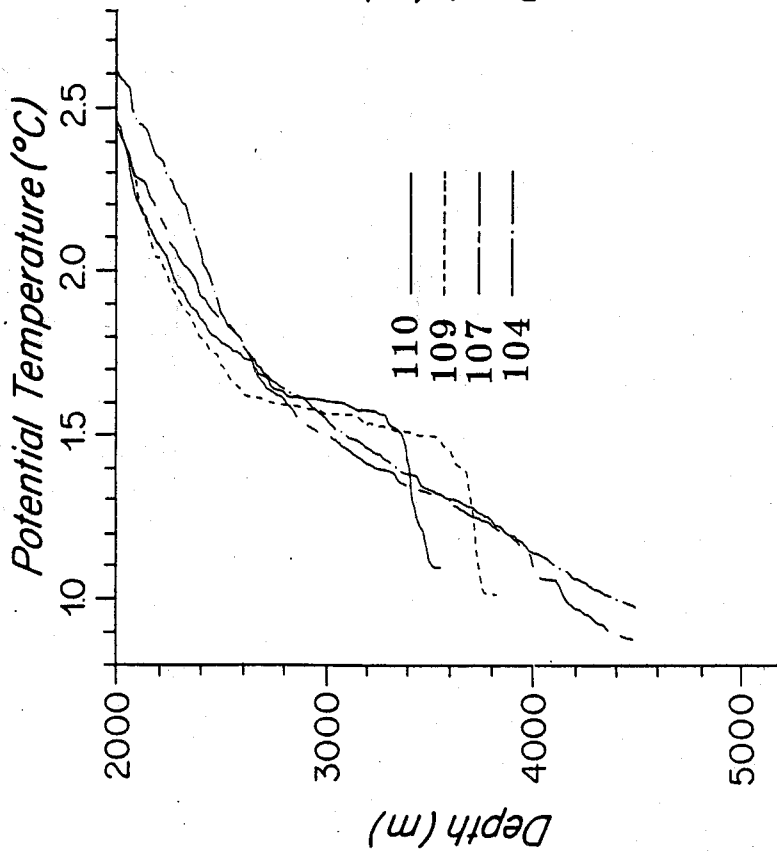
Figure 2.6: Structure of the DWBC riding up along the continent rise south of the equator. Potential temperature plotted against depth for deep stations in the southern sections in the Somali Basin. See Figure 2.2 for station locations. (a) Stations 110 (solid), 109 (dashed), 107 (chain dashed) and 104 (chain dotted) from CD 86–19. (b) Stations 8 (solid), 10 (dashed), 11 (chain dashed), and 17 (chain dotted) from CD 87-25.

37

acceleration due to gravity is $g = 9.8$ m s^{-2}, the ambient density $\rho \approx 1.05$ gm cm^{-3}, and an ambient density change of $\Delta\rho \approx 5\text{x}10^{-5}$ gm cm^{-3} occurs over a depth change of $\Delta z \approx 1000$ m. Thus the observed thickness of the homogenous layer agrees well with theoretical predictions of the thickness of a bottom boundary layer.

The use of $\theta = 1.2°$C as a ZVS for the southern section in the two surveys yields a transport estimate of 3.2x10^6 m^3 s^{-1} northward below $\theta = 1.2°$C for CD 86–19 and 4.6x10^6 m^3 s^{-1} for CD 87–25. The pressure limit of 4600 db imposed on transport estimates by wire problems for the first survey may account for some of the discrepancy. The sections do not extend all the way across the basin, so a net northward transport for the basin can not be estimated. It is notable that the average of the estimates for the two cruises, 3.9x10^6 m^3 s^{-1}, agrees so well with DWBC transport estimates in the Amirante Passage and southward, which use a similar ZVS (Subsection 1.2.2).

2.2.2   The Equatorial Section

The equatorial section forms an enclosed triangle with the southern section and the coast of Africa. The choice of a ZVS might be improved by attempting to balance mass in the area enclosed by these sections. However, with the strong geostrophic shears present near the equator, transport estimates depend crucially upon the choice of ZVS and the level below which transport is estimated. Geostrophic velocity calculations within a degree of the equator are accurate indicators of relative shear over a few hundred meters, but not of velocity over the full water column (Eriksen, 1982). Varying the ZVS by a small amount in the vertical can drastically change the transport estimate for these sections. In the absence of strong indications in the water-mass properties for placing the ZVS and with the lack of full water column accuracy of geostrophic calculations, a mass balance is not attempted.

Transport estimations for the equatorial section using a ZVS of $\theta = 1.2°$C yield a northeastward transport of 0.5x10^6 m^3 s^{-1} for CD 86–19 and 42.0x10^6 m^3 s^{-1} for CD 87–25. Both of these estimates vary wildly as the ZVS is varied slightly. How-

ever, they are both northeastward, and their magnitude exhibits the same temporal trend as that of the southern section, if greatly exaggerated. The geostrophic shear about the equator is symmetric in the deep water within a degree of latitude, and a reversal in shear near 3800–4000 db ($\theta \approx 1.2$–1.1°C) indicates northeastward flow of the water below, giving continuity of ZVS and direction of geostrophic flow with the southern section even though the near-equatorial geostrophic transport estimates are noisy (Figure 2.7).

Step-like features with a vertical scale of about 400 m are present in the deep density field within 1° of the equator (Figures A.8 and A.24). These structures may be the signal of equatorially-trapped deep jets (Eriksen, 1982). Since the section crosses the equator diagonally (Figure 2.2), it is possible (but not likely) that the cross-equatorial symmetry in the density field is simply the result of the sections crossing the axis of the DWBC flowing northeastward along the boundary at the equator. However, this symmetry (Figure 2.7) and the step-like structures in the density field both suggest that the bottom water turns eastward at the equator.

2.2.3 The Northern Section

The northern section profiles from the two cruises show similar deep structure. Once again, this section joins with the Carlsberg Ridge section to form an area that is enclosed, this time at the sill depth of the Owen Fracture Zone. As mentioned above, the area to the north in the Somali Basin is enclosed for $\theta \leq 1.2^\circ$C. As in the equatorial section, the use of $\theta = 1.2^\circ$C as a ZVS results in wildly different transports for the two surveys. Because of eddy noise and lack of a strong signal, changing the ZVS slightly also changes the transport markedly. Since once again there is little guidance in the water-mass properties for setting a ZVS, and the expected signal is a weak interior flow here (Section 1.1), transport estimates are not made for the layer below $\theta = 1.2^\circ$C on this section.

One indication of the circulation of the water of $\theta \leq 1.2^\circ$C in the northern section profiles is the presence of more cold, dense water to the east of the Chain
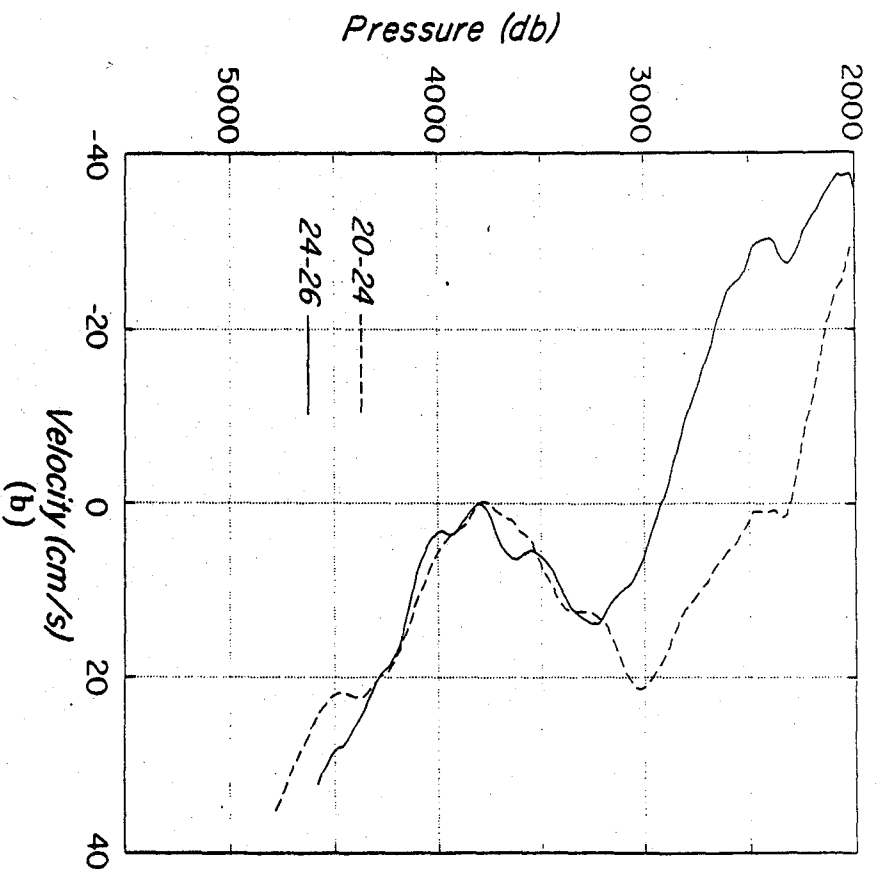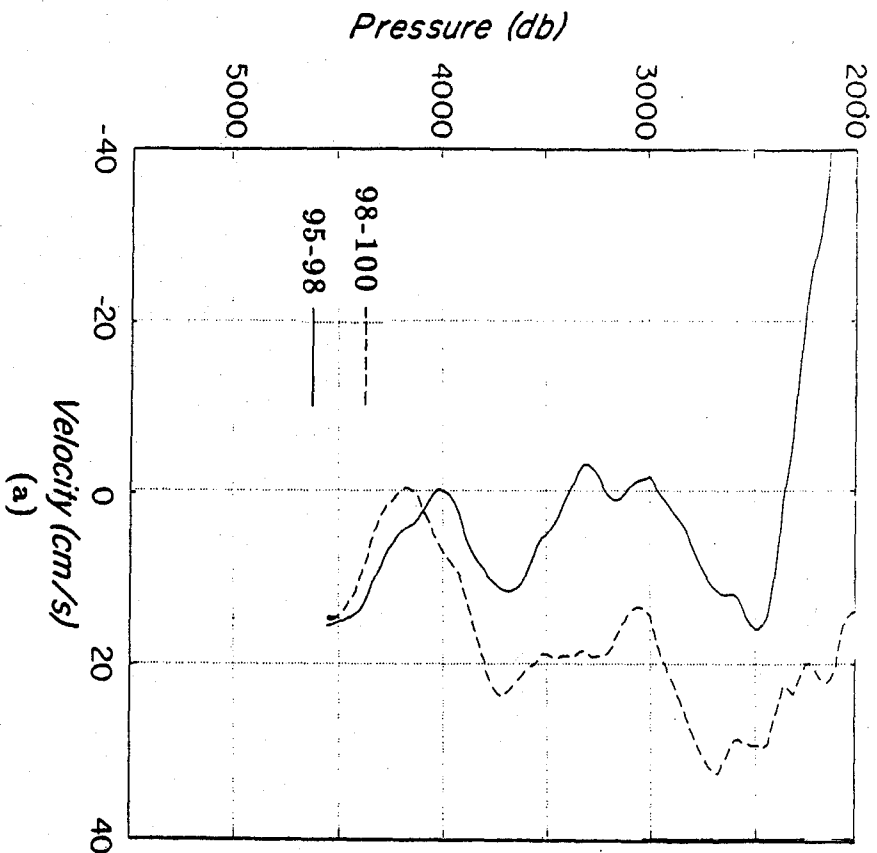
Figure 2.7: Deep geostrophic velocities for station pairs each with one station on the equator show cross-equatorial symmetry near the bottom. See Figure 2.2 for station locations. (a) Station pairs 95–98 and 98–100 from CD 86–19. (b) Station pairs 20–24 and 24–26 from CD 87–25.

Ridge than near the western boundary (Figures A.12 and A.28). Examination of potential temperature against depth reveals this trend with stations 52 and 49 from CD 86–19 and 67 and 70 from CD 87–25 being colder than those inshore below 4100 m (Figure 2.8). The presence of the coldest water in the interior below about 4100 m is consistent with the DWBC turning east near the equator, as the symmetric geostrophic signal in the deep equatorial section suggests, with some water branching off of this zonal flow to feed the densest water into the northern interior. Another indication that the DWBC does not penetrate to the northern reaches of the basin is that the values of dissolved-oxygen concentration west of the Chain ridge are the lowest in the basin for $\theta \leq 1.2°C$ (Station 64 in Figure 2.4 and stations 62 and 58 in Figure 2.11).

2.2.4 Summary of Circulation for $\theta \leq 1.2°C$

The circulation in the layer of $\theta \leq 1.2°C$ is summarized as follows (Figure 2.5). About 4×10^6 m^3 s^{-1} enters the Somali Basin through the Amirante Passage. This current moves to the western boundary between the passage and 3.5°S, where it is observed to carry about the same amount of water northward in a DWBC with the same choice of ZVS in both southern sections. The current turns east at the equator, consistent with the presence of the coldest water east of the Chain Ridge in the interior to the north. If there is a DWBC in the bottom water in the northern section it is too small to be observed in the density field in the presence of eddy noise. This circulation is different from that predicted by a Stommel-Arons calculation in the Somali Basin with uniform upwelling at the top of the bottom water (Subsection 4.1.2).

A historical map of dissolved-oxygen concentration at 4000 m (Wyrtki, 1971 p. 150) is consistent with the observed circulation scheme for the bottom water outlined above. Dissolved-oxygen concentration is highest in the vicinity of the Amirante Passage, and lowest in the east along the equator and in the northwest where the water should be oldest. The dissolved-silica concentration section profile
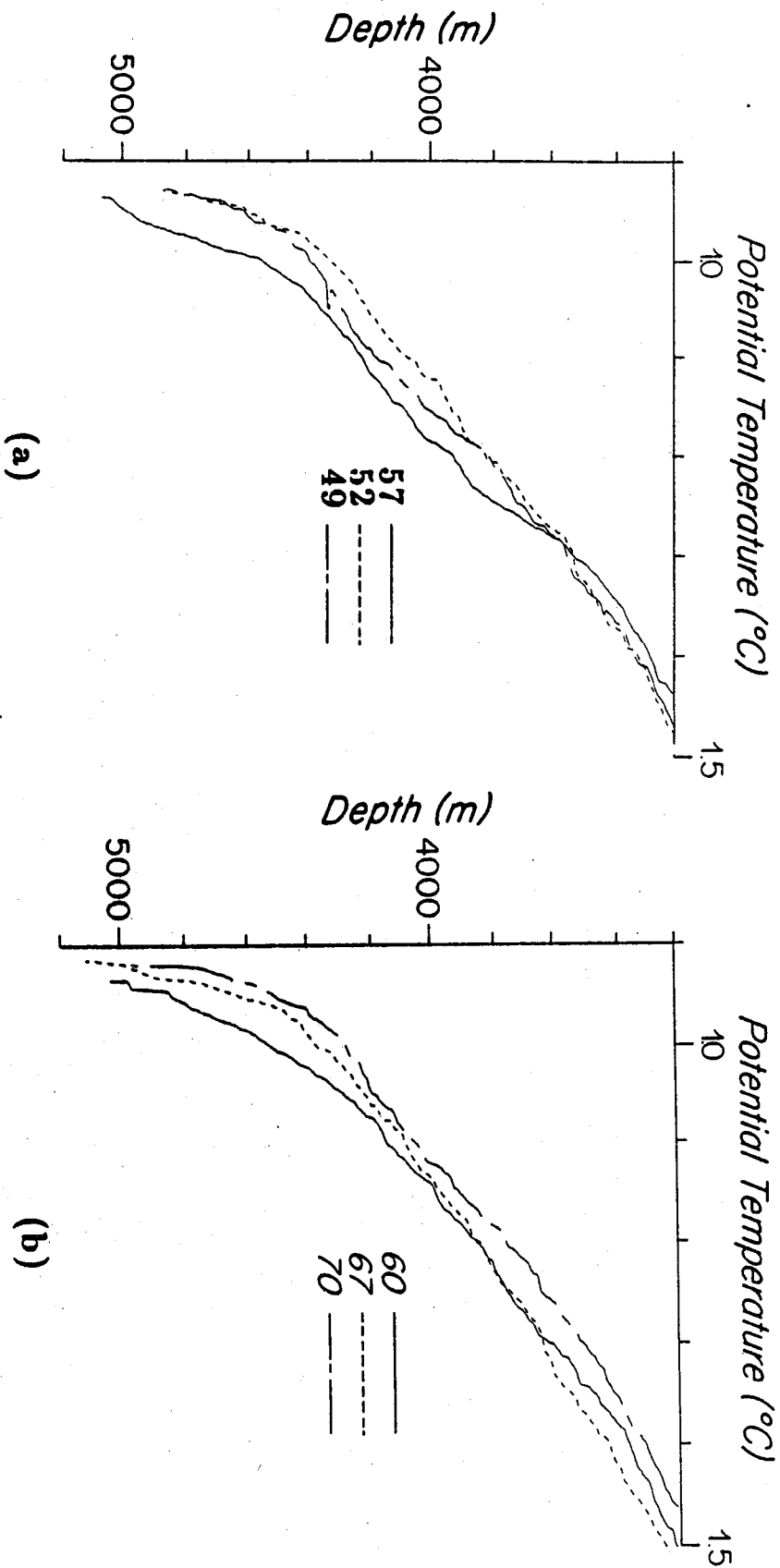
Figure 2.8: Profiles of potential temperature against depth for selected stations from the northern sections showing the large mass of cold dense water east of the Chain Ridge. See Figure 2.2 for station locations. (a) Stations 57 (solid) on the western side of the ridge, and 52 (dashed) and 49 (chain dashed) on the eastern side from CD 86–19. (b) Stations 60 (solid) on the western side and, 67 (dashed) and 70 (chain dashed) on the eastern side from CD 87–25.

from the western Indian Ocean GEOSECS data is also in agreement with the supply of water to the basin being at this depth, with silica-poor water of southern origin appearing only in the bottom water, strongest south of the equator (Spencer et al., 1982 plate 13).

2.3 The Circulation for $1.2°C< \theta \le 1.7°C$

The water of $1.2°C< \theta \le 1.7°C$ is the Somali Basin deep water and the Arabian Basin bottom water. It is suggested below that the Somali Basin deep water is not supplied directly through the Amirante Passage but originates from the east from a branch of the DWBC flowing northward along the Central Indian Ridge (Figure 2.5) and from below upwelled from the bottom water. The Arabian Basin bottom water is shown to flow southeastward in a DWBC on the flank of the Carlsberg Ridge. This circulation pattern along with other evidence argues that Arabian Basin bottom water is supplied by Somali Basin deep water which flows through the Owen Fracture Zone at about 11°N, 57°E, and not from the Central Indian Basin though the other possible Arabian Basin bottom water entrance, the gap in the Chagos-Laccadive Ridge near 3°S, 73°E.

2.3.1 The Southern Section

The origin of the deep water in the southern Somali Basin is different from that of the bottom water. The deep water appears to have two sources. The bottom water entering the basin through the Amirante Passage must exit by upwelling into the deep water, thus providing one source. However, there is a fresh oxygen-rich bend in the θ–S and θ–O_2 curves for the water from $1.2°C< \theta \le 1.7°C$ south of the equator which provides information on another source (Figure 2.9). The values of salinity at $1.2°C< \theta \le 1.7°C$ offshore in the southern section are too fresh to come from the Amirante Passage to the south according to comparisons with CTD casts taken there recently (Barton and Hill, 1989). In addition, using a ZVS of $\theta = 1.2°C$ and their stations 1–6 across the passage from CD 87-24 gives a net

southward transport of 0.7x10^6 m^3 s^{-1} for 1.2°C< θ ≤ 2.2°C (about 2200–3800 db). However, there is a DWBC that runs northward along the Central Indian Ridge at this depth. This current is sufficiently fresh and oxygen-rich to provide this signal in the water-mass properties seen in the southern section data (Figure 2.9) and carries an estimated 6x10^6 m^3 s^{-1} of water northward at 18°S between 2400–3600 db and 3x10^6 m^3 s^{-1} of water northward at 12°S between 1800 and 2800–3800 db (Warren, 1981b and 1982). This latter estimate provides an upper bound on the volume transport of the deep water entering the Somali Basin from this source, since the DWBC there presumably supplies the Central Indian Basin as well as the Somali Basin (Warren, 1982).

Maps of salinity and dissolved-oxygen concentration at 3000 m provide evidence that this fresh, oxygen-poor DWBC running northward along the Central Indian Ridge branches westward north of 12°S, with that branch flowing along the Mascarene Plateau into the interior of the Somali Basin (Wyrtki, 1971 pp. 143 and 144). The fact that the freshest and most oxygen-rich water in this potential temperature range is found in the southern section data off the coast closest to the Mascarene Plateau rather than against the western boundary as it would be if originating from the south reinforces the argument for this circulation pattern. Thus this component of the Somali Basin deep water appears to enter from the east, not the south. If the flow is to be consistent with the Stommel-Arons framework for the deep circulation this deep water should flow from its eastern source to the western boundary in a zonal jet (Warren, 1982).

2.3.2   The Equatorial Section

Curves of θ–S bend fresh from 1.2°C< θ ≤ 2.2°C in the interior from just north of the equator to the southern end of the sections. This bend is a result of the fresh water supplied from the east, along the Mascarene ridge, as described for the southern sections above. Northward toward the coast this freshness disappears. The increase in salinity occurs in the deeper water in the interior, but gradually

44
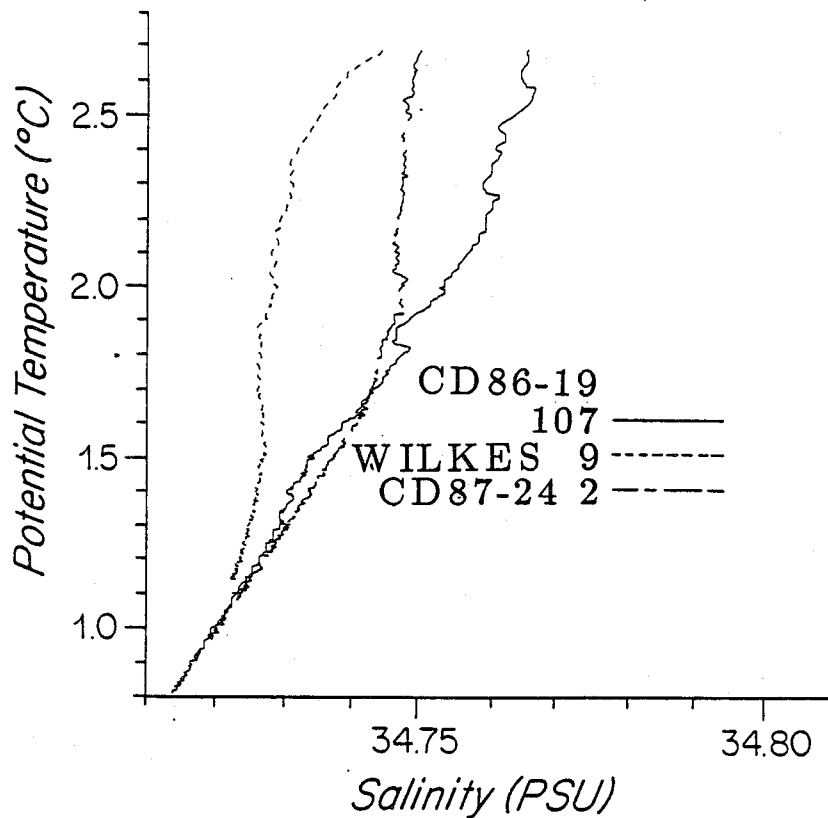
Figure 2.9: θ–S for the deep water of the Somali Basin, CD 86–19 station 107 at 2° 50'S 68°E (solid line); the Amirante Passage, CD 87–24 station 2 at 8° 57'S 53° 24'E (Barton and Hill, 1989) (chain dashed line); and the DWBC of the Central Indian Ridge, U.S.N.S. *Wilkes* cruise 343907, station 9 at 12°S 46°E (Warren, 1982) (Dashed line). See Figure 2.1 for station locations.

rises to eliminate the entire fresh bend near the coast. This trend is seen in stations 95 to 88 for CD 86–19 and 26 to 33 for CD 87–25 (Figure 2.10). The same trend is revealed to a lesser extent in θ–O_2. This feature indicates at most a sluggish cross-equatorial northward flow in the deep water off of the continental rise just north of the equator. Because the saltiness does not extend to the southern section it is not likely that the salty water over the rise from $1.2°C < \theta \leq 2.2°C$ moves south across the equator in a DWBC.

The CD 86–19 data show a maximum in northeastward velocity of order 10 cm s^{-1} offshore in the fresh bend at 3600 db with a ZVS near 4000 db ($\theta \approx 1.1°C$) between stations 95 and 100. This ZVS is the same as that indicated for the northeastward flow of Somali Basin bottom water in the equatorial section (Subsection 2.2.2). The maximum is similar in depth and magnitude to that described for the northern section on the same cruise (Subsection 2.3.3). However, a similar feature in the shear field is not seen in the CD 87–25 equatorial section.

2.3.3 The Northern Section

Saltiness above $\theta = 1.7°C$ near the coast in the northern sections indicates a southward flow here (Figure 2.11). The change in slope of the θ–S and θ–O_2 curves near $\theta = 1.7°C$ north of the equator together with the relative uniformity of the curves below this potential temperature indicate a fresh, oxygen-rich relatively uniform water-mass north of the equator. This feature suggests that water of $\theta \leq 1.7°C$ is relatively recently arrived from the south. The use of $\theta = 1.7°C$ as a ZVS sends the fresh oxygen-rich water below northward at the approximate depth of the Owen Fracture Zone and the salty water near the coast above southward. Assuming a ZVS at $\theta = 1.7°C$ (about 2800 db) here gives a northward velocity maximum of about 15 cm s^{-1} at 3600 db between stations 64 and 63 from CD 86–19 (Figures A.9 and A.12). In parallel with the temporal trend toward weaker flow at this depth in the equatorial section on CD 87–25, the signal is found spread out and offshore between stations 55 and 60 and reduced in amplitude to 5 cm s^{-1}
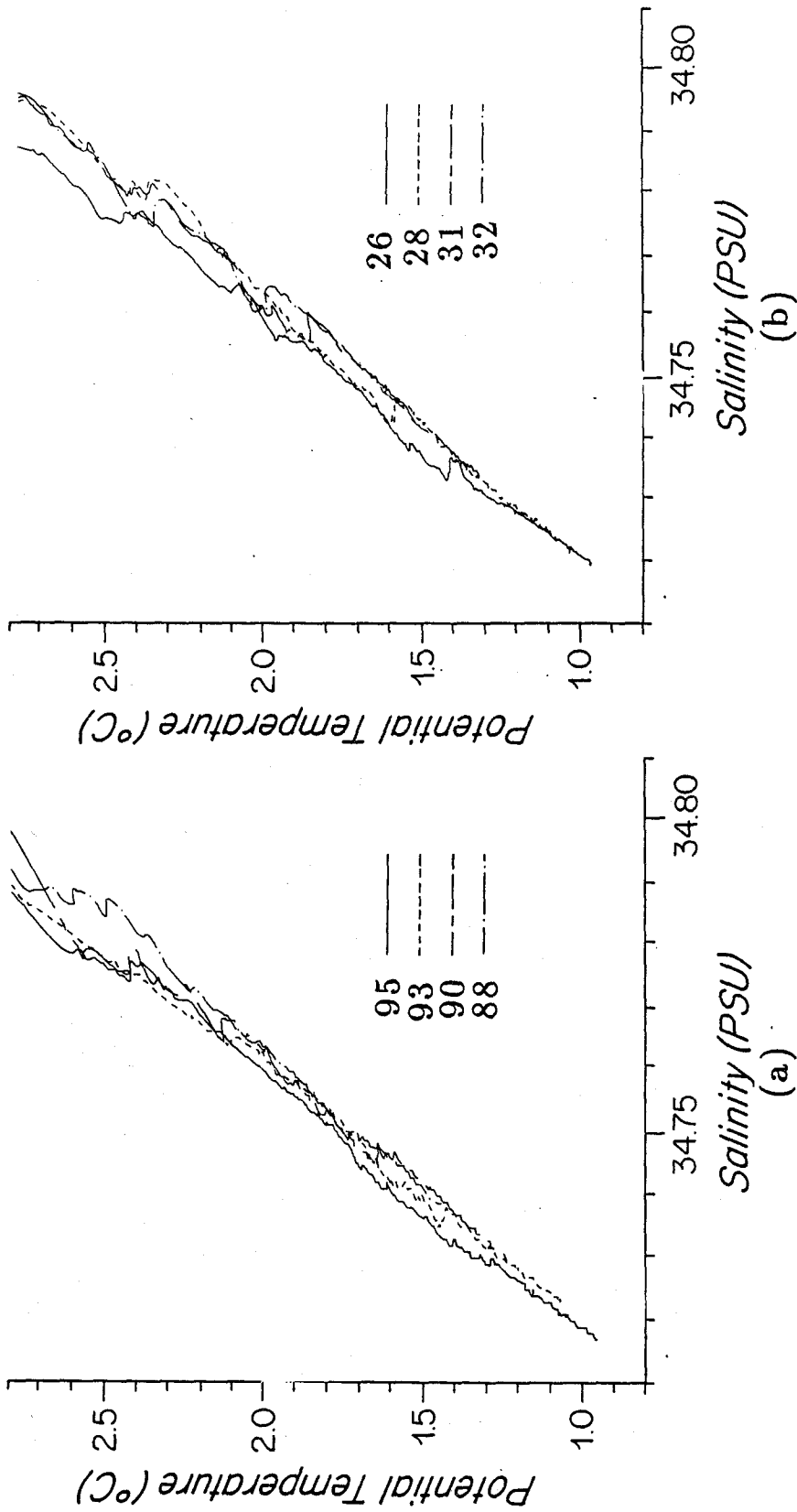
Figure 2.10: Deep θ–S curves for stations just north of the equator shows increasing salinity with increasing potential temperature toward the coast, stepping up from station to station. The pattern is similar with θ–O_2. See Figure 2.2 for station locations. (a) Stations 95 (solid), 93 (dashed), 90 (chain dashed) and 88 (chain dotted) from CD 86–10. (b) Stations 26 (solid), 28 (dashed), 31 (chain dashed) and 32 (chain dotted) from CD 87–25.

in the second survey (Figures A.25 and A.28). In both surveys the maximum in deep northward velocity in the northern section is associated with a maximum in buoyancy frequency near the coast at this depth as the isopycnals converge to form a cusp (Figures A.12 and A.28).

These maxima in northward velocity at 3600 db with currents falling off below 3800 db are near the estimated sill depth between the Somali and Arabian Basins of 3800 m (Wyrtki, 1971 p. 475), at the approximate potential temperature of the coldest water in the Arabian Basin. This northward velocity peaks at the correct depth and location to supply deep water to the Arabian Basin through the Owen Fracture Zone.

Net transports for these sections are not cited because of eddy noise and a weak geostrophic signal, but with a ZVS of $\theta = 1.7°C$, the northward transport for $1.2°C < \theta \le 1.7°C$ is 1.3×10^6 m^3 s^{-1} between stations 63 and 64 of CD 86–19 and 2.7×10^6 m^3 s^{-1} between stations 55 and 60 of CD 87–25.

2.3.4 The Carlsberg Ridge Section

The final section runs across the Carlsberg ridge into the Arabian Basin. The thermal wind in the northern and equatorial sections indicates that north of the equator the Somali Basin deep water flows northward, first offshore then along the western boundary toward the Owen Fracture Zone. For the circulation to be consistent with the Stommel-Arons framework when this water supplies the Arabian Basin bottom water, a southeastward flowing DWBC will exist on the northeastern flank of the Carlsberg Ridge. If the Arabian Basin bottom water were to enter from the gap in the Chagos-Laccadive Ridge near the southeastern part of the basin, the DWBC would flow northwestward (Subsection 4.1.2).

While the θ–S curves in the deep water are extremely uniform here, the θ–O_2 curves give a clue to the circulation in the area. Above $\theta = 1.7°C$ dissolved-oxygen concentration decreases to the northeast, whereas for $\theta \le 1.7°C$ the θ–O_2 curves are also quite uniform (Figure 2.12). This feature suggests that the bottom
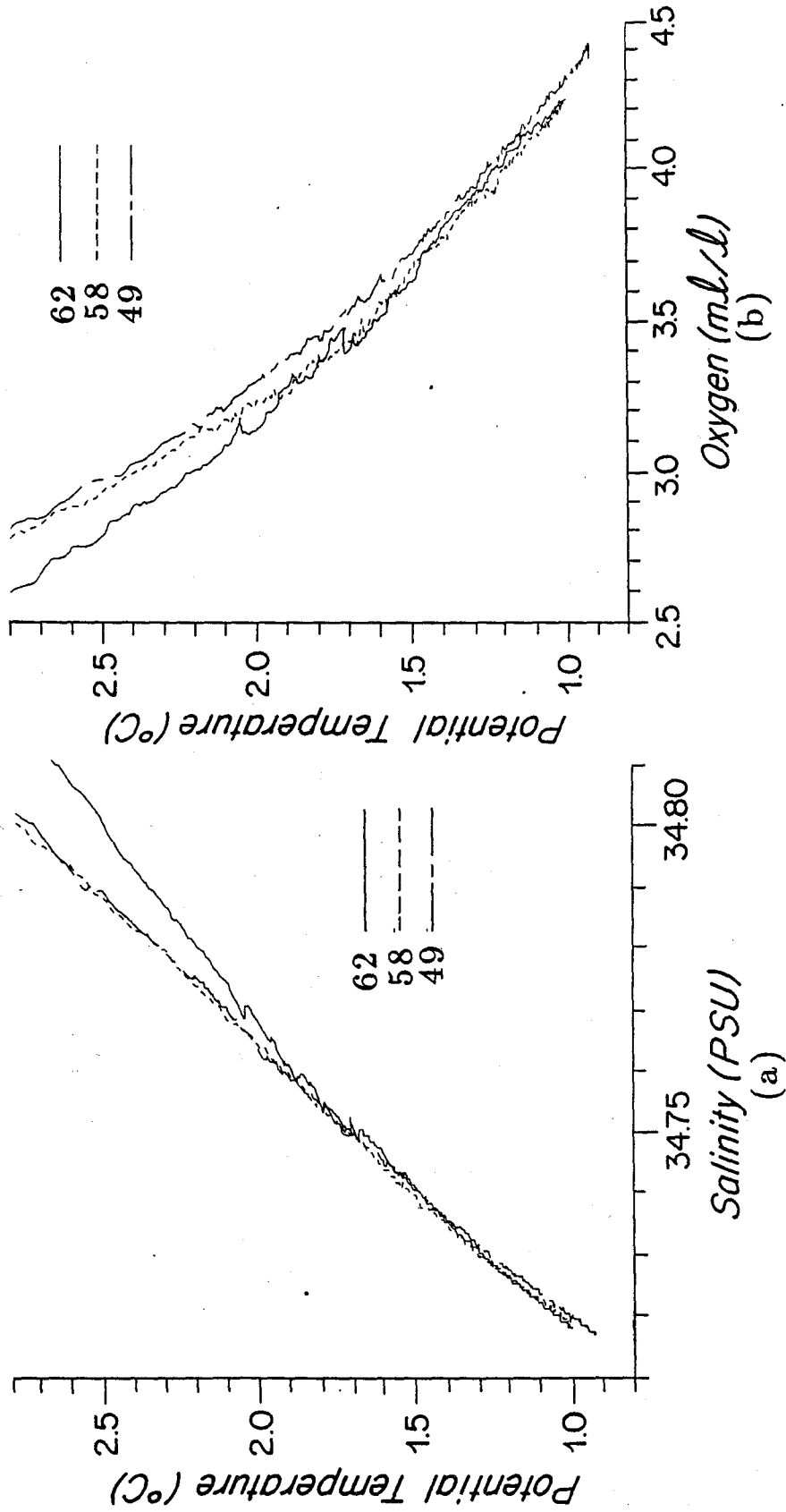
Figure 2.11: θ-property curves for the northern section. The curves change slope and become uniform below about $\theta = 1.7°C$, hinting at rapid renewal of deep water below and southward flow above. See Figure 2.2 for station locations (a) θ–S for stations 62 (solid), 58 (dashed) and 49 (chain dashed) from CD 86-19. (b) θ–O_2 for the same stations.

water for the basin is supplied for $\theta \leq 1.7°C$. Since most of the deep shear lies below this level as well (Figures A.16 and A.32), the $\theta = 1.7°C$ surface is used as a ZVS for estimating transports. Again consistent with the temporal trend in velocities upstream, the southeastward transport for the CD 86–19 section is 4.8×10^6 m^3 s^{-1}, with the transport estimate for the CD 87–25 section much weaker, about 0.5×10^6 m^3 s^{-1}, and to the northwest. However, if the ZVS for the CD 87–25 section were lowered with distance from the ridge crest, the isopycnals, which slope up toward the ridge, indicate that southeastward transport would result below.

2.3.5   Summary of Circulation For $1.2°C< \theta \leq 1.7°C$

The circulation for $1.2°C< \theta \leq 1.7°C$ is different from that for $\theta \leq 1.2°C$ (Figure 2.5). Some of the Somali Basin deep water is modified Somali Basin bottom water, all of which must upwell in the basin to exit after entering through the Amirante Passage. Some of the water south of the equator at this level originates from the DWBC on the Central Indian Ridge, which evidently has a branch which extends northwestward along the Mascarene Plateau and then westward into the interior of the Somali Basin. A trend toward saltiness and more oxygen-poor water north of the equator on the western boundary hints that this water does not flow northward along the boundary at the equator. However, there is evidence north of the equator for a northward flow along the western boundary toward the Owen Fracture Zone then southward in the Arabian Basin in a DWBC along the Carlsberg Ridge in the density field of CD 86–19. This signal is much reduced in the density field of CD 87–25. The change in the slope of the θ–S and θ–O_2 curves and their relative uniformity below $\theta = 1.7°C$ north of the equator and the divergence in the θ–O_2 curves above this potential temperature in the Arabian Basin comprise the main evidence in the water-mass properties which corroborate the signal of the current in the thermal wind north of the equator. The weaker and less consistent signal in CD 87–25 indicates that this circulation may be time-dependent.

Maps of water-mass properties on constant depth surfaces using historical data
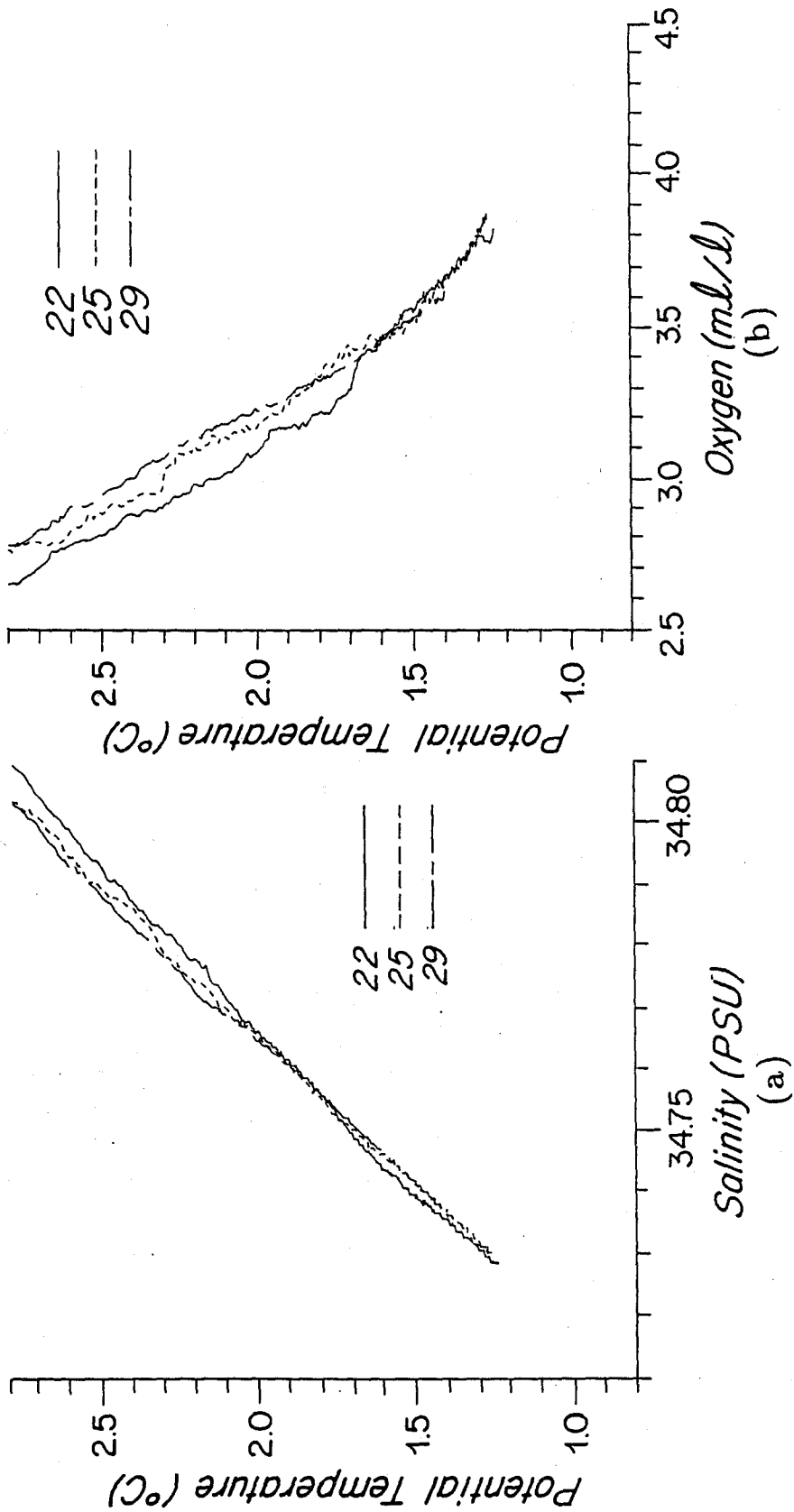
Figure 2.12: Deep θ-property curves for the Arabian Basin showing the uniform θ–O_2 curve for $\theta \leq 1.7°C$. Above this potential temperature dissolved-oxygen concentration decreases rapidly to the north. See Figure 2.2 for station locations. (a) θ–S for stations 22 (solid), 25 (dashed) and 29 (chain dashed) from CD 86–19 (b) θ–O_2 using the same stations.

in the region help to corroborate this description of the circulation. Dissolved-oxygen concentration at 3000 m depth is discussed above (Subsection 2.3.1). The western Indian Ocean section profiles of the GEOSECS expedition (Spencer et al., 1982 plates 3, 5, 11 and 13) are also of some use. The cold, fresh, oxygen-rich, silica-poor bottom water entering into the Arabian Basin extends below a depth of about 3000 m. As in the Pacific (Section 3.2), silica-rich deep water from the north is visible.

2.4 Historical Hydrographic Data

The R.V. *Atlantis II* cruise 8 hydrographic survey (AII 8) is the most useful unpublished historical data in the region. The salinities are not precise enough to allow for tracing deep water-mass properties or calculating deep geostrophic velocities. However, potential temperature profiles prove to be adequate to illuminate some features in the density field. The stations shown were taken after the southwest monsoon, from 21 September to 29 October 1963. (See Figure 2.1 for locations of stations reaching deeper than $\theta = 1.8°C$).

The section profile of potential temperature at 5°S from AII 8, the only other adequately sampled section in the southern Somali Basin aside from those of CD 86–19 and CD 87–25, once again shows the cold dense water of $\theta \leq 1.2°C$ riding up the continental rise of Africa (Figure 2.13). A transport estimate is not made because of the inaccurate salinity values and sparse station and bottle spacing, but there is no doubt the flow of bottom water is northward below a ZVS of $\theta = 1.2°C$.

The cross-equatorial section profile reveals a dome in the isotherms below $\theta = 1.1°C$, or about 4000 m (Figure 2.13). With a ZVS above the feature the flow would be to the northeast in the bottom water. This feature is reminiscent of the cross-equatorially symmetric shear seen in the bottom water in the most recent surveys.

The 5°N section profile departs somewhat from the northern section profiles of CD 86–19 and CD 87–25, in that a mid-depth ZVS of $\theta = 1.7°C$ plainly gives a
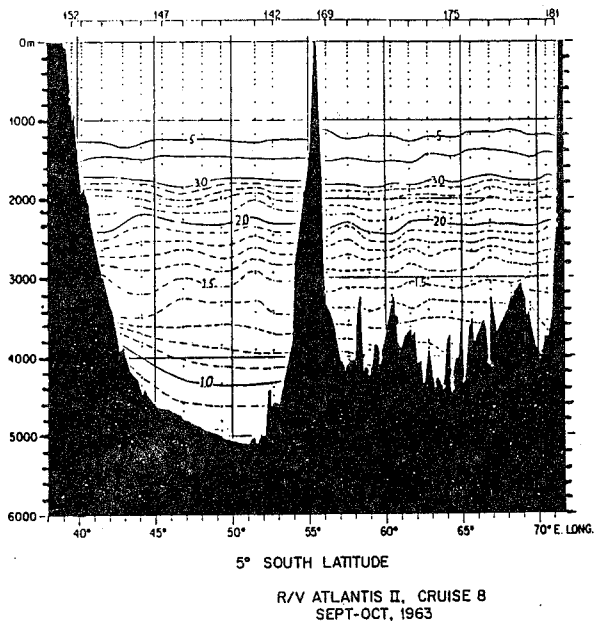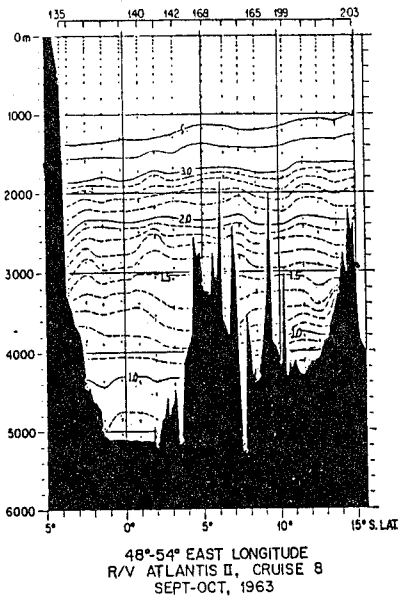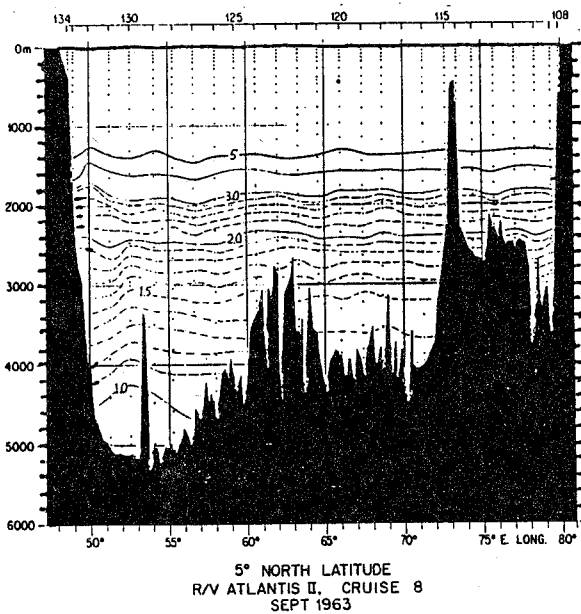
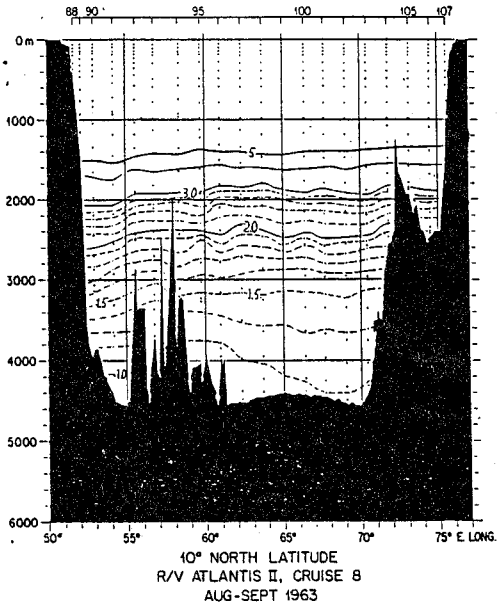Figure 2.13: Section profiles of potential temperature from the AII 8 survey in the Somali and Arabian Basins. See Figure 2.1 for station locations. (a) The 5°S section profile. (b) The cross-equatorial section profile. (c) The 5°N section profile. (d) The 10°N section profile.

northward bottom intensified flow at the coast, shown by the deep and bottom isotherms which slope down into the Somali Coast (Figure 2.13). With this choice of ZVS some of the water of $\theta \leq 1.7°C$ would be returned in a southward flow offshore. This fact can be seen in the downward slope to the east of isotherms below $\theta = 1.7°C$ offshore. This southward interior flow reduces the net northward flow of the bottom water into the northern Somali Basin.

The 10°N section profile is most notable for the indication of a southeastward flow of cold water pressed up against the flank of the Carlsberg Ridge in the Arabian Basin (Figure 2.13). With a ZVS of $\theta = 1.5°C$, slightly lower than that used above, the flow against the ridge would certainly be southward at the bottom. This DWBC is presumably supplied by flow of the deep water from the Somali Basin through the Owen Fracture Zone.

2.5   Conclusion

The two R.R.S. *Charles Darwin* cruises give a coherent picture of flow for $\theta \leq 1.2°$ in the Somali Basin (Figure 2.5). The deep cold water from the Mascarene Basin flows northward through the Amirante Passage below a ZVS of about $\theta = 1.2°C$ with an average transport of $4\text{x}10^6$ m^3 s^{-1}. This current reaches the latitude of 3.5°S with transport and ZVS unaltered, but near the equator it flows eastward. In the north, the presence of the bulk of the coldest densest water in the northern section profiles in the interior to the east of the Chain Ridge, and the most oxygen-poor bottom water in the basin near the continental rise off the Somali coast corroborate this supposition of eastward, not northward, flow near the equator. The transport estimates from the CD 87–25 data are slightly larger than those from the CD 86–19 data in this layer.

Some variability in the circulation for $1.2°C < \theta \leq 1.7°C$ in the Somali and Arabian Basins is seen (Figure 2.5). Of course, all the Somali Basin bottom water entering through the Amirante Passage must upwell in the basin and when modified must supply a good deal of the deep water. However, water-mass properties suggest

that some of the water in this potential temperature range south of the equator originates from the Central Indian Ridge to the east, not the Amirante Passage to the south. The water of southern origin does not appear to extend northward across the equator at the western boundary, but may do so offshore. Calculated northward velocity of deep water at 3600 db with a ZVS of $\theta = 1.7°C$ along the western boundary north of the equator is weaker during the southwest monsoon than during the northeast monsoon, although conclusions for the circulation from both cruises are tentative in this area. The southeastward flowing DWBC along the Carlsberg Ridge in the Arabian Basin appears to be fed by this northward flow through the Owen Fracture Zone and follows the same trend in the R.R.S. *Charles Darwin* data.

This trend is in direct opposition to the indications from historical data. While the AII 8 section profile of potential temperature south of the equator shows a similar structure to that observed in the CD 86–19 and CD 87–25 surveys, indicating a steady DWBC south of the equator, a current meter record at 3000 m on the equator indicates a seasonal reversal in the deep flow positively correlated with the surface current (Schott et al., 1989). The two previous comprehensive hydrographic surveys, separated by 21 years and a monsoon season, indicated the same (Warren et al., 1966 and Fieux et al., 1986). If the DWBC north of the equator reverses directions with the monsoon, it is possible that the weak southeast monsoon of 1987 was not strong enough to drive the DWBC northward across the equator that season. However, in all sections south of the equator the DWBC does appear to be moving north.

Chapter 3

Pacific Ocean Observations

Circulation of the Lower Circumpolar Water (LCPW) and the North Pacific Deep Water (NPDW) is described at 10°N in the Pacific using a recent transpacific CTD section. Salinity, S, dissolved-oxygen concentration, O_2, and dissolved-silica concentration, H_4SiO_4, are water-mass properties which are used to fix a boundary in potential temperature between the LCPW and the NPDW. Transports of LCPW and NPDW are estimated in each of the three central basins at this latitude using zero-velocity surfaces (ZVS's) which result in water with southern water-mass properties moving north and water with northern water-mass properties moving south. Deep Western Boundary Currents (DWBC's) of LCPW are found in the East Mariana and the Central Pacific Basins contributing to net northward transports of 5.0–14.8 and 8.1×10^6 m^3 s^{-1} respectively in these basins. In the Northeast Pacific Basin a southward interior flow of 4.7×10^6 m^3 s^{-1} of LCPW is observed. The net flow of salty oxygen-rich silica-poor LCPW for $\theta \leq 1.2°C$ at this latitude is $8.4–18.2 \times 10^6$ m^3 s^{-1} northward. A net southward flow of 2.7×10^6 m^3 s^{-1} of fresher, oxygen-poor, and silica-rich NPDW for $1.2°C < \theta \leq 2.0°C$ is estimated across the three basins, with almost all of the southward flow in the NPDW occurring the Northeast Pacific Basin, on the western flank of the East Pacific Rise.

3.1 The Data Set

A transpacific hydrographic cruise from the Philippines to Costa Rica was made on the R.V. *Moana Wave* from January to May 1989 at a nominal latitude of 10°N

(cruise MW 89–3). Vertical profiles from the surface to the bottom of conductivity, temperature, pressure and dissolved-oxygen concentration were taken using a suite of Neil-Brown MkIII CTD's fitted with Beckman polarographic oxygen sensors. Station spacing was at intervals of no more than 50 nautical miles, reduced to 10–30 nautical miles over rapidly changing topography. The bottom was approached within about 100 m on stations taken during the first leg, and within about 10 m on most stations thereafter (when a transducer was jury-rigged to replace the ship's failed hull mounted transducer). A total of 221 stations were taken, with repeat casts at several locations to aid in data calibration. The calibrated deep temperature, salinity and dissolved-oxygen concentration profiles are thought to be accurate to $\pm 0.002°C$, ± 0.0017 psu and ± 0.03 ml l^{-1} or better respectively.

Water samples were taken with a General Oceanics rosette sampler fitted with 24 10–l Niskin bottles. Water sample salinities were analyzed on a Guildline Autosal salinometer, and dissolved-oxygen concentrations measured with a modified Winkler titration method (Knapp and Stalcup, 1987). Analyses of concentrations of dissolved silica, phosphate and nitrate were carried out on a Technicon Auto-Analyzer II. Chlorofluorocarbon and tritium-helium measurements were taken on selected casts and bottles. Bottle oxygen measurements are accurate to ± 0.025 ml l^{-1} or better. Nutrients are accurate to $\pm 1\%$. The bottle salinities are accurate to ± 0.001 psu.

In the East Mariana basin the data are supplemented by six sections extending from 5°S to 10°N along 165°E collected by the U.S.-P.R.C. TOGA program during cruises 1 through 6. The data were collected using a Neil-Brown MkIII CTD fitted with a Beckman polarographic oxygen sensor during February 1986, December 1986, October 1987, May 1988, November 1988 and May 1989. The stations used are spaced at even 1° latitude intervals from 5°S to 10°N and more closely at 0.5° latitude intervals between 3°S to 3°N.

The MW 89–3 CTD section cuts through five basins in the Pacific. (See Figures 3.1 and 3.2). The outermost Philippine and Guatemala basins are isolated from the LCPW in the Central Pacific south of 10°N and stations taken in those basins

are not discussed at length here. From the equator to 10°N the Caroline Islands and Solomon Rise make up the deep western boundary for the East Mariana Basin. The Marshall and Gilbert Islands form the deep western boundary for the Central Pacific Basin, separating it from the East Mariana Basin. The Line Islands form a third barrier to zonal deep flow and separate the Northeast Pacific Basin from the Central Pacific Basin. The Northeast Pacific Basin, unlike those to the west, is not likely to be directly supplied with deep water from the south because it lies to the east of the Samoan Passage, where the LCPW is observed to flow northward south of the equator (Subsection 1.2.3).

To the north the Hawaiian Ridge presents a barrier to northward flow from the Central Pacific Basin, and the LCPW must exit through the Northwest Passage to the west and the Clarion Fracture Zone to the east. In the Northeast Pacific Basin the bathymetry shallows equatorward and eastward from near 5500 m in the Clarion Fracture Zone to 4300 m at the Equator and about 3000 m at the crest of the East Pacific Rise. A passage with a sill depth between 4700 and 4800 m at 0°N 155°W exists between the Line Islands and the ridge at the equator.

3.2   Water-Mass Properties

The subset of stations (40–190) from the cruise which fall in the East Mariana Basin, the Central Pacific Basin and the Northeast Pacific Basin are used in this study. Here deep salinity, dissolved-oxygen concentration and dissolved-silica concentration all form tight curves against potential temperature. Chlorofluorocarbons are not observed in the deep North Pacific, and the tritium-helium data are not yet available, so these water-mass properties will not be discussed here. Dissolved-phosphate and nitrate concentrations are not discussed either, because they are so well correlated with dissolved-oxygen concentration in the deep water that they provide no additional information as water-mass properties. Relations between the deep water-mass properties and the geostrophic shear field are discussed for each basin below.
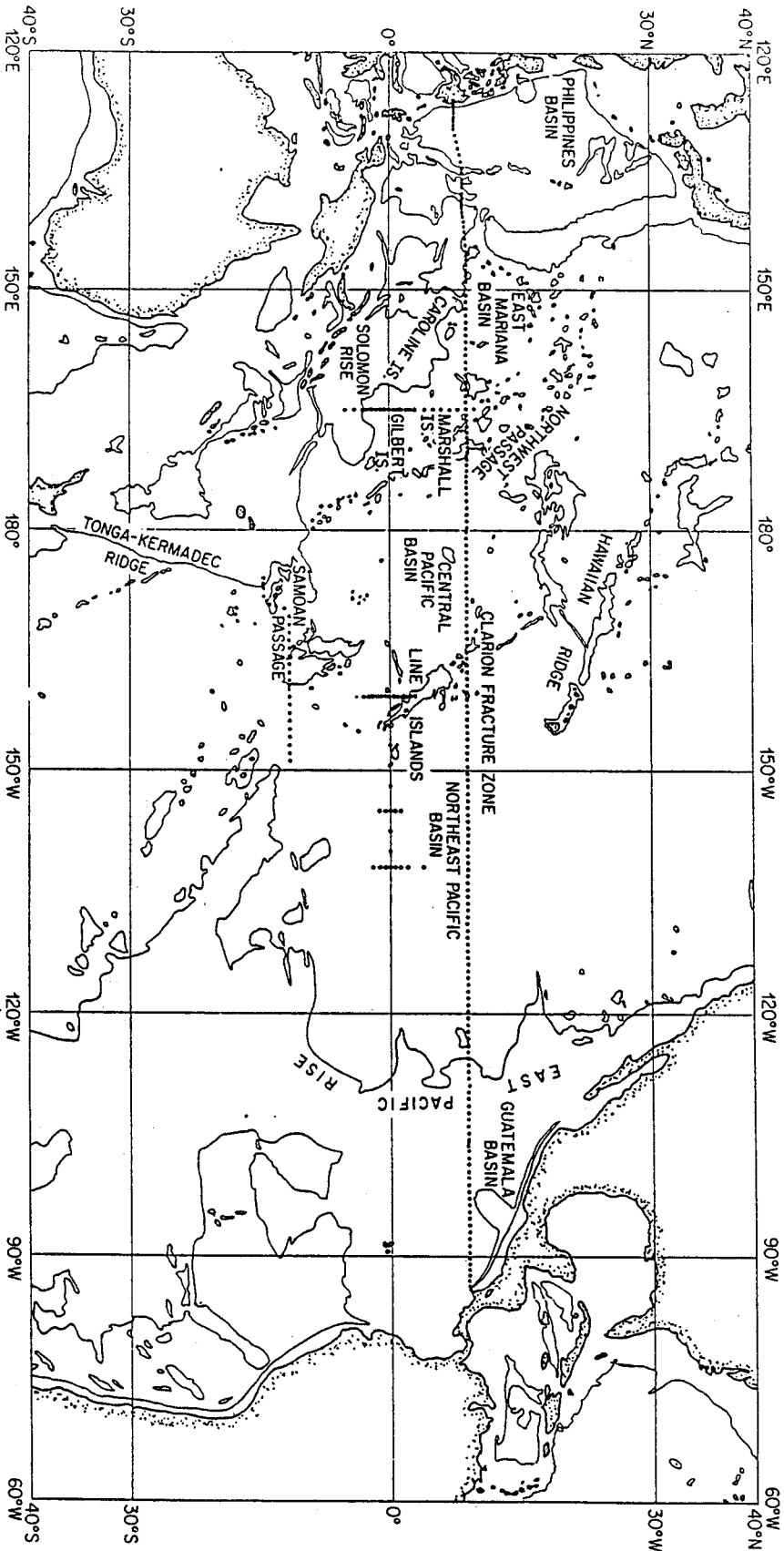
Figure 3.1: Station locations for MW 89-3 transpacific cruise at 10°N. Also included are the locations of stations from 5°S to 10°N at 165°E from the U.S.-P.R.C. TOGA cruises, locations of direct velocity measurements near the equator at 159°W (Firing, 1989) and 138°W to 153°W (Ponte and Luyten, 1989) and station locations near 12°S and the Samoan Passage (Taft et al., 1990). The 4000 m isobath is adapted from GEBCO (1984).

Figure 3.2: Section profile of potential temperature, θ, in $^\delta$C at 10°N in the Pacific, MW 89–3 (top). Section profile of dissolved-silica concentration, H_4SiO_4, in $\mu mol\ l^{-1}$ (bottom). Vertical exaggeration is 500:1. See Figure 3.1 for section location.

There are three water masses of interest in the analysis of deep and bottom circulation in the North Pacific. The bottom water is composed primarily of salty oxygen-rich waters of southern origin, which will be called LCPW here for c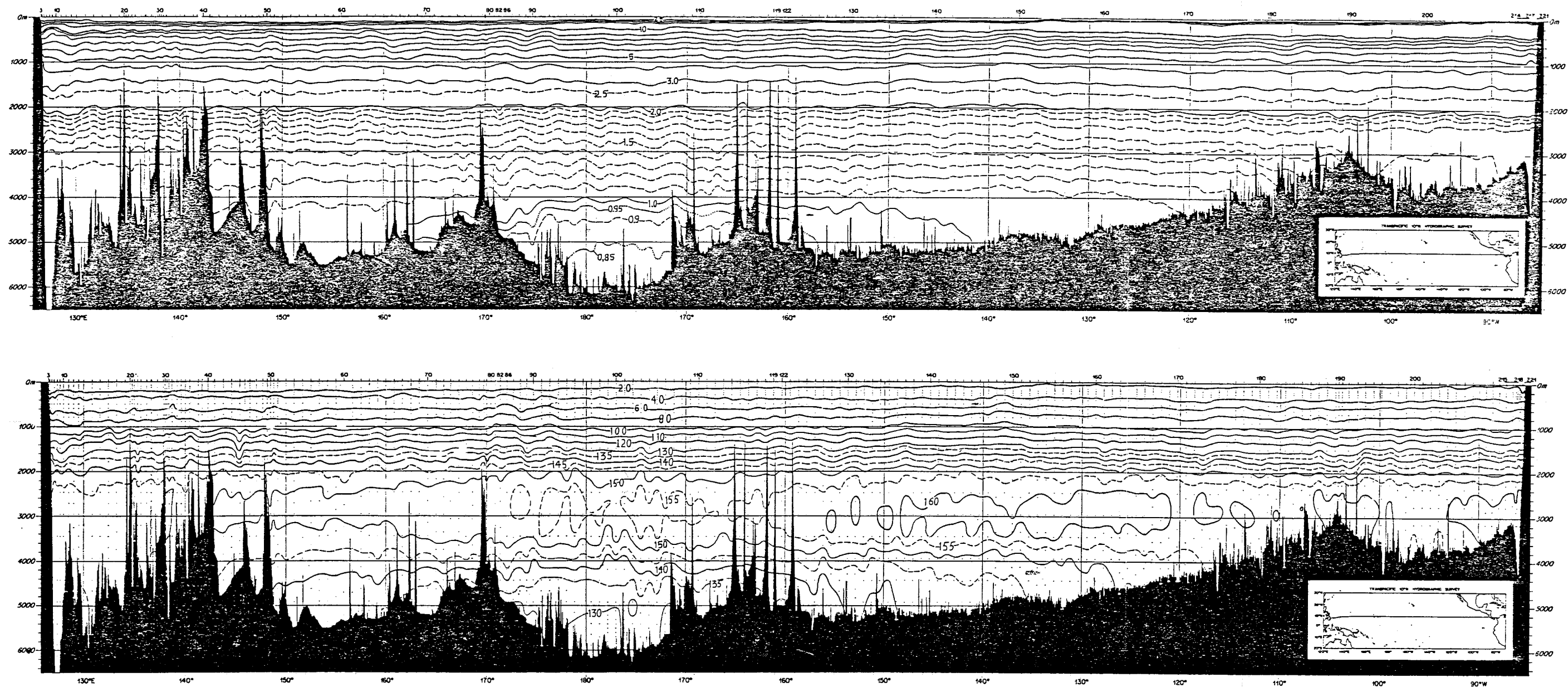onvenience. The deep water lies between the LCPW below and the Intermediate Water (IW) above, and is marked by a maximum in dissolved-silica concentration gained in the Northeast Pacific. This water mass will be called the NPDW. The IW lies above the NPDW and is marked by a salinity minimum.

The LCPW is actually a mixture of North Atlantic Deep Water (NADW), LCPW and IW (Mantyla and Reid, 1983). This LCPW is cold, with a minimum potential temperature below 0.85°C (Figure 3.2), salty, with a maximum salinity near 34.707 psu (Figure 3.3), oxygen-rich, with dissolved-oxygen concentration reaching 4.5 $ml\ l^{-1}$ (Figure 3.4) and relatively silica-poor, with a dissolved-silica concentration miminimum at the bottom below 130 $\mu mol\ l^{-1}$ (Figures 3.1 and 3.5).

Below 800 m, the θ–S and θ–O_2 curves run relatively smoothly from salty and oxygen-rich at the cold end in the LCPW below to fresh and oxygen-poor in the IW above (Figures 3.3 and 3.4). The salinity and dissolved oxygen minimums that mark the IW are not shown in these figures, but they occur at $\theta \approx$ 6°C (700–800 m) and $\theta \approx$ 8°C (400–500 m) respectively. The minimum salinity values range from 34.52 to 34.56 psu from west to east and the minimum dissolved-oxygen values from 1.5 to 0.05 $ml\ l^{-1}$ also from west to east. Salinity in the IW increases to the east and dissolved-oxygen concentration decreases to the east, and this trend continues down even to the deep temperature range illustrated (Figures 3.3 and 3.4).

While the θ–S and θ–O_2 curves run from the LCPW up to the IW minimums, over a range of almost 5000 m in places, another water mass is defined between by the deep silica maximum which occurs at $\theta \approx$ 1.5°C (2800 m) at 10°N (Figures 3.5 and 3.2). The dissolved-silica concentration maximum reaches values of 150 and 160 $\mu mol\ l^{-1}$ in the west and east respectively. This maximum marks the NPDW, which gains its dissolved silica from high latitudes (Sverdrup et al., 1942; Edmond et al., 1979).

In order to quantify transports of the LCPW and NPDW across the central
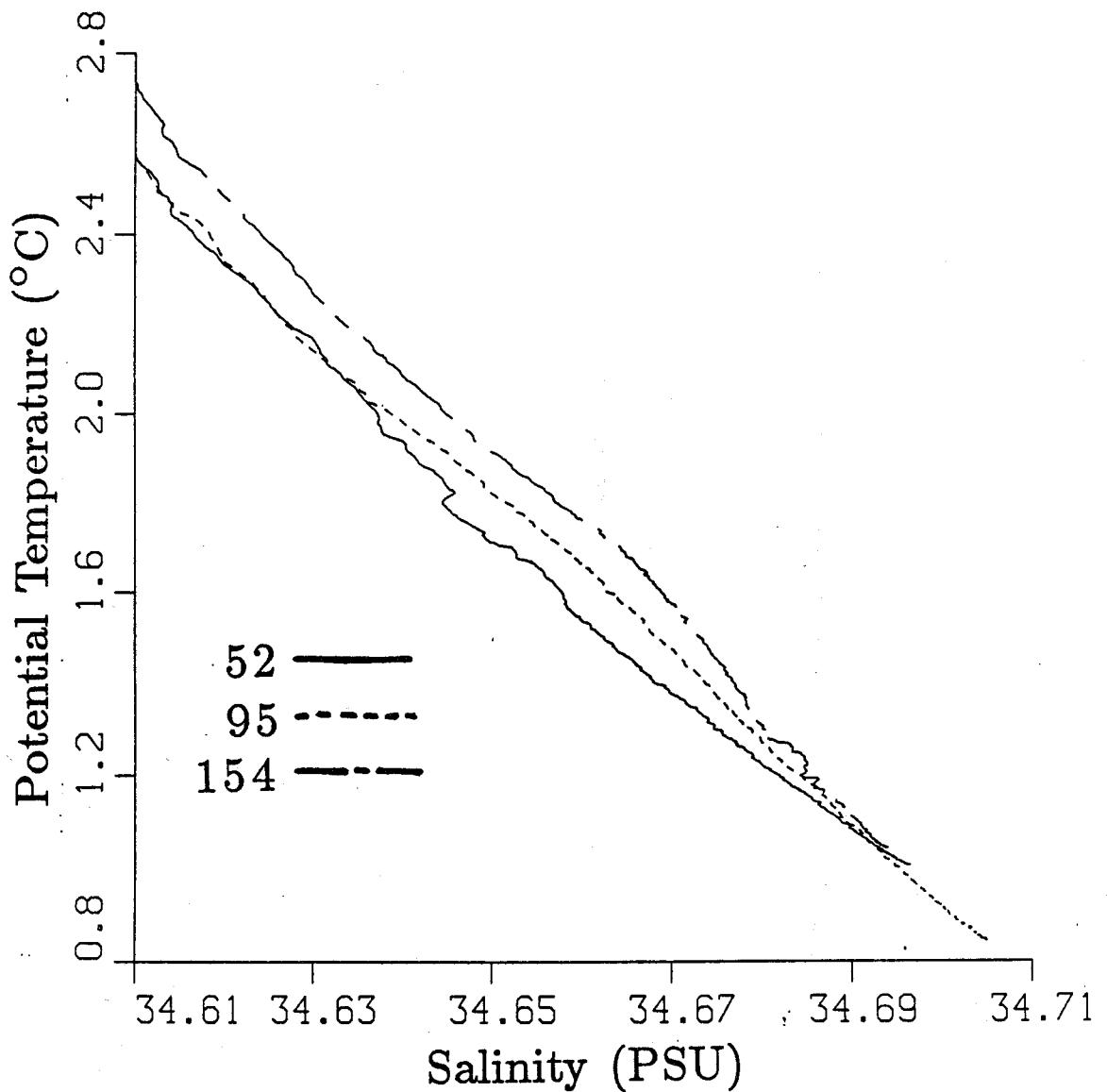
Figure 3.3: Deep θ–S curves for station 52 from the East Mariana Basin (solid), station 95 from the Central Pacific Basin (dashed) and station 154 from the Northeast Pacific Basin (chain dashed). Curves run from the salty LCPW below to the fresh IW above. The East Mariana Basin station is saltier than the other two in the LCPW, and the Northeast Pacific Basin station curves to join that of the Central Pacific Basin in the LCPW. See Figure 3.2 for station locations.
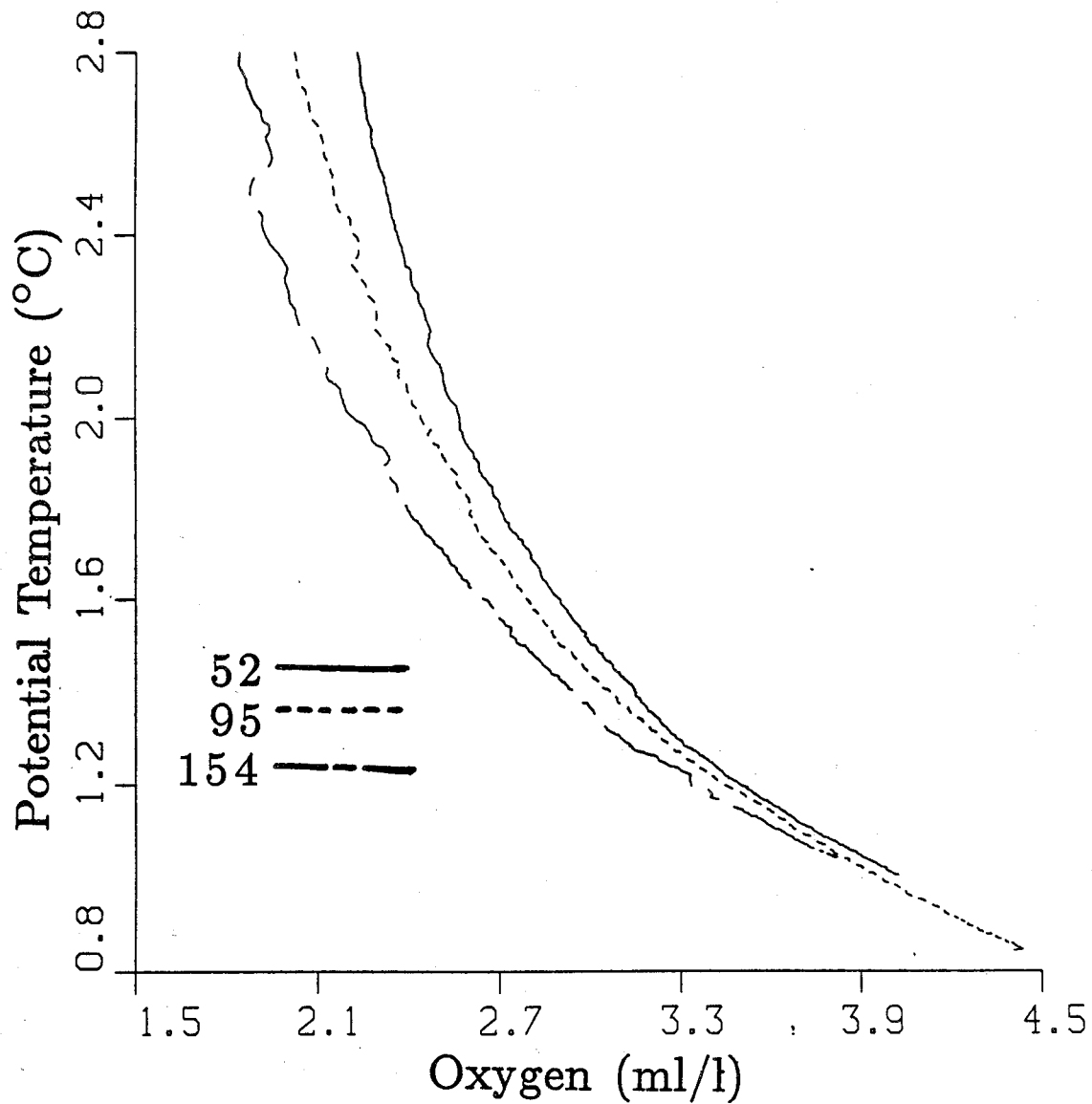
Figure 3.4: Deep θ–O$_2$ curves for same stations as Figure 3.3. The increase in slope below $\theta \approx 1.2°$C indicates that the LCPW is renewed more rapidly from the south than that above. The decreasing concentration for $\theta > 1.2°$C to the east is indicative of the increasing age of the water. See Figure 3.2 for station locations.
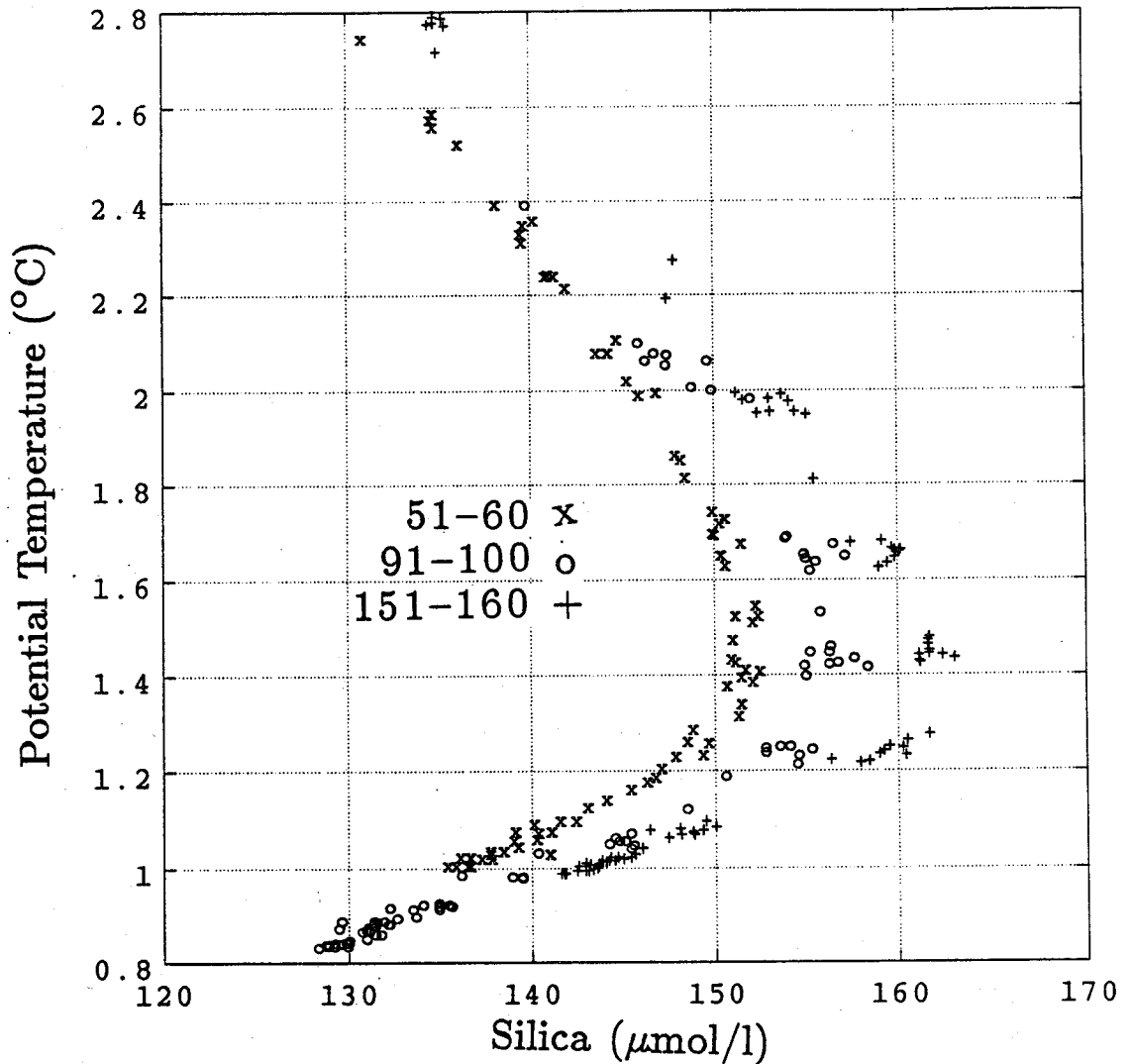
Figure 3.5: Deep θ-H_4SiO_4 values for stations 51–60 in the East Mariana Basin (x's) 91–100 in the Central Pacific Basin (o's) and 151–160 in the Northeast Pacific Basin (+'s). The low values for the East Mariana Basin for $\theta \leq 1.2°C$ indicate LCPW of most recent southern origin. The similarity for $\theta \leq 1.2°C$ in the Central Pacific and Northeast Pacific Basins shows the connection between the water of the two basins. Increasing values to the east for $1.2°C < \theta \leq 2.0°C$ show NPDW with more northern water-mass properties to the east. See Figure 3.2 for station locations.

Pacific basins at 10°N a boundary is defined between the LCPW and the NPDW and another between the NPDW and the IW. Potential temperature surfaces are chosen for these boundaries because they are roughly conservative and used in the θ–property plots to define the water masses themselves. These boundaries are determined in part by the geostrophic shear field, and in part by a closer analysis of the water-mass properties.

The boundary between the LCPW and the NPDW must be below the maximum in dissolved silica at $\theta \approx 1.5°C$. At $\theta \approx 1.2°C$ the θ–S and θ–O_2 curves in each of the three basins begin to join (Figures 3.3 and 3.4), and in addition below this potential isotherm the dissolved-oxygen concentration increases more rapidly with decreasing potential temperature. Finally, most of the deep geostrophic signal of the DWBC's of the East Mariana and Central Pacific Basins is found below $\theta \approx 1.2°C$ (where the isotherms fall into the western boundary, Figure 3.2). Thus the boundary between the LCPW and the NPDW is set at $\theta = 1.2°C$, only slightly colder than that used near the Samoan Passage at 12°S (Taft et al., 1990). Interestingly, this is the same potential temperature used to define the top of the bottom water in the Somali Basin (Section 2.2), near the equator in the other ocean with only a southern source of bottom water, the Indian Ocean.

The boundary between the NPDW and the IW must lie above the maximum in dissolved silica. This boundary is picked somewhat arbitrarily at $\theta = 2.0°C$ (near 2000 m) such that the values of silica concentration at the top boundary of the NPDW are close to those at its bottom boundary, nicely bracketing the silica-rich waters in the vertical (Figure 3.5). This choice also brackets some features in the geostrophic shear field, which were also used in picking the boundary.

The LCPW is defined as water of $\theta \leq 1.2°C$ and the NPDW as water of $1.2°C < \theta \leq 2.0°C$. In a broad sense the LCPW thus defined gains its water-mass properties from the south and the NPDW its water-mass properties from the north, so the LCPW on the whole should move northward away from its source and the NPDW southward away from its source. It is important to note that there are variations in the water-mass properties in the horizontal at 10°N within these temperature

classes which suggest that, while this assumption is on the whole correct, there is some water in the LCPW temperature class that may be moving south and some water in the NPDW temperature class that may be moving north. These exceptions, supported by the geostrophic estimates of transport, are detailed below.

Within the potential isotherms bounding the NPDW salinity increases to the east, dissolved-oxygen concentration decreases to the east, and dissolved-silica concentration increases to the east (Figures 3.3, 3.4 and 3.5). The most silica-rich oxygen-poor deep water is found to the northeast. This water is some of the oldest water in the World Ocean. Thus the water in the Northeast Pacific Basin, over the western flank of the East Pacific Rise, has the most northern water-mass properties and should be moving south, away from its source waters. In contrast, the relatively silica-poor and oxygen-rich water in the East Mariana Basin has the most southern water-mass properties of the NPDW and should be moving north if any of the NPDW is moving north.

The fact that the salinity increases to the east is interesting for another reason. There is a salty knee in the θ–S curve at $\theta \approx 1.6°C$ in the Northeast Pacific Basin (Figure 3.3). It is unlikely that this knee is produced by simple vertical mixing between the LCPW and the IW. Upon closer inspection this knee strengthens to the east within the basin and is joined by the cold end-member of the θ–S curve for the Guatemala basin to the east (Figure 3.6). This pattern suggests that the knee originates from the relatively salty bottom water in the Guatemala Basin flowing westward over the crest of the East Pacific Rise. A core of δHe^3 observed at 2600 m ($\theta \approx 1.6°C$) at 10°N in the HELIOS section at 135°E (Craig, 1990) indicates that this salty knee has been made by heating from hydrothermal vents. Cold salty water entering the Guatemala Basin could be warmed by the vents and become anomalously saline for its now warmer potential temperature. Upon spilling over the crest of the East Pacific Rise it would produce a feature like the knee in the θ-S curve, strongest at the crest of the rise, that is observed in the Northeast Pacific Basin

In the potential temperature range of the LCPW, the water is oxygen-rich and

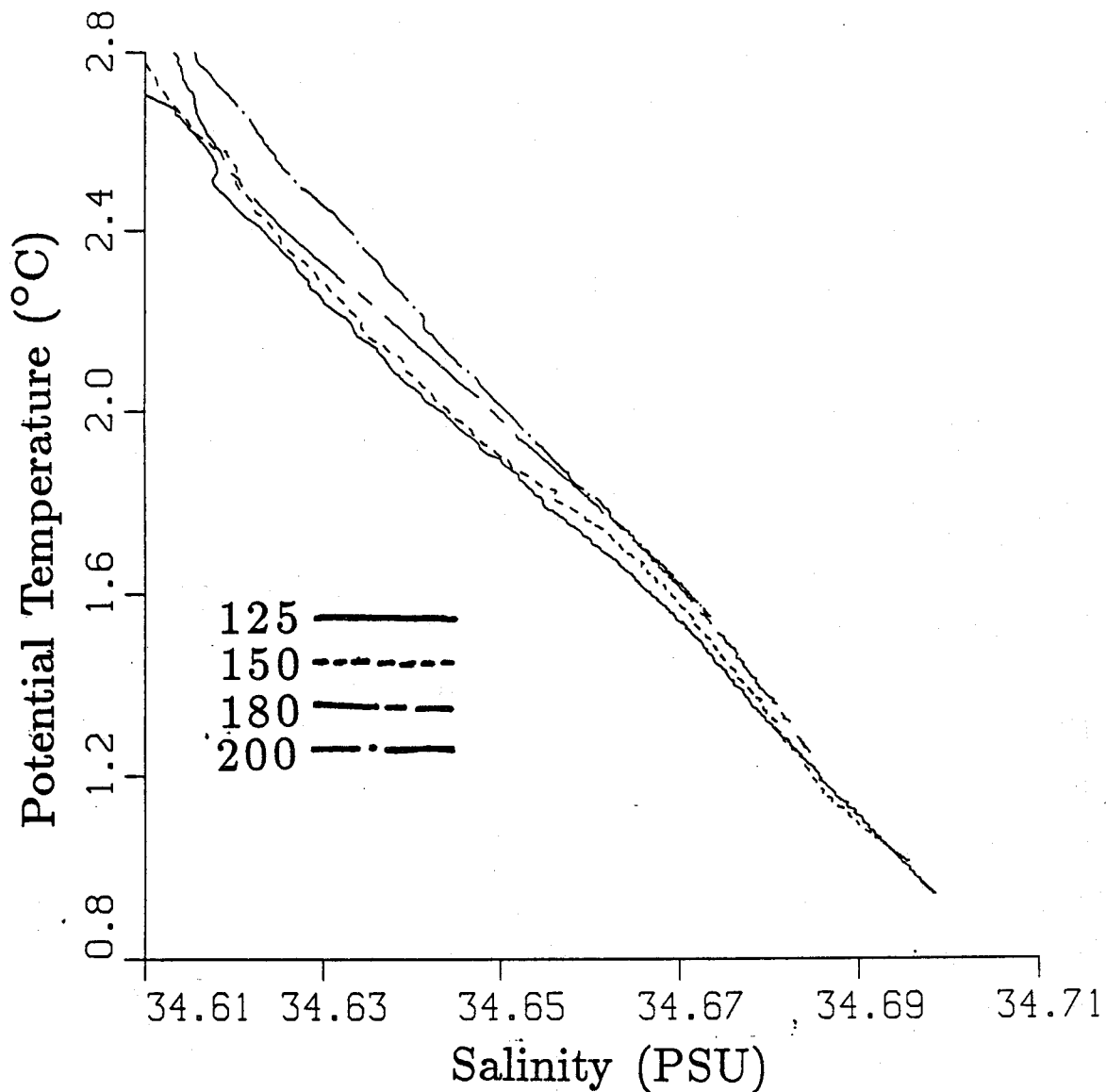Figure 3.6: Deep θ–S curves for stations 125 (solid), 150 (dashed), and 180 (chain dashed) from the Northeast Pacific Basin and 200 (chain dotted) from the Guatemala Basin. The salty knee in the curves found $\theta \approx 1.6°C$ is the result of geothermal heating. The knee gets stronger to the east and is joined by the cold end-member of the curve from the Guatemala Basin. See Figure 3.2 for station locations.

silica-poor in the East Mariana Basin (Figures 3.4 and 3.5). The LCPW in this basin is slightly saltier than those of the two basins to the east at its coldest potential temperatures (Figure 3.3). These features suggest that LCPW of the East Mariana Basin is the most recently arrived to the North Pacific at this latitude. The water is coldest in the Central Pacific Basin (Figure 3.2) and slightly more silica-poor and oxygen-rich than that in the Northeast Pacific Basin. This water too should be moving north, since it is the coldest. In the Northeast Pacific Basin the water is slightly more silica-rich and oxygen-poor than that to the west, although the contrast of the western basin with the central basin is greater than that of the central basin to the eastern basin. In fact, the water-mass properties in the LCPW of the two eastern basins are close enough to suggest that the circulation of the two are somehow linked. The manner of this link is explained below. While the LCPW in the East Mariana Basin and the Central Pacific Basin should both be moving north, the water of the Northeast Pacific Basin could be moving south, being the least southern in water-mass properties in this potential temperature range.

3.3 Transport Estimates

The geostrophic shear field in each basin is used in conjunction with the water-mass properties as discussed above to determine a ZVS for each basin. In the East Mariana Basin $\theta = 1.3°C$ ($\approx$ 3400 db) gives a large northward transport in the LCPW and a small northward transport in the NPDW above. In the Central Pacific Basin the surface $\theta = 1.4°C$ ($\approx$ 3000 db) yields a large northward transport of LCPW and a negligible southward transport of NPDW. However, in the Northeast Pacific Basin there is no mid-depth ZVS that will yield a northward flow of LCPW. Here the shear is reversed, and a ZVS of $\theta = 1.65°C$ ($\approx$ 2500 db) gives a net southward transport in the LCPW, and in the NPDW above. A dynamical explanation of this southward flow of LCPW is advanced below (Section 4.3).

Using the values of potential temperature above for the ZVS's, transports of LCPW ($\theta \leq 1.2°C$) and NPDW ($1.2°C < \theta \leq 2.0°C$) are estimated in each basin.

Geostrophic transport estimates are referenced to the ZVS or the deepest common level (DCL) if it is shallower. The velocity at the DCL is applied to the triangle made up by the distance between stations and the difference in pressure between the pressure at the DCL and the deepest pressure of the two stations (i.e. the velocity at the DCL is applied to the bottom triangle). The transport estimates explained below are combined with analysis and results from previously published data to obtain a circulation pattern for the LCPW in the region (Section 3.4). The schematic of this circulation (Figure 3.7) may be helpful in following the discussion that follows.

In the East Mariana Basin (Stations 40–78) 5.0×10^6 m^3 s^{-1} of LCPW moves north using a ZVS of $\theta = 1.3°$C and 1.1×10^6 m^3 s^{-1} of NPDW moves northward. In the Central Pacific Basin (Stations 78-114) the ZVS used is $\theta = 1.4°$C resulting in a net northward flow of LCPW of 8.1×10^6 m^3 s^{-1} and a small southward flow of NPDW of 0.2×10^6 m^3 s^{-1}. In the Northeast Pacific Basin (Stations 114-190) an estimated 4.7×10^6 m^3 s^{-1} of LCPW moves southward using a ZVS of $\theta = 1.65°$C with a southward transport of NPDW of 3.6×10^6 m^3 s^{-1}. The net transport of LCPW for the three basins (Stations 40–190) is 8.4×10^6 m^3 s^{-1} northward, and the net transport of NPDW is 2.7×10^6 m^3 s^{-1} southward.

The bulk of the northward flow of LCPW in the East Mariana Basin occurs between stations 51 and 52 in a DWBC just off the Caroline Islands. The dynamic signature is associated with silica-poor water and hence water of recent southern origin (Figure 3.2). However, the lack of resolution in the DWBC makes the estimate of transport worrisome. Thus six U.S.-P.R.C. TOGA sections at 165°E extending from 5°S to 10°N are combined to estimate an average transport of LCPW and NPDW through the region.

This transport estimate at 165°E was arrived at using a somewhat more sophisticated approach than the other estimates, which are simple geostrophic calculations using quasi-synoptic sections. The station locations don't vary from survey to survey, but the bottom pressures of the stations do. As expected in an equatorial region transport estimates for the LCPW and NPDW varied significantly from survey to
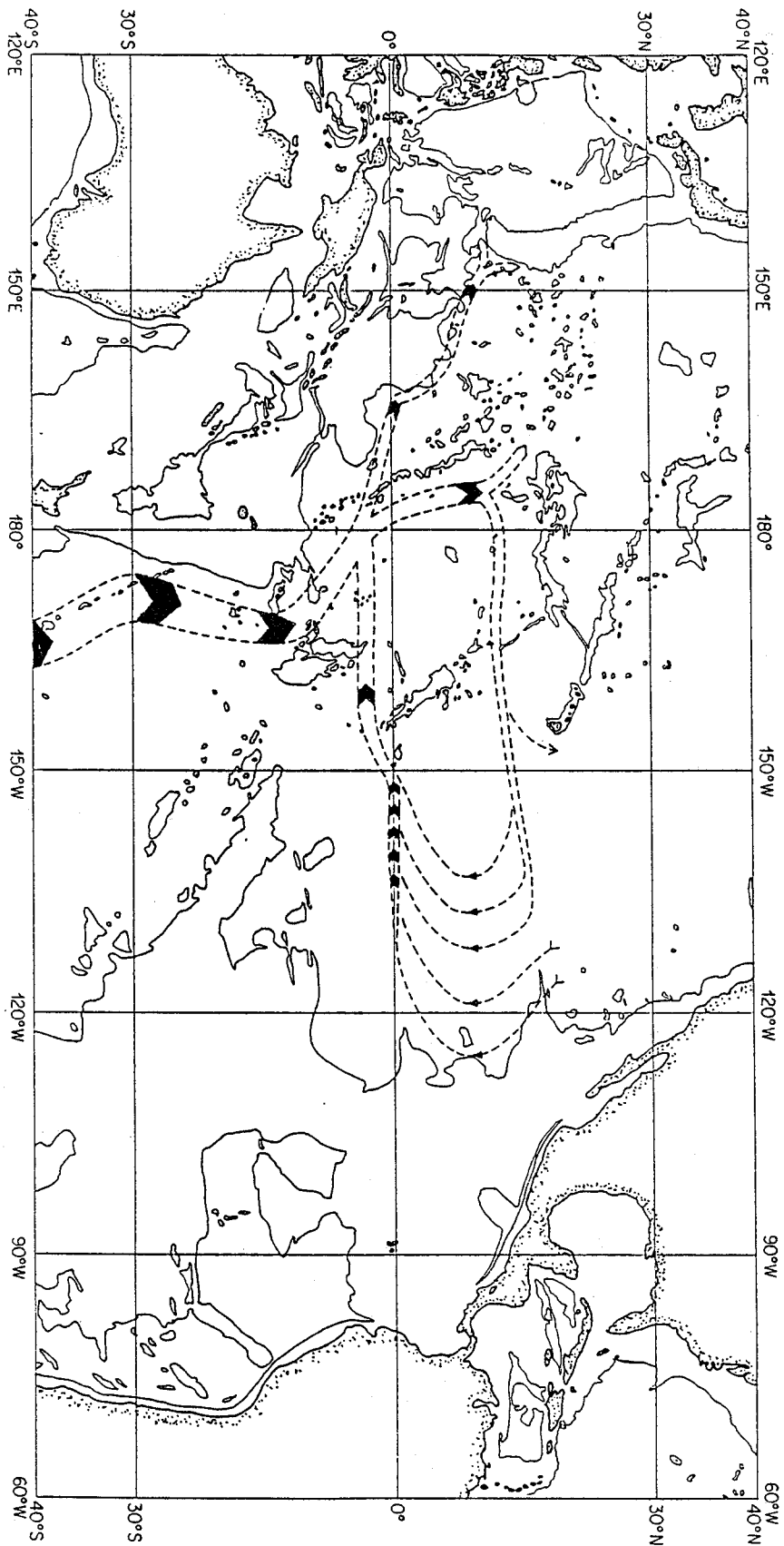
71

Figure 3.7: Schematic of the circulation of LCPW in the near-equatorial Pacific with the 4000 m isobath adapted from GEBCO (1984). Arrows show direction and approximate locations of flow. Arrow thickness is proportional to transport with the two southern arrows representing transports of 20x10⁶ m³ s⁻¹ each. Locations of observations used to construct the schematic are shown in Figure 3.1.

survey so an average of all the surveys was constructed. To use all the information from the six surveys temperature, salinity, and dissolved-oxygen concentration were averaged on pressure surfaces into a composite station at each location. At the highest pressures only the deepest station contributes to this composite station, but further up in the water column more and more of the stations contribute to the average. Between 3°S and 10°N from 1 to 6 stations reached below 4000 db at each location, with an average of 3.5 station reaching this pressure at each location. In the equatorial band between 2°S and 2°N from 2 to 5 stations reached this pressure at each location, with an average of 3.2 reaching this location. Dynamic heights for geostrophic calculations were computed using these composite stations.

A conventional mid-latitude geostrophic calculation produced unreasonably large velocities with a degree of the equator. To estimate the zonal velocity at the equator the thermal wind relation is often differentiated to yield

$$\beta y u_{zy} + \beta u_z = -\frac{g}{\rho}\rho_{yy}.$$

At the equator $y = 0$ and the first term of the LHS can be neglected, so the zonal velocity is related to the curvature of the density field (Lukas and Firing, 1984). A profile of potential temperature for the composite section shows a bowl in the deep potential isotherms at the equator which indicates increasing westward velocity toward the bottom below a ZVS of $\theta = 1.3°C$ ($\approx$ 3400 db), the same ZVS used at 10°N in the East Mariana Basin (Figure 3.8). To find this curvature a second order polynomial was fit to dynamic height on constant pressure surfaces for the composite stations about the equator using least squares. This method also allowed for the smoothing of the composite station data over some latitude range. After some experimentation the fit was applied out to ±2° of latitude about the equator (Figure. 3.9). This fit had the least cross-equatorial slope in the deep water, with the curvature term contributing at least five times more to the polynomial curve than the slope term in most locations. To match the end stations of the fit to the adjacent stations an artificial dynamic height profile was constructed at each end of the region by evaluating the fit at ±2°. Regular geostrophy was used to calculate

transports outside of this equatorial band.

Using this method and the ZVS of $\theta = 1.3°C$ there is an estimated net westward transport of LCPW of 14.8×10^6 m^3 s^{-1} between 5°S and 10°N at 165°E. Of this 11.1×10^6 m^3 s^{-1} occurs between 2°S and 2°N, and of this amount 7.7×10^6 m^3 s^{-1} occurs as the result of applying the velocity at the DCL to the large unsampled area between 4000 db and the bottom between 2°S and 2°N which is the sum of the bottom triangles fro the station pairs in the equatorial band. Thus the estimate of the westward transport of LCPW is strongly dependent on the representativeness of the fit at the equator and the extrapolation of it to below the DCL. This water presumably supplies the DWBC at 10°N in the East Mariana Basin. The transport of NPDW through the section is calculated as 0.9×10^6 m^3 s^{-1} to the east.

The discrepancies between transport estimates for the LCPW and the NPDW in the two sections in the East Mariana Basin most likely arise from some combination of three factors. One possibility is that the zonal section at 10°N does not resolve the DWBC in the East Mariana Basin as well as that in the Central Pacific Basin. This sampling problem may be related to the topography in the western basin being more abrupt than that of the Central Pacific Basin. Another possibility is that the transport of the DWBC in the East Mariana Basin may simply vary in time. The last and strongest possibility is that the transport estimate from the meridional section at 165°E may be aliased by equatorial waves. The bulk of the LCPW moving westward through the section is found between 2°S and 2°N, where equatorial geostrophy was applied with over half of that resulting from the extrapolation of velocity into the bottom triangles. The transports estimated in this equatorial band could vary wildly in comparison with the actual mean transports if the few stations going into the composite stations were aliased by equatorial waves. The divergence of 2.0×10^6 m^3 s^{-1} in the NPDW between the two sections is less worrisome than the convergence of 9.8×10^6 m^3 s^{-1} in the LCPW, but may also result from some of the problems mentioned here. It is argued below using conservation of mass in the context of the overall circulation of LCPW in the near-equatorial Pacific Ocean that the smaller estimate of LCPW water transport through 10°N
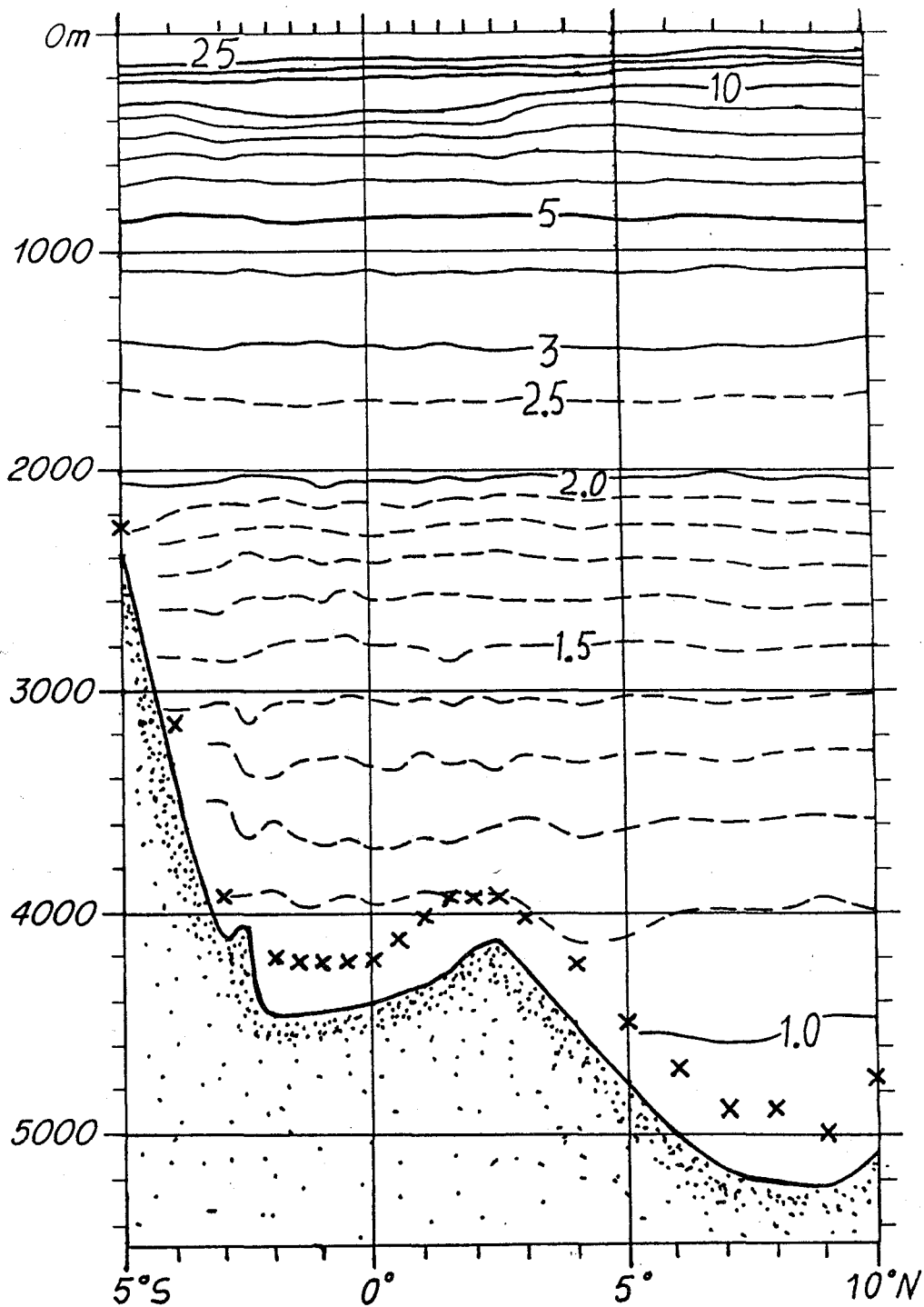
Figure 3.8: Section profile of average potential temperature, θ, in °C at 165°E using the composite section constructed from the six U.S.-P.R.C. TOGA sections. Vertical exaggeration is 500:1. The x's mark the deepest station depth at each location. The bowl in the bottom isotherms at the equator indicates a westward velocity increasing toward the bottom there. See Figure 3.1 for section location.
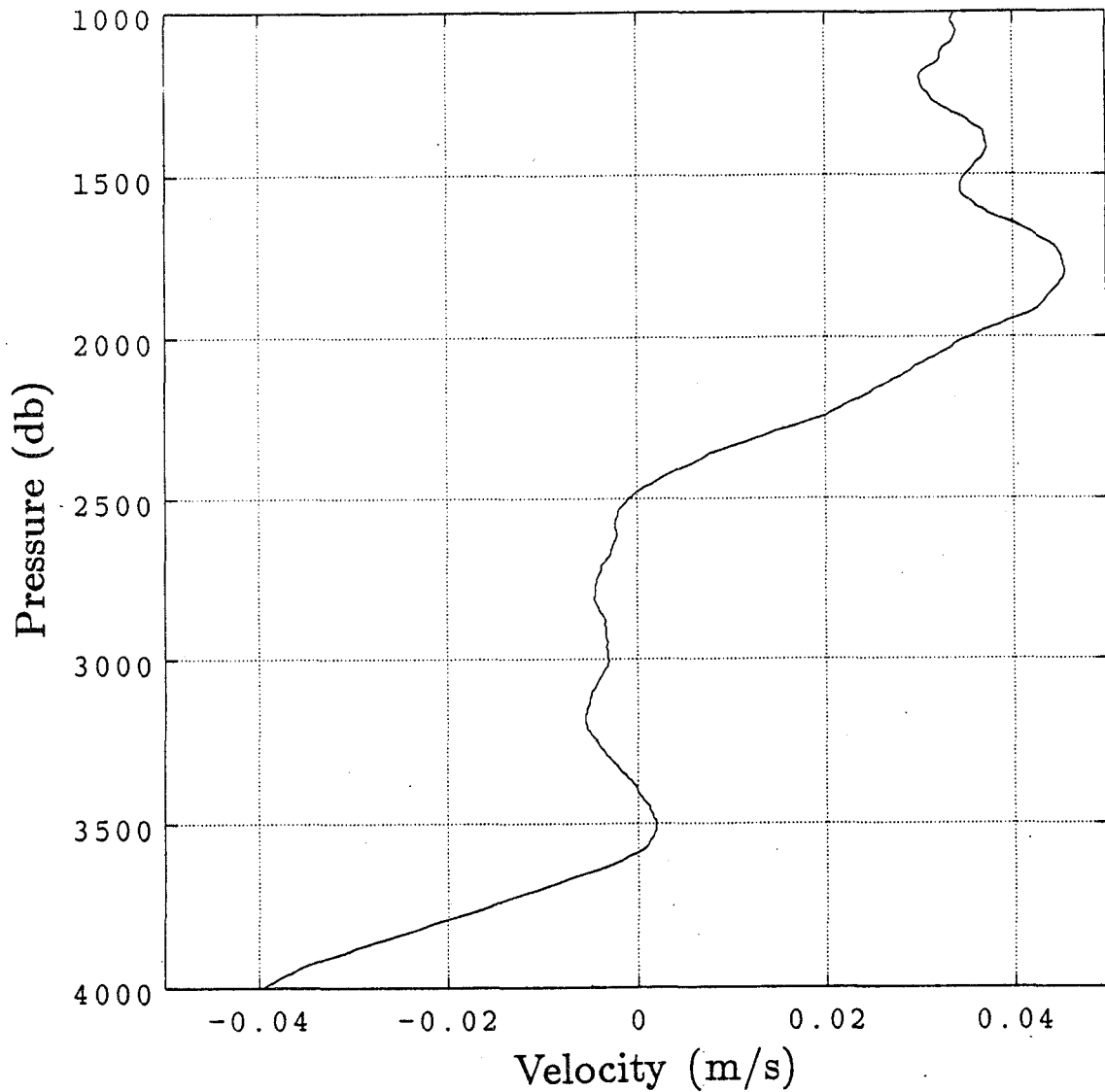
Figure 3.9: Velocity estimated from the curvature coefficient of a second order polynomial fit to dynamic height on constant pressure surfaces from 2°S to 2°N using the average of station data from six U.S.-P.R.C. TOGA sections at 165°E plotted against pressure. Velocity increases westward toward the bottom in the LCPW. The DCL is at 4000 db over this latitude range.

in the East Mariana Basin is more likely to be close to the actual mean transport through the basin than that made with the composite U.S.-P.R.C. TOGA section at 165°E (Section 3.4).

In the Central Pacific Basin, the bulk of northward flowing DWBC of LCPW is found between stations 86 and 96, and is once more associated with silica-poor water (Figure 3.2) found in the western boundary region. Since the thermal wind signal of the DWBC is spread out over many stations, the transport estimate here is more robust than that in the East Mariana Basin, and the lack of another estimate nearby is not worrisome. The net southward transport of 0.2×10^6 m^3 s^{-1} of NPDW in the basin is negligible, and suggests that the NPDW in the interior of the tropical Pacific is moving very sluggishly.

In the Northeast Pacific Basin, the flow in both the LCPW and the NPDW is southward. This southward flow is mostly confined to within 1000 m of the bottom along the flank of the East Pacific Rise, where the potential isotherms can be seen sloping downward into the rise as they approach it. Consistent with this, there is not much change in dissolved-silica concentration in the LCPW of the basin, but the higher values do occur where the transport is southward, east of station 150. Concentrations of dissolved-silica in the NPDW above increase significantly (Figure 3.2). It is the high silica NPDW between Stations 170–190 which is moving south.

3.4   Conclusion

The circulation of NPDW is fairly clear. The net transport of NPDW across the three central basins of the North Pacific at 10°N is 2.7×10^6 m^3 s^{-1} southward. The transport of NPDW in each basin is of this order. There is 1.1×10^6 m^3 s^{-1} of the water in the NPDW class that is most southern in water-mass properties estimated to be moving north in the East Mariana Basin. The net southward transport of 3.6×10^6 m^3 s^{-1} of NPDW that is estimated in the Northeast Pacific Basin is all of the most silica-rich NPDW, originating from the north and flowing away from its

source over the western flank of the East Pacific Rise. The net transport distribution is consistent with a net southward transport of NPDW out of the North Pacific and qualitatively agrees with results which indicate that this water continues to flow south through the South Pacific (Wunsch et al., 1983). However, water in the peripheral basins, the Philippine and Guatemala basins, is not included in the estimate made here and the latter area especially may add southward transport of NPDW to the net transport across the Pacific at this level. The more important result is that the ZVS's chosen for each basin result in a circulation of NPDW in that basin consistent with its water-mass properties as discussed above.

The results of the estimates of LCPW transport at 10°N and 165°E can be combined with observations near 12°S (Taft et al., 1990), 159°W near the equator (Firing, 1989), and 138–153°S near the equator (Ponte and Luyten, 1989) to give a consistent scheme for the circulation of LCPW between 12°S and 10°N (Figure 3.7)

An estimated 12.2×10^6 m^3 s^{-1} of LCPW moves north below a ZVS of $\theta = 1.22$–1.26°C at 12°S (Taft et al., 1990). The shallower part of this water branches westward over the Melanesian Basin where an estimated 14.8×10^6 m^3 s^{-1} is found moving west from the average of three U.S.-P.R.C. TOGA CTD sections at 165°E from 10°S to 10°N below a ZVS of $\theta = 1.2$°C. From here this branch moves northwest to where an estimated 5.0×10^6 m^3 s^{-1} moves north below the same ZVS at 10°N, the bulk in a DWBC near the Caroline Islands. These latter two estimates indicate a convergence of nearly 10×10^6 m^3 s^{-1} of LCPW between the equator and 165°E and 10°N and 150°E. Such a large convergence is not likely over such a small distance, and it is argued below that by conservation of mass arguments the smaller of the two estimates for the DWBC transports is more likely applicable to both locations.

The deeper colder LCPW is blocked by topography and cannot flow westward across the Melanesian Basin. This water is constrained to flow northward in the Central Pacific Basin. Using a ZVS of $\theta = 1.4$°C, an estimated 8.1×10^6 m^3 s^{-1} of LCPW moves northward, the bulk in a DWBC near the Marshall Islands. This gives a net northward transport of 13–23×10^6 m^3 s^{-1} for these two basins. This amount is roughly equal to or greater than the 12×10^6 m^3 s^{-1} estimated to flow north at

12°S below similar ZVS's (Taft et al., 1990). This agreement is worrisome since some of the LCPW should flow into the interior and upwell between 12°S and 10°N. However, in the Northeast Pacific Basin a choice of $\theta = 1.65°C$ as a ZVS results in an estimated southward transport of 4.7×10^6 m^3 s^{-1} below, bringing the net transport of LCPW to $8-18 \times 10^6$ m^3 s^{-1}, the lower bound of which is now less than that estimated at 12°S, as expected. The net transport of LCPW at 10°N should not exceed that at 12°S. This constraint indicates that the mean transport of LCPW in the East Mariana Basin is closer to the 10°N estimate of 5.0×10^6 m^3 s^{-1} than the 165°E estimate of 14.8×10^6 m^3 s^{-1} since the estimated net northward transport of LCPW north of the equator exceeds the estimate to the south of the equator when the large estimate made at 165°E is used for the transport through the East Mariana Basin.

This southward transport of LCPW at 10°N in the Northeast Pacific Basin helps to explain some puzzling features in some vertical profiles of currents taken near the equator. PEQUOD White Horse profiles taken in April 1982 (Ponte and Luyten, 1989) show strong westward flow below 3500 m from 138-148°W within 0.5° of the equator. Plots of the mean zonal velocity of all profiles taken during three cruises in January 1981, and February and April 1982 [from 3-9 profiles at each location, see Ponte (1988) for details], generously supplied by Rui Ponte, allow for conservative estimates of the transport below 3500 m within 0.5° of the equator, ranging from $2-4 \times 10^6$ m^3 s^{-1}. At 153°W the flow is not observed, it is presumably deflected by a seamount just upstream (Figure 3.7). This westward flow along a ridge near the equator is presumably supplied by the southward flow observed to the north.

A westward flow of 6×10^6 m^3 s^{-1} is observed centered at 4000 m, 2.5°S, 159°W (Firing, 1989). Here the transport estimate is the mean from 42 profiles at each location taken over 16 months, and is more reliable and thorough than those rough estimates to the east made above. There is little doubt that this flow is the same jet as that to the east discussed above, deflected south by the Line Islands to the sill at 155°W (Section 3.1). Like the jet to the east it is also consistent with the transport estimate and ZVS for the LCPW in the Northeast Pacific Basin.

Taken together, these observations show that the near-equatorial jet is the result of influence of bathymetry on the interior flow, not a branch of a DWBC. Some such result was to be expected, since the current flows to the west, and could not have directly originated from either of the DWBC's to the west. Of course, the southward interior flow in the Northeast Pacific Basin is puzzling from the standpoint of simple flat-bottom Stommel-Arons dynamics (Subsection 1.1.1). This puzzle is addressed by considering the manner in which the large-scale upward slope of the bottom to the southeast from about 15°N toward the equator and the East Pacific Rise modifies the flat-bottom Stommel-Arons dynamics (Section 4.3).

Thus some of the LCPW flowing north at 10°N in the Central Pacific Basin probably flows north west of the Hawaiian Ridge through the Northwest Passage. Analysis of a recent transpacific CTD section at 24°N suggests that 4.9×10^6 m^3 s^{-1} of LCPW moves north at this latitude, nearly all of it in the interior west of Hawaii (Bryden et al., 1990). If some of this water flows north through the East Mariana Basin and some through the Central Pacific Basin at 10°N, the rest of the DWBC in the Central Pacific Basin at 10°N would seem to be deflected to the east by the Hawaiian Ridge, entering the Northeast Pacific Basin through the Clarion Fracture Zone and flowing east [only 0.4×10^6 m^3 s^{-1} is estimated to flow to the north around the eastern side of the Hawaiian Ridge (Edmond et al., 1971)]. From there the LCPW moves southeastward up the bottom topography, perhaps joining and mixing with more silica-rich water flowing south from further north, turns west near the crest of the ridge and at the equator to form a jet which re-enters the Central Pacific Basin just south of the Line Islands.

Thus some of the supply of LCPW to the Pacific north of 10°N is contained in the DWBC flowing along the Caroline Islands in the East Mariana Basin, and some in the DWBC of the Central Pacific Basin. Some of the water in the former DWBC probably turns west to supply bottom water to the Philippines Basin. Some of the water in the latter DWBC apparently turns east and returns south in the Northeast Pacific Basin to be recirculated. This assertion is supported by the water-mass properties. The high salinity and low dissolved-silica concentration observed

in the LCPW in the East Mariana Basin with respect to the two basins to the east support the conclusion that the East Mariana Basin DWBC is supplied most directly from the south. The lower salinity and higher dissolved-silica concentrations measurements in the Central Pacific and Northeast Pacific Basins, which are similar in the LCPW, indicate the water there is somewhat older than that to the west, and are in accord with the recirculation proposed (Figures 3.3 and 3.5).

Chapter 4

Theoretical Considerations

Here models are used to interpret the observed circulation patterns of bottom water in the equatorial Indian and Pacific Oceans as described in Chapters 2 and 3. A Stommel-Arons scheme is used to predict the strength and direction of deep western boundary currents (DWBC's) in the western Indian and central Pacific Oceans. A model of a meridional inertial jet on a sloping bottom (Stommel and Arons, 1972) is reformulated on the equatorial β–plane to explore the behavior of a DWBC in the vicinity of the equator, specifically in the Somali Basin. The influence of topography on the flow of bottom water at 10°N in the Northeast Pacific Basin is discussed. Estimates of the vertical upwelling rates at the top of the bottom water are made from mass budgets in near-equatorial regions of the two oceans. Using these upwelling rates in heat budgets allows for the calculation of vertical diffusivities in these areas. The vertical diffusivity at the top of the bottom water in the Somali Basin is larger than previous estimates for the bottom water in other locations and the present estimate in the near-equatorial Pacific Ocean.

4.1   A Stommel-Arons Framework with Basin Geometry

The Stommel-Arons framework for the interior deep circulation gives a theoretical interpretation of observations of deep circulation. A review of the theory and usual simplifications is found above (Section 1.1). The simplifying assumptions made here are slightly different.

4.1.1 Model Description

The ocean bottom is assumed to be flat, with uniform upwelling at the top of the bottom water. Knowing magnitudes and locations of the sources and sinks and treating the basins as otherwise horizontally enclosed below the top of the bottom water allows an estimate of a uniform upwelling w. Only the vertically averaged circulation is considered. With these assumptions the meridional velocity, v, in the interior can be calculated using a form of the planetary geostrophic relation

$$\frac{2\Omega\cos\theta}{a}v = \frac{2\Omega\sin\theta}{H}w ,\qquad (4.1)$$

where Ω is the earth's rotation rate, θ the latitude, a the radius of the earth and H the layer thickness.

The magnitude and direction of the DWBC transport, $T(\theta)$, can be calculated by continuity, using

$$T(\theta) = wA(\theta) - a\tan\theta\, wL(\theta) - \sum_{i=1}^{n} S_i \mathcal{H}(\theta_i - \theta) ,\qquad (4.2)$$

where $A(\theta)$ is the area north of θ, $L(\theta)$ the basin width at θ, and S_i the n source and sink strengths. The first term on the RHS is the volume of water upwelled per unit time north of θ, the second term is the interior transport at θ, and the third term is the contribution from the sources and sinks. The $\mathcal{H}(\theta - \theta_i)$ multiplying each source and sink is the Heaviside or step function, indicating that this term is only applied south of the latitude θ_i of each source or sink.

For each basin the depth of the top of the bottom water and the strengths and locations of the sources and sinks are selected using material from the earlier Chapters 2 and 3. The basin geometry is determined by using historical bathymetry which has been processed into average depths for each degree of latitude and longitude. The width of each basin as a function of latitude $L(\theta)$ is determined by using the number of degree squares below the top of the bottom water or between the crests of the ridges defining the basin if these do not extend to the top of the bottom water. Here the top is depth of the top of the bottom water entering the basin. The area of the basin north of a given latitude $A(\theta)$ is the integral of $L(\theta)$ from the

84

northernmost extent of the basin toward the south. The uniform upwelling rate w is the sum of the sources and sinks divided by the total area of the basin.

The exact structure of the interior circulation is not calculated, the fact that it is poleward and satisfies the no-flux boundary condition on the eastern boundary is sufficient for any inferences made with the model. The primary result of the model is the magnitude and direction of the DWBC transport, which can be compared with estimates from analysis of observations.

The model is not applied to the Atlantic Ocean for several reasons. The deep circulation of the Atlantic is complicated, with sources of deep water of differing densities to the north and south. The depths of the isopycnals defining these layers varies significantly with latitude (Whitehead, 1989). The magnitude of the communication with the eastern basins in the Atlantic has not been well estimated either. Finally, observational work concerning the Atlantic is not presented here.

4.1.2   The Western Indian Ocean

The only known bottom water source for the Somali Basin is the flow through the Amirante Passage from the Mascarene Basin. The 3800 m isobath is picked to define the deep basin geometry for this basin because it is close to the estimated ZVS for the inflow (Subsection 1.2.2). A unit source representing the flow through the Amirante Passage between the Somali and Mascarene Basins is introduced into the DWBC at 8.5°S. Since the basin is closed below 3800 m everywhere except this passage the bottom water must upwell in the basin.

South of 8.5°S there is little area in the basin and only a small northward DWBC fed from the southward interior circulation as it re-encounters the boundary (Figure 4.1). At 8.5°S the unit source from the Amirante Passage is introduced and the recirculation of interior flow augments the DWBC size which is near 1.2 from 8.5°S to 6°S. At 4°S the DWBC strength is back to unity. South of the equator the model agrees well with the observations, since the volume transport of bottom water estimated at 3°S is close to that estimated at Amirante Passage (Subsections 2.2.1

and 1.2.2) in a pattern similar to that in the model. By 4°N the DWBC in the model has fed all its transport into the interior and reverses direction, flowing southward north of 4°N. However, the observations suggest that the DWBC does not cross the equator, but turns east there (Subsection 2.2.2). This difference is a significant one, and may indicate the importance of non-uniform upwelling within the basin or the large values of vertical diffusivity calculated for the basin (Section 5.1). An attempt to model the behavior of a DWBC as it approaches the equator follows (Section 4.2). The southward flow, fed by the poleward interior which returns to the western boundary, is a maximum of only 0.1 at 7.5°N. This model result is once again in accord with observations, which do not reveal a significant DWBC in the bottom water near 7°N, but do reveal the lowest dissolved-oxygen concentrations and relatively warm water in the interior, suggesting that the oldest bottom water in the basin, perhaps moving south, is located there (Subsection 2.2.3).

The Arabian Basin has a different source of deep water of different density, and thus is treated separately, with a unit source introduced to the DWBC at the Owen Fracture Zone at 10.5°N. The 2800 m isobath, close to the ZVS estimated for the basin (Subsection 2.3.4) and the ridge crests where they are deeper than 2800 m are used to define the basin geometry (see Figure 1.1 for the 4000 m isobath). Here the assumption is made that these ridges exert sufficient topographic control to guide and contain most of the flow beneath the ZVS within the basin even where they are occasionally deeper than the ZVS.

In the Arabian Basin the bottom water source enters through the Owen Fracture Zone and the strong DWBC flow is all to the southeast along the Carlsberg Ridge. If the source were introduced through the gap in the Chagos-Laccadive Ridge at 3.5°S the DWBC would flow in the opposite direction up to 10.5°N (Figure 4.1). Since the observations suggest that the DWBC flows southeastward along the Carlsberg Ridge (Subsection 2.3.4), the model results suggest that given that flow direction, the source of the bottom water in the Arabian Basin is probably the Owen Fracture Zone.
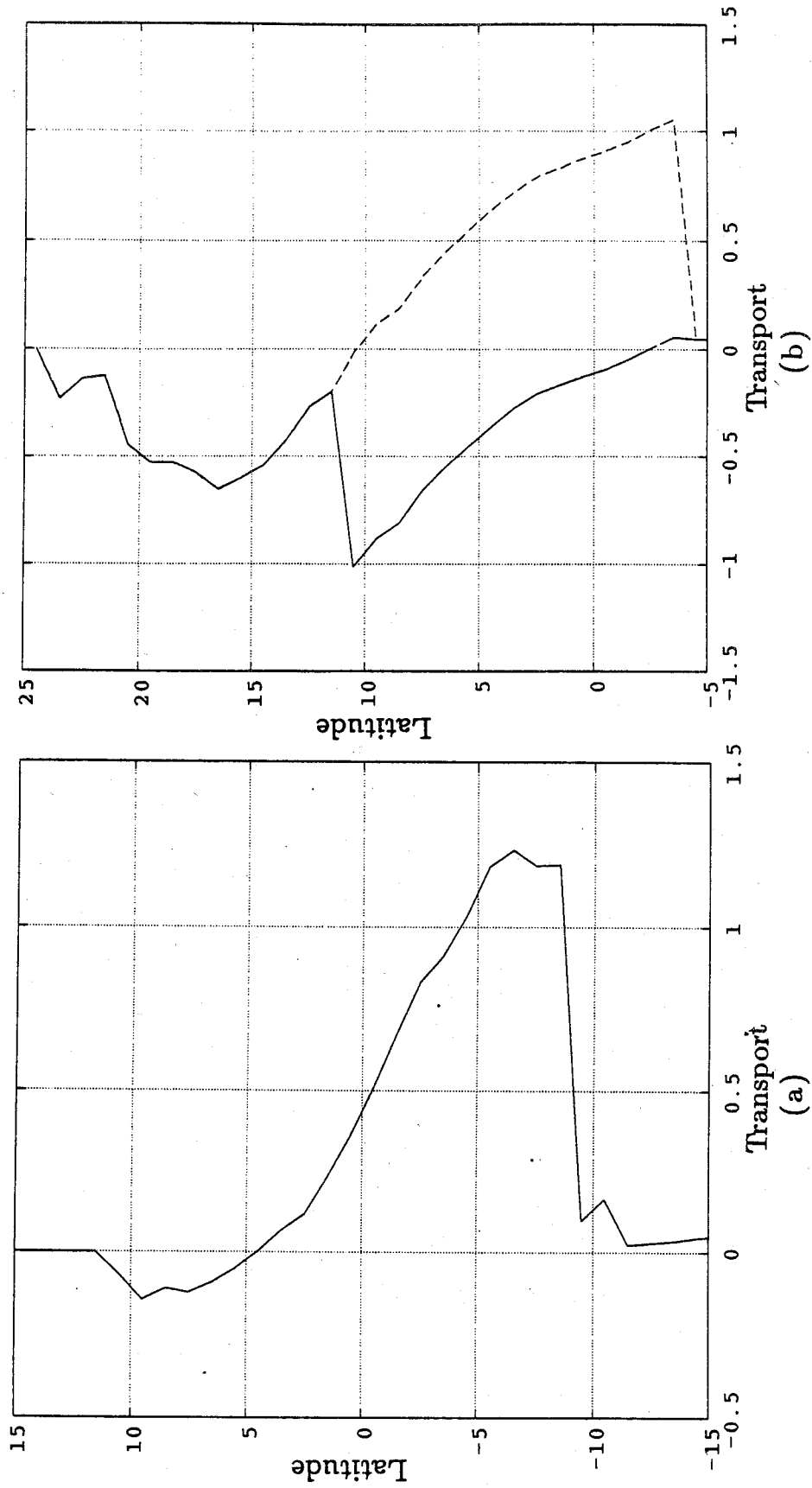
Figure 4.1: (a) DWBC strength as a function of latitude in the Somali Basin. (b) The unit source DWBC introduced to the Arabian Basin at 10.5°N is of different origin. This runs as a DWBC southward along the Carlsberg Ridge (solid line). If the source is introduced at 3.5°S the flow in the DWBC is northward south of 10.5°N (dashed line).

4.1.3 The Central Pacific Ocean

The top of the bottom water in the central Pacific is near 3600 db at 12°S (Subsection 1.2.3) and 3600 db at 10°N (Section 3.2). Thus the depth of the top of the bottom water and hence the basin boundary is selected as 3600 m for the Pacific. Area calculations exclude the basins east of the East Pacific Rise, west of the barrier composed of New Zealand, the Kermadec, Tonga and Solomon Islands and the Eauripik, Mariana and Sitio-Iozuma ridges, and north of the Aleutian Islands.

The unit source feeding the DWBC enters at 55.5°S (Figure 4.2). At 12°S, near the Samoan Passage, the DWBC transport has diminished to 0.8 of its unit source strength. Again south of the equator the model is in accord with the observations, since near the source at 43°S and 28°S the DWBC transport is estimated at 20×10^6 m^3 s^{-1} but by the Samoan Passage the estimate stands at 12×10^6 m^3 s^{-1} (Subsection 1.2.3), slightly less than the transport predicted. By 10°N the DWBC is predicted to be only 0.3 of the original strength by the model. In contrast with the Somali Basin, the prediction of DWBC transport at 10°N is in relatively good agreement with the net observed transport of 8.4×10^6 m^3 s^{-1} (Section 3.3), being only slightly smaller than that observed. Of course the observed DWBC has split into two, a result of the complicated bathymetry not included in the model. In addition, the model takes no account of the southward flow in the Northeast Pacific Basin, probably another result of the bathymetry which is discussed below (Section 4.3). The model DWBC reverses direction at 22°N, flowing south above this latitude with a maximum amplitude of 0.4 at 50°N, supplied by poleward interior flow re-entering the boundary. This prediction seems in gross agreement with the suggestion of only interior flows of the water with most southern water-mass properties at 24°N and 35°N and the observation of a westward flowing northern boundary current off of the Aleutian Islands which would feed this southward flow at the western boundary (Subsection 1.2.3). However, the model does not account for the large westward jet observed in the bottom water of the eastern equatorial Pacific (Subsection 1.2.3).
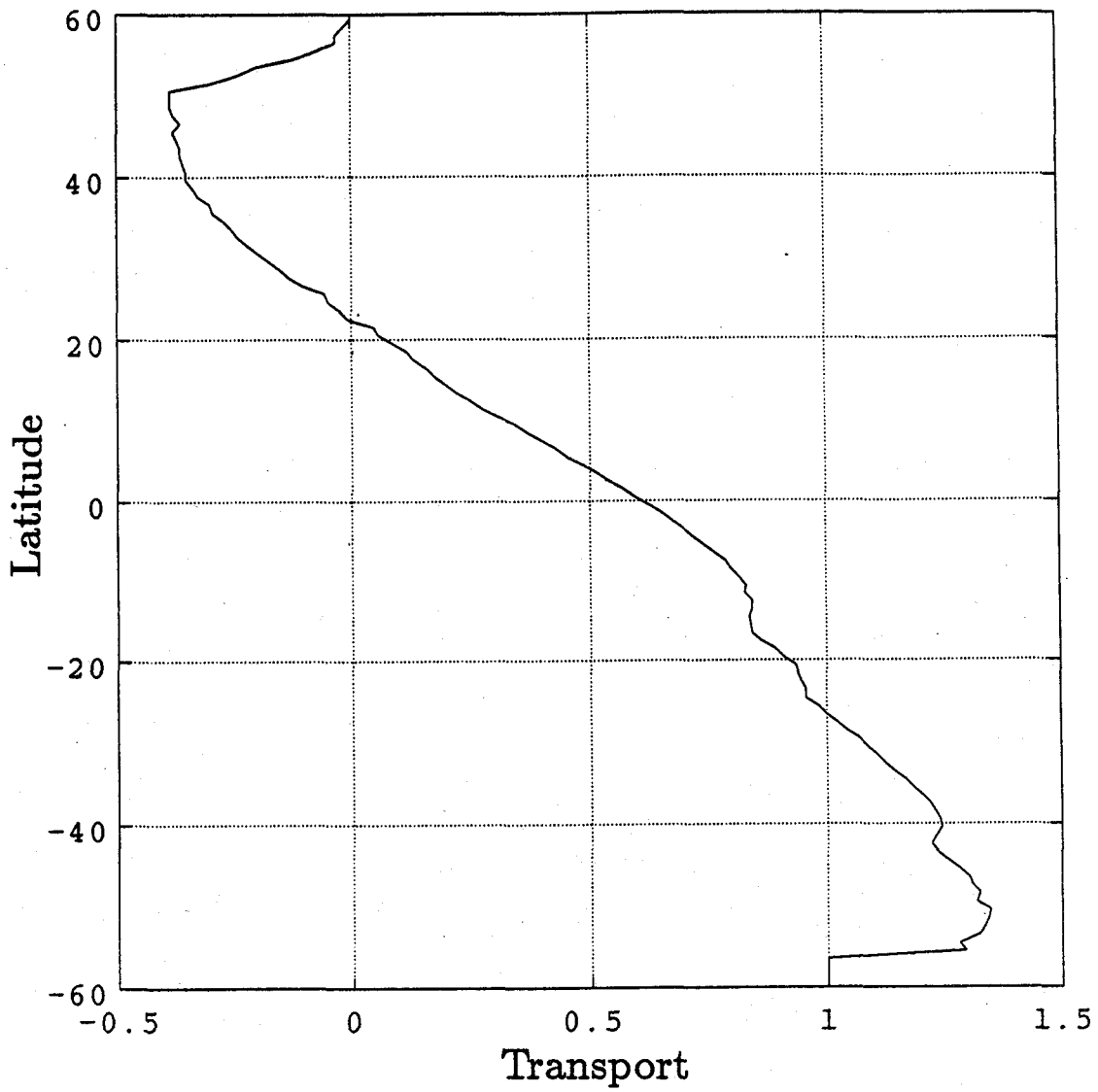
Figure 4.2: The DWBC strength as a function of latitude for the central Pacific basins. A unit source enters the basin at 55.5°S. Near the Samoan Passage at 12°S the DWBC is 0.8 of the source strength. By 10°N it has diminished to 0.3 of the original source strength. The DWBC reverses direction at 22°N.

4.2 A Meridional Inertial Current on a Sloping Bottom

The dynamics of DWBC's in the vicinity of the equator is sparsely treated in the literature. Here a model of an inertial current traveling over a sloping bottom originally formulated to explain the unexpected width and bottom trapped nature of DWBC's (Stommel and Arons, 1972) is modified and extended to explore this problem. The original formulation did not take the β-effect into account in calculating velocities, and thus gave poor results with large changes in latitude. In the reformulation of the model presented below the equatorial β-plane approximation is applied consistently. This reformulation allows a consistent exploration of how the structure of a meridional inertial current travelling over a sloping bottom changes as it approaches and then crosses the equator.

The simplest place to apply this model is in the Somali Basin, where the northward flowing DWBC in the southern part of the Somali Basin flows over a smooth continental rise (Subsection 2.2.1). The model may also be applicable to the DWBC's in the Atlantic and Pacific Oceans. However, the situation is more complicated in each case. In the Atlantic the northward flowing DWBC of LCPW appears to transpose sides to sit on the western flank of the Mid-Atlantic Ridge. The reason for this transposition is not clear (Subsection 1.2.1). In the Pacific the location of the deep western boundary is obscure in the vicinity of the equator, and the current observed at 12°S is shown to be split into two currents by the topography by 10°N. A near-equatorial zonal jet further complicates matters by bringing bottom water that has already crossed the equator back to the western boundary there (Section 3.4). Therefore the model is scaled using the southern section profiles of stacked-σ (See Appendix A for an explanation of stacked-σ). from cruises CD 86–19 and CD 87–25 in the somewhat simpler Somali Basin (Figures A.4 and A.20).

4.2.1 Model Formulation

The model is a reduced gravity equatorial β–plane construction, with a resting upper layer of infinite extent, and a moving lower layer which encounters a bottom that slopes linearly upward to the west. (See Figure 4.3 for the geometry). The origin of the coordinate system is placed at the intersection of the equator with the line at which the interface defining where the two layers would meet the bottom slope if both layers were everywhere at rest. The x–axis points eastward, the y–axis northward, and the z–axis upward. Thus with a bottom of slope $-s$ the bottom b is defined by $b = -sx$. The thickness of the lower layer is represented by h so the height of the interface between the layers i is given by $i = h + b = h - sx$.

While the model is inviscid, a simple Rayleigh friction is carried through the initial development for the purposes of later discussion. The assumption that the current is primarily meridional and thus $v \gg u$ and $\partial/\partial x \gg \partial/\partial y$ simplify the horizontal components of the shallow-water momentum equation to

$$- \beta y v = -g'(h + b)_x \tag{4.3}$$

and

$$u v_x + v v_y + \beta y u = -g'(h + b)_y - rv , \tag{4.4}$$

where u and v are the east and north velocity components, β the planetary vorticity gradient, $g' = g\Delta\rho/\rho_0$ the reduced gravity where g is the gravitational acceleration, $\Delta\rho$ the density difference between the layers and ρ_0 the average density and finally r is the Rayleigh friction coefficient. The cross-stream momentum balance is geostrophic and the along-stream balance is among all the terms.

The continuity equation is

$$(uh)_x + (vh)_y = 0 . \tag{4.5}$$

Taking the curl of the horizontal momentum equation and using the continuity equation in the result yields the vorticity equation,

$$u \left(\frac{\beta y + v_x}{h} \right)_x + v \left(\frac{\beta y + v_x}{h} \right)_y = -r \left(\frac{v_x}{h} \right) , \tag{4.6}$$
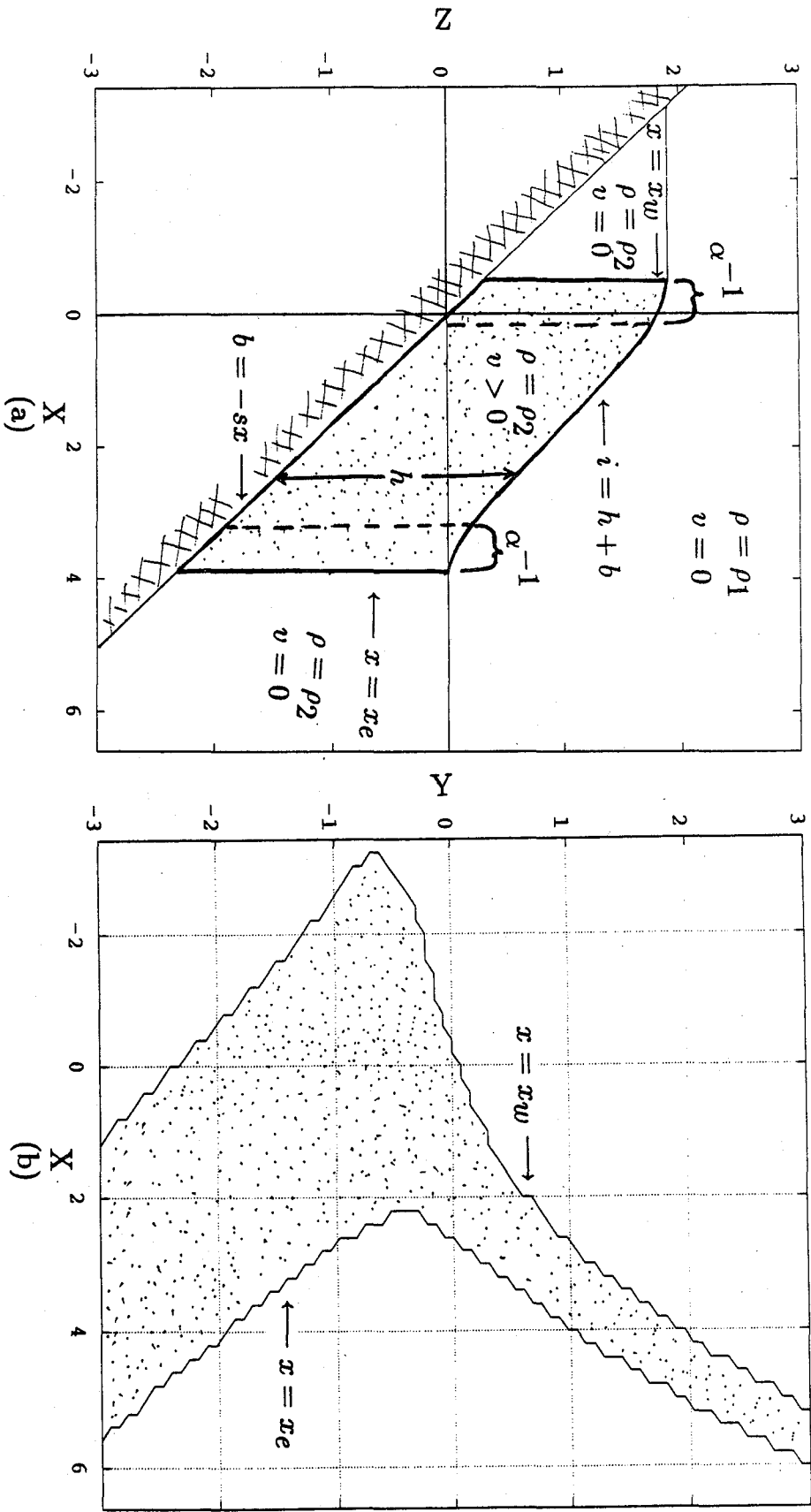
91

Figure 4.3: (a) Cross section of the jet (stippled area) at $y = -2$. The x-axis is scaled by $\alpha^{-1} = 36.8$ km, the z-axis by $H = 150$ m. Adjustment regions of width a Rossby radius of deformation, α^{-1}, are shown by the dashed lines. (b) Overhead of the jet (stippled area). The y-axis is scaled by $y_o = 372$ km. If the axes were plotted dimensionally, the y-axis would be about 6 times the length of the x-axis.

which relates the advection of potential vorticity $Q = (\beta y + v_x - u_y)/h$ to the dissipation due to Rayleigh friction. Only the u_y term has been eliminated from Q. With the further assumption of an inviscid system the RHS of 4.6 can be dropped and potential vorticity is conserved along streamlines.

With a uniform potential vorticity $Q_o = -\beta y_o/H$, where y_o is some distance south of $y=0$ and H is a characteristic thickness of the current at this latitude, potential vorticity conservation along with the assumption of cross-stream geostrophic balance 4.3 yields an equation for the layer thickness h within the stream,

$$h_{xx} + \frac{\beta^2 y_o y}{g'H} h = \frac{-\beta^2 y^2}{g'} \ , \tag{4.7}$$

a second order non-homogeneous differential equation in x. The solution south of $y=0$ is

$$h = -\frac{y}{y_o}H + p \exp\left(-\frac{\beta y_o}{(g'H)^{1/2}}\left(\frac{y}{y_o}\right)^{1/2}x\right) + q \exp\left(\frac{\beta y_o}{(g'H)^{1/2}}\left(\frac{y}{y_o}\right)^{1/2}x\right) \ , \tag{4.8}$$

where p and q are functions only of y once r and s are chosen. The explicit forms of the coefficients, which change north of $y = y_c$, are omitted for the sake of brevity and clarity.

The solution appears to have only two free parameters giving the amplitudes of the y–dependent coefficients. However, the eastern and western boundaries of the stream x_e and x_w are free to vary, so actually there are four free parameters. Thus four constraints are needed to close the model.

Conservation of transport, r, provides one constraint,

$$r = -\int_{x'=x_w}^{x_e} vh\,dx' \ . \tag{4.9}$$

This constraint holds r constant over all latitudes.

At the eastern and western boundaries there should be no flow into or out of the jet, i.e. $u = 0$. Applying this condition to 4.4 with $r = 0$ and integrating along the jet (in y) shows that

$$B = g'i + \frac{1}{2}v^2, \tag{4.10}$$

where i is again, the interface height. The Bernoulli function B must be conserved along the streamlines defining the edges of the jet.

The current thickness on its eastern edge should match that on the western edge of the motionless interior, so that $h = -sx$ at $x = x_e$. The current velocity is chosen to match that of the quiet interior so that $v = 0$ at $x = x_e$. The assumption that $v \gg u$ has been applied again. These conditions provide the second and third constraints and set $B = 0$ at $x = x_e$ in 4.10.

At the western boundary of the jet 4.10 applies for the fourth constraint, but its nature is different on either side of a critical latitude which occurs south of $y=0$ at $y_c = -y_o((sg'^{1/2})/(\beta y_o H^{1/2}))^{2/3}$. South of y_c if the thickness of the moving layer were to go to zero at its western edge there would be a reversal in the meridional velocity. To keep the model current simple, the thickness is kept finite, and the velocity is required to vanish on the western edge so that $v = .0$ at $x = x_w$, where the assumption of a meridional nature in the jet is applied for the last time. This condition keeps the stream flowing everywhere northward and with the assumption that transport is conserved fixes the height of the interface at a constant value at the western edge. A consequence of this condition is a pool of quiet water to the west of the stream, which points to the fact that this model is not strictly one of a boundary current, but a meridional inertial jet. The jet does not lose or gain water from or to the interior as the DWBC does in the Stommel-Arons framework. North of y_c the western edge of the moving layer meets the bottom, so $h = 0$ at $x = x_w$. This condition is substituted for that of vanishing meridional velocity at the western edge of the jet. This change of boundary conditions frees the western edge of the current to fall to the north and speed up, converting its Bernoulli head to kinetic energy.

The particular part of the solution is $h_p = -(y/y_o)H$. The homogeneous solution is a pair of exponential functions which grow and decay in x. The coefficients of these functions are found by setting $v = 0$ at $x = x_e$ and applying the latitude-dependent boundary condition at the western edge of the stream. The substitution of these expressions into 4.9 results in an expression for τ which depends on meridional

location y, bottom slope s and the current width $\Delta x = x_e - x_w$. Since everything but Δx is fixed the proper value of Δx to return the chosen τ can be solved for by iteration at any y. Applying the expressions for the coefficients along with the value of Δx at each y to the condition $h = -sx$ at $x = x_e$ determines x_e. Then the value of $x_w = x_e - \Delta x$ can be found by subtraction, giving 4.8.

At the equator, $y=0$, there is a regular singularity in 4.7, and the interface height $i = h + b = 0$ to avoid infinite meridional velocities and connect smoothly to the motionless interior at $x = x_e$. Thus $x_w = 0$. Potential vorticity and transport are conserved. At the equator potential vorticity conservation demands that

$$v_x = \frac{-sx\beta y_0}{H} , \tag{4.11}$$

where the requirement that $i = 0$ has been used to find $h = sx$. Integrating this relation and setting $v = 0$ at $x = x_e$ gives

$$v = \frac{s\beta y_0}{2H}(x_e^2 - x^2) . \tag{4.12}$$

Combining 4.12 and 4.9 gives

$$\tau = \int_{x'=0}^{x_e} \frac{s^2\beta y_0}{2H}(x'x_e^2 - x'^3)dx' . \tag{4.13}$$

Upon integration this can be written as an equation for x_e as follows,

$$x_e = \left(\frac{8H\tau}{\beta y_0 s^2}\right)^{1/4} , \tag{4.14}$$

and the problem is solved at $y=0$.

North of the equator, where $y > 0$, y changes sign and the solution for the thickness h can be written in the form

$$h = -\frac{y}{y_0}H + p\sin\left(\frac{\beta y_0}{(g'H)^{1/2}}\left(\frac{y}{y_0}\right)^{1/2}(x - x_w)\right)$$
$$+ q\cos\left(\frac{\beta y_0}{(g'H)^{1/2}}\left(\frac{y}{y_0}\right)^{1/2}(x - x_w)\right) , \tag{4.15}$$

which simplifies finding the analytic expression for the amplitude coefficients. The constraints are the same physically as those for $y_c \le y < 0$. The method of solution is also the same.

Except at the equator, the expressions for fields other than the thickness h are not given above. Other aspects of the solution can be easily determined however, the meridional velocity $v = -g'(h + b)_x/(\beta y)$ by the geostrophic relation, and the interface height by $i = h - sx$. The other quantity examined is v_x/h, which is most easily derived using the conservation of potential vorticity so

$$\frac{v_x}{h} = \frac{-\beta y_o}{H}\left(1 + \frac{yH}{y_o h}\right) . \qquad (4.16)$$

This quantity, by 4.6, is related to the dissipation of potential vorticity by Rayleigh friction. The model is inviscid, but the examination of this term gives some indication of the latitude south of which the inviscid model results could be expected to be valid.

4.2.2   Scaling the Model

Solutions for the model are calculated and plotted non-dimensionally. The model is scaled using the potential density section profiles for the sections near 3°S from CD 86–19 and CD 87–25. The DWBC can be seen in the isopycnals $\sigma_4 = 45.84$ to 45.92 which parallel the bottom slope on the western boundary (Figures A.4 and A.20). Here $g = 978$ cm s^{-2}, $f_o = -8.50 \times 10^{-6}$ s^{-1} (the value for 3.35°S, the median latitude of stations 109 and 110 from CD 86–19), $y_o = -372$ km (the distance from 3.35°S to the equator, which scales y), so $\beta = f_o/y_o = 2.285 \times 10^{-13}$ cm^{-1} s^{-1}, $H = 1.5 \times 10^4$ cm (the average distance from $\sigma_4 = 45.88$ to the bottom at stations 109 and 110 from CD 86–19, which scales z), $s = 0.00250$ (a 263 m bottom drop in the distance $\Delta x = 105.1$ km between stations 110 and 109), $\Delta \rho = 7.00 \times 10^{-5}$ g cm^{-3} (assuming the current shear exists between $\sigma_4 = 45.84$ and 45.91 at station 109 and an equal interval 0.01 σ units denser at station 110), the average density $\rho_o = 1.05$ g cm^{-3}, and finally, to use with Δx to calculate v and τ, $\Delta z = 2.83 \times 10^4$ cm (the drop of $\sigma_4 = 45.88$ between stations 110 and 109).

Using this information to arrive at derived quantities the reduced gravity $g' = g\Delta \rho/\rho_o = 0.0652$ cm s^{-2}, so the deformation radius (which scales x) is $\alpha^{-1} = (g'h)^{1/2}/f_o = 36.8$ km. Velocity scales with $V = (g'H)^{1/2} = 31.3$ cm s^{-1}, and

the bottom slope with $\alpha H = 0.00408$. Transport scales with $T = g'H^2/f_o = 1.73 \times 10^{12}$ cm^3 s^{-1}, and the dimensional $\tau = vH\Delta x$, where $v = (g'\Delta z)/(f_o x) = 20.7$ cm s^{-1}, so $\tau = 3.26 \times 10^{12}$ cm^3 s^{-1}. For this scaling and choice of physical values, the non-dimensional values of $\tau = 1.89$, and $s = 0.613$ allow solution of the problem and description of the jet. $Q = (\beta y + v_x)/h = -1$ non-dimensionally, which is -5.67×10^{-10} cm^{-1} s^{-1} dimensionally.

4.2.3   The Model Solution

The solution was evaluated between $y = -3$ to $+3$ (about 10°S to 10°N, approximately the latitude range of the Somali Basin) and for a width of 10 (368 km) in the x–domain (from $x = -3.4$ to $+6.6$). The discussion uses non-dimensional units, all of which can be dimensionalized using the scaling in Subsection 4.2.2.

The shape of the jet as seen from above reveals the change in nature of the jet at $y_c = 0.722$ (Figure 4.3). If the axes of this plot were to scale, the y–axis would be about six times longer than the x–axis. This plot in fact provides an a posteriori check on the semi-geostrophic approximation used in the model. The amplitude of the angle of departure from meridional in the jet edges gives a check on the departure of the jet from meridional. South of the critical latitude the largest slope does not exceed 5° in amplitude on the western edge of the jet, an acceptable value for the approximation to hold. North of $y = y_c$ the angle reaches its largest value at about 33° on the western edge between $y = -0.375$ and the equator. Thus the semi-geostrophic approximation may break down north of the critical latitude, making it difficult to draw too many conclusions from the behavior of this model there.

South of the critical latitude y_c the current width Δx is fairly constant, and the current travels to the west, up the bottom slope, as it moves northward. North of y_c the jet moves back down the slope and east, narrowing rapidly. Starting at $y = -3$ with $\Delta x = 4.2$, it widens to 5.0 at $y = -1.05$ and reaches a maximum of 5.4 at y_c. This change in current width is primarily due to the dependence of the

Rossby radius α^{-1} on y; the width of the core of the current remains unchanged but the adjustment regions on either side widen approaching the equator so the current width increases. However, north of y_c the current narrows rapidly, from $\Delta x = 2.6$ at $y=0$, to 1.1 at $y = 1.05$ to 0.6 at $y = 3$.

The two most basic fields of the jet are the interface height $i = h - sx$ and the velocity v. Below the evolution of these fields with increasingly northward latitude are described in light of conservation of potential vorticity and transport. (See Figure 4.4 for i and v plotted against x at the latitudes mentioned below).

South of y_c the mean current thickness h_{mean} decreases from 3 at $y = -3$ to 1.05 at $y = -1.05$, nearly linearly with latitude south of y_c. At the same time the maximum current velocity v_{max} increases from 0.19 to 0.49 while the slope of the interface in the center of the jet remains roughly constant. Potential vorticity is conserved mainly by decreasing the jet thickness as latitude decreases. Only in the adjustment regions on the edge of the jet does the v_x/h component of potential vorticity come into the balance, and even there the absolute value of v_x/h reaches a maximum of less then $0.5\beta y_o/H$ south of y_c. This means that the influence of Rayleigh friction, were it to be included in the model, would be small here compared to farther north.

Since by Bernoulli's Law the level of the western edge of the current cannot change south of y_c owing to the zero velocity condition, the current moves toward the coast to thin out as it moves northward. The current does not widen nearly so much as it thins out, in contrast with the previous model (Stommel and Arons, 1972) because the inclusion of β in the calculation of velocity allows the velocity to increase inversely with y for a constant interface slope; so as the current thickness decreases equatorward, velocity is increasing, and the two effects balance each other to maintain a constant transport without making the current wider.

At y_c the boundary condition at $x = x_w$ changes from $v = 0$ to $h = 0$. North of y_c the jet begins to move down the slope, converting its Bernoulli potential to kinetic energy and speeding up, with $i = 0$ at $y=0$ to avoid a singularity in the velocity and match to the motionless interior. The v_{max} shifts from the center of the jet
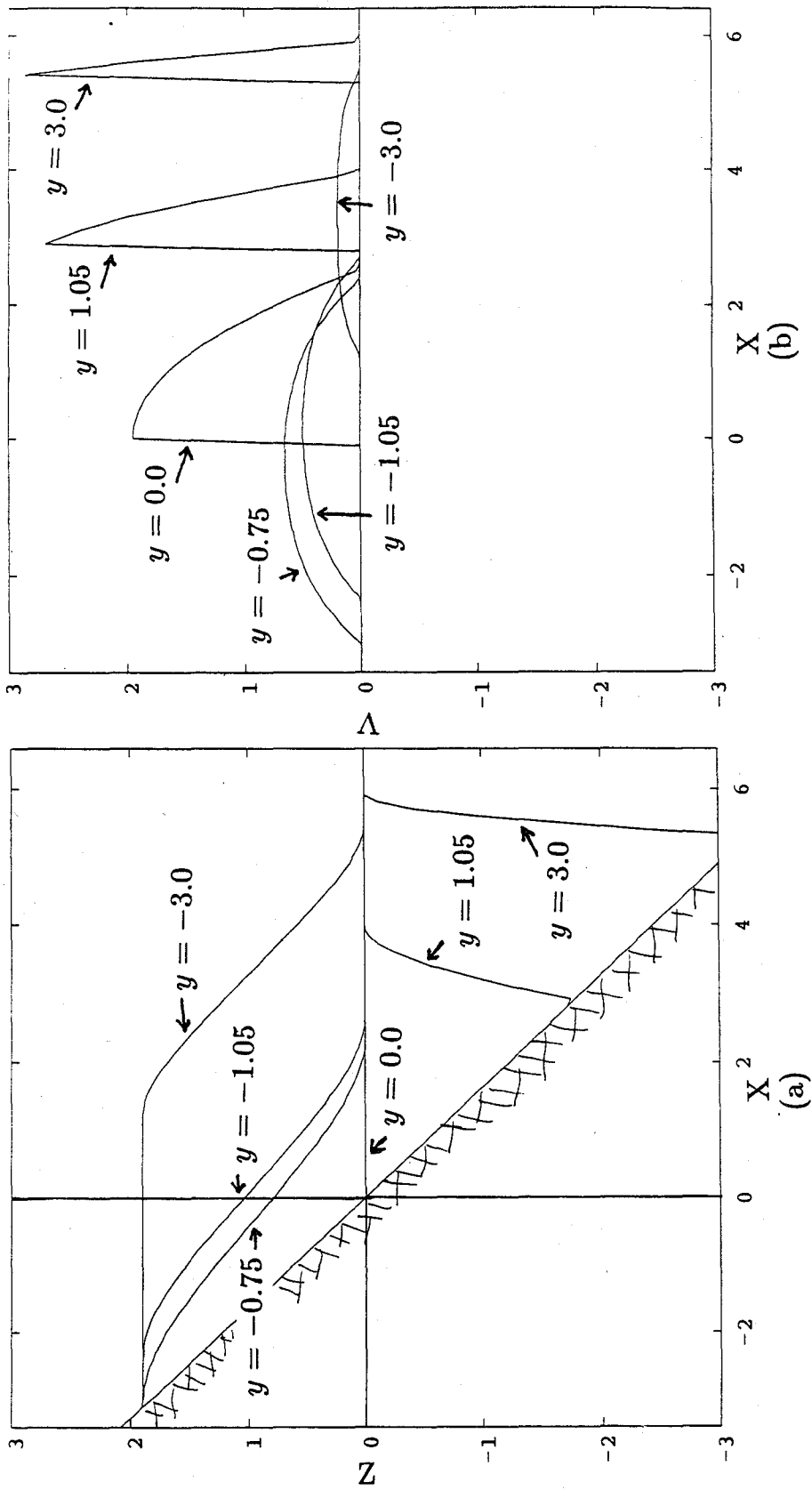
Figure 4.4: (a) Interface height i (scaled by $H = 1.5 \times 10^4$ cm) against x (scaled by $\alpha^{-1} = 36.8$ km) for $y = -3$, -1.05, -0.75, 0, 1.05, and 3. South of y_c, $h = i - b$ decreases inversely with y with a constant slope. North of y_c i falls rapidly, reversing slope at $y=0$. (b) Velocity v (scaled by $(g'H)^{1/2} = 31.3$ cm s^{-1}) for the same y's. The speed increases rapidly north of y_c.

for $y < y_c$ to the western edge for $y \geq 0$. At $y=0$ $v_{max}=1.9$ and $h_{max}=1.5$, with $\Delta x=2.6$. Since $\beta y = 0$, v_x/h alone must keep $Q = -1$. The current speeds up as it moves eastward down the bottom slope and increases thickness while decreasing width to conserve transport.

North of the equator 4.15 is oscillatory. The moving layer is terminated at the first point east of where the interface hits the bottom where $v = 0$ and $i = 0$, allowing only northward meridional flow. With this method of solution, the trends of increasing velocity and decreasing current width continue. As y increases, $-v_x/h > (\beta y)/h$ to keep $Q = -1$, thus v_{max} continues to increase rapidly to 2.7 at $y = 1.05$ and then more slowly up to 2.9 at $y = 3$. In addition the current width Δx decreases to 1.1 then 0.6 at these locations to further increase the large horizontal shear. The current continues to move down the slope, with $h_{max}=2.4$ at $y = 1.05$ and 3.6 at $y = 3$.

In summary, the current preserves its potential vorticity south of the critical latitude mostly by moving westward to thin out while maintaining its slope parallel to that of the bottom and keeping the height of its western edge constant. Its width remains roughly constant at several times the radius of deformation and its velocity is largest near its center. The decreasing Coriolis parameter allows the transport to be conserved by increasing the velocity of the current as it thins even with a constant slope of the interface. At the critical latitude the boundary condition on the western edge of the current changes from vanishing velocity to vanishing thickness. This allows the western edge of the jet to fall and gain speed as it converts Bernoulli potential to kinetic energy. The relative vorticity of the current increases as it decreases width, moving eastward down the bottom slope. The interface flattens at the equator and current velocity becomes a maximum at the western boundary. North of the equator these trends continue, with the current interface dipping below the level of the resting interior as a result of the reverse in sign of the Coriolis parameter.

4.2.4 Discussion

An inertial solution for a potential vorticity and transport conserving jet riding a linear bottom slope on a β–plane has been constructed and solved using a scaling pertinent to the DWBC in the Somali Basin. The model is an extension of one developed earlier (Stommel and Arons, 1972), and benefits from insights resulting from work on the Somali Current (Anderson and Moore, 1979). The earlier work discusses one other class of jet not discussed here, that of a current denser than, and therefore isolated from the interior, a core of dense water moving northward along the bottom slope. While this case does not appear relevant to the Somali Basin, and has algebra more involved than that of the above study, it is of interest since one can imagine a DWBC composed of denser water than that in the interior. The limiting case of an isolated jet against a vertical western wall has been explored with a consistently applied equatorial β-plane (Nof, 1990). The isolated jet can not cross the equator, but has to turn east and move along the equator. This result derives from the fact that the jet is an isolated core of buoyant fluid on the western boundary, and presumably extends to an isolated core of dense fluid on a slope. Hence a jet of water denser than that found in the interior on a sloping bottom might be expected to turn eastward on the equator.

With the solution complete and described, its pertinence to the deep circulation of the Somali Basin is examined. First, unlike the jet described, DWBC's do not conserve transport along their length, as they feed the interior circulation. The model is presented to give some insight on an inertial jet in the vicinity of the equator, not to describe a DWBC fully.

South of the critical latitude the solution is well behaved and agrees well with observations in the area (Chapters 1 and 2). Maximum velocities range from 6 cm s^{-1} at 10°S to 15 cm s^{-1} at 3.5°S. Over this latitude range the jet thins from a thickness of 450 m to 150 m and widens from a width of 155 km to 184 km as it approaches the equator. Between the critical latitude and the equator the semi-geostrophic approximation may break down as mentioned above. The frictional term in 4.6

may also cause problems in this region. South of y_c the current thickness does not vanish, but for $y > y_c$ it does on the western edge. By 4.6 the frictional parameter v_x/h becomes infinitely large at the western edge in this region, and this term would significantly alter the potential vorticity of the jet if it were not neglected in the model. However, the solution is still reasonable in physical terms. At the equator the velocity is larger than observed, reaching 59 cm s^{-1} at the western edge of the jet, but the solution matches smoothly with that to the south, with a width of 96 km and a maximum thickness of 225 m at the equator.

North of the equator maximum velocities range from 85 cm s^{-1} at 3.5°N to 91 cm s^{-1} at 10°N. The maximum current thickness deepens from 360 m to 540 m and the width narrows from 40 km to 22 km over this latitude range. These results clearly do not agree with the observations (Chapter 2). In addition the frictional effect mentioned above continues to increases in magnitude with latitude as v_x increases and other questions emerge. Earlier results for a model similar to this one point to a non-unique solution north of the equator. In a model of the Somali current with a motionless lower layer and a wall for a western boundary, the transcendental equation for the transport of the upper layer has multiple roots; that is, more than one thickness of the current returns the assumed transport of the current (Anderson and Moore, 1979.) This oscillatory character is a result of the trigonometric nature of the solution north of the equator, and prompts a concern for the stability of the solution presented above north of the equator. The magnitudes of the solutions themselves are also dubious. The large velocities and narrow widths are not characteristic of any observed DWBC.

The fact that $h = 0$ and v_x is finite at the western edge of the jet north of $y = y_c$ indicates that if bottom friction were included here significant dissipation of potential vorticity would take place as the jet approached the equator. While desirable in terms of a realistic solution, the addition of even such a simple form of friction as shown on the RHS of 4.6 to the model would make it very difficult to determine the solution. However, examination of v_x/h required by the inviscid solution indicates that north of $y = 0$ this term becomes large and negative to

conserve potential vorticity in the face of an increasingly positive planetary vorticity. In fact, this term becomes large north of $y = y_c$, and by the equator $v_x/h = -1$ everywhere within the current by definition. Thus the relative vorticity is of the correct sign to dissipate the negative potential vorticity of the current and modify the potential vorticity of the jet from a negative value to a positive one. If r were large enough so that this term could make this change somewhere in the vicinity of the equator the values of relative vorticity would not have to grow as large as they do; thus the current velocities north of the equator would be lower, and the current wider. The problem of the trigonometric solutions would also be resolved, as the positive potential vorticity of the jet north of the equator would allow exponential solutions. In other words, the inclusion of bottom friction might allow the jet to cross the equator more realistically than the inviscid jet because it would allow modification of the negative potential vorticity of the jet.

4.3 Effects of Bathymetry in the Northeast Pacific Basin

The deep southward interior flow observed in the Northeast Pacific Basin is suspect in the Stommel Arons framework, because it implies downward vertical velocities in a flat-bottom ocean. However, the bottom in the Northeast Pacific Basin is not flat. There is a meridional rise in topography between the trough at the Clarion Fracture Zone (≈ 5500 m) and ridge near the equator (≈ 4300 m) which is greater than 1000 m over 15 degrees of latitude. The East Pacific Rise also supplies a zonal rise in topography to the east.

Where bottom slope is sufficiently large such that the vertical velocity generated at the bottom by the component of horizontal velocity running up the slope is larger than the upwelling velocity of the bottom water, topographic-β is large enough to overcome the effects of planetary-β and reverse the direction of interior flow of the flat-bottom Stommel-Arons framework such that it flows south and east. Instead of DWBC's to conserve mass and close the system, DEBC's (deep eastern boundary currents) result. (Look at Figure 1.1 in the mirror to get a qualitative feeling for

the circulation pattern imposed by such an effect.)

An estimate for the effect of bathymetry on the circulation can be obtained simply from 1.1 by assuming that the bathymetry in the basin has only a meridional slope. Integrating 1.1 over the thickness of the bottom water yields

$$(\beta h r - f\frac{\partial h}{\partial y})v_{bottom} = fw_{top},$$ (4.17)

where h is the layer depth, r is the ratio of the depth-averaged meridional velocity to the meridional velocity at the bottom, v_{bottom}, (a measure of bottom-intensification), $(\partial h)/(\partial y)$ is the meridional change in thickness of the bottom layer, (or the negative of the meridional bottom slope assuming the depth of the top of the bottom water does not change significantly in space) and w_{top} is the vertical velocity at the top of the bottom water. For topographic-β to be sufficient to reverse the meridional flow direction in the most favorable case of no upwelling (the RHS of 4.17 set to zero) the bottom slope must be sufficiently negative and the flow sufficiently bottom-intensified such that the second term on the LHS of 4.17 overcomes the first term on the LHS. As the equator is approached f decreases so for the flow to continue southward up a linear bottom slope r must increase, or the flow must become more bottom intensified.

In the Northeast Pacific Basin, the top of the bottom water is at 3600 m, and the bathymetry rises from 5500 m at 15°N in the Clarion Fracture Zone to 4300 m at the equator. With no upwelling at the top and a meridional velocity that increases linearly toward the bottom from zero at the top of the layer ($r = 0.5$) topographic-β will dominate to 10°N. In order for the flow to continue southward from that latitude the meridional flow would have to become further bottom-intensified.

However, the bottom slope is not simply meridional. If to a first approximation there were no upwelling at the top of the bottom water in the Northeast Pacific Basin and the flow were inviscid in the interior then potential vorticity Q would be conserved in the interior so that

$$Q = \frac{\beta y}{h},$$ (4.18)

where β is the change of the Coriolis parameter with latitude (2.25×10^{-11} m^{-1} s^{-1}

at 10°N), y is the distance from the equator and h the thickness of the layer of water.

In a flat-bottom ocean this means that water flows freely along constant latitude only, and only the divergence caused by upwelling in the interior or the friction found in the swift flows at the western boundary allows the flow to change latitude. However, in the Northeast Pacific Basin the bottom shoals to the equator and the east, and since the upper boundary of the LCPW (≈ 3500 m) lies below the crest of the East Pacific Rise (≈ 3000 m), potential vorticity asymptotes to zero at the equator and infinity at the 3500 m isobath along the ridge (Figure 4.5). Thus isopleths of potential vorticity fan out to the northwest from the intersection of the equator and the 3500 m isobath. In the absence of upwelling, water introduced anywhere to the northwest can flow southeastward along isopleths of potential vorticity toward this intersection point. With upwelling, the flow would cross these isopleths so as to tend northward of them, and would have a pattern within the basin qualitatively similar to that predicted by a flat-bottom Stommel-Arons framework, distorted to the extent that the potential vorticity isopleths do not run along latitude lines.

However, if the flow were bottom intensified such that the vertical velocity generated at the bottom exceeded that at the top, the water would cross the potential vorticity isopleths so as to tend southward of them. If this were the case, topographic-β would be dominant, and the interior flow would be to the southeast. With a source in the northwest at the Clarion Passage and a sink in the southwest just south of the Line Islands a DEBC running southward along the western flank of the East Pacific Rise would be fed from the source and exit the basin as a westward equatorial jet as observed.

The problem of the dynamics of bottom water flow in the Northeast Pacific Basin is far from solved here. The question of why there is a source at the Clarion Fracture Zone and a sink on the equator south of the Line Islands is not addressed. In fact, calculating the structure of the interior flow or the strength of the boundary currents and jets would not be trivial even given the source and sink strengths and locations. What has been shown here is that the bathymetry has sufficient slope to effect the
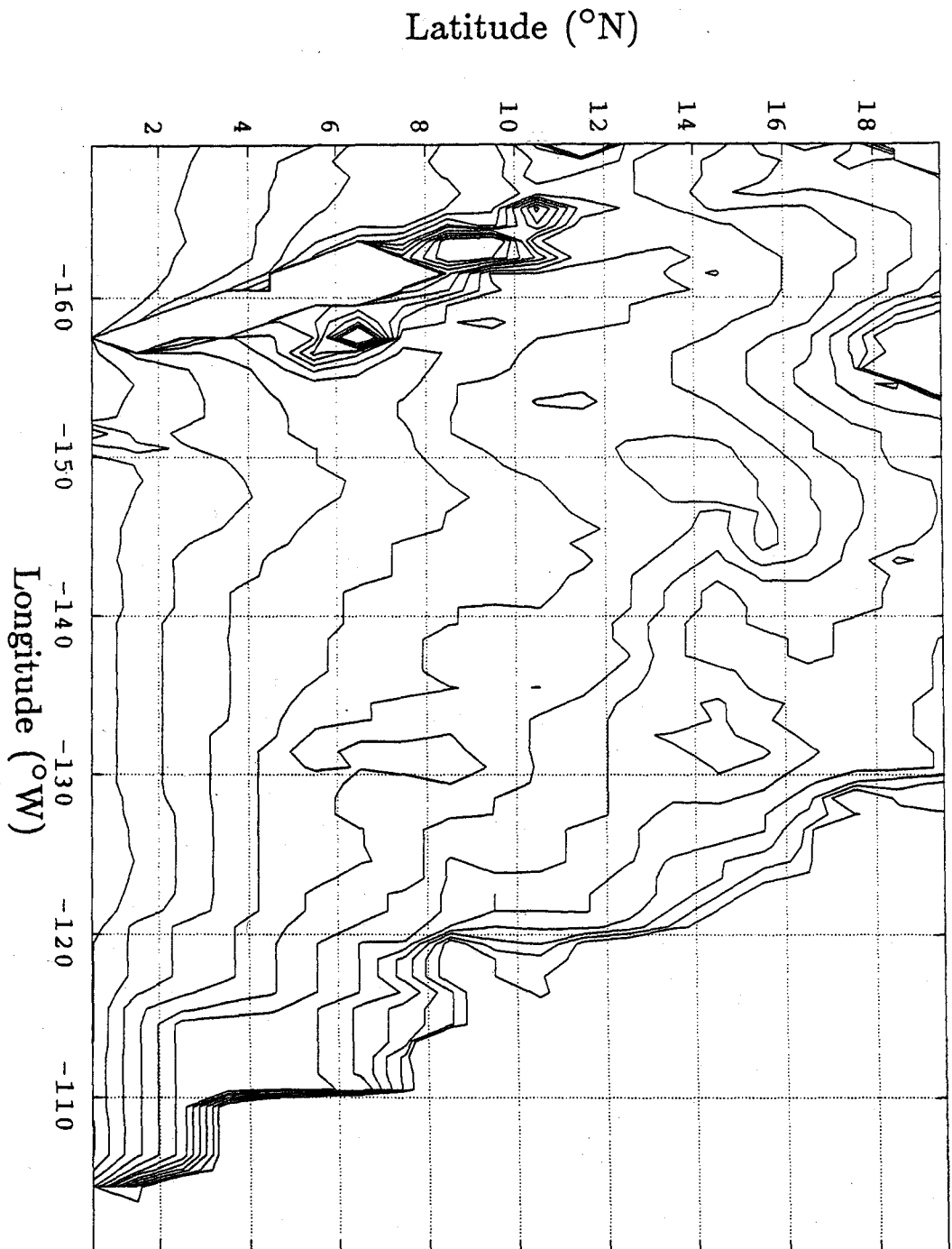
Figure 4.5: Isopleths of $(\beta\, y)/h$ for a layer of water in the Northeast Pacific basin with a lid at 3500 m depth. The isopleths tend to converge in the southeastern corner, where the equator and the East Pacific Rise meet.

Stommel-Arons solution in the interior and that with some bottom-intensification topographic-β could dominate, causing a DEBC fed from a jet running from the Clarion Passage to the East Pacific Rise to run southward along the East Pacific Rise to feed a westward zonal jet along the equator in the Northeast Pacific Basin.

4.4 Upwelling and Diffusivity Calculations

Deep mass budgets can be constructed in the equatorial regions of the Western Indian and Central Pacific Oceans. Estimates for the transport into the Somali Basin are available (Subsection 1.2.2). An estimate for the transport into the Central Pacific near 12° S has been made (Subsection 1.2.3) and that through 10° N is estimated above (Section 3.2). The areas of the basins at the ZVS's for LCPW entering these regions are known (Subsection 4.1.2 and 4.1.3). If the isotherms near the ZVS remain relatively flat, allowing the water entering to fill the basin, the transport divided by this area gives the mean vertical velocity w at the ZVS,

$$w = \frac{A}{\tau} ,$$ (4.19)

where w is the vertical velocity at the ZVS, A is the area of interest at the ZVS, and τ is the net transport into the area below the ZVS. While flat isotherms at the ZVS of the LCPW near and north of the equator are the rule in the Somali Basin and the Central Pacific, they are not in the Atlantic. Thus this exercise will not be performed in the Atlantic, where upwelling rates and vertical diffusivities are estimated elsewhere (Hogg et al., 1982; Whitehead, 1989).

Simple heat budgets for the bottom water in the deep basins allow estimation of the vertical diffusivities. The sources of heat are assumed to be a uniform geothermal heating up from the bottom and vertical diffusion of heat down from the deep water above. The heat content of the bottom water is assumed to remain constant through the introduction of bottom water into the deep basins through passages. The equation for the heat balance is written as

$$\rho c_p \left(\tau_{in}\theta_{in} - \tau_{out}\theta_{out} - \tau_{top}\theta_{top} \right) + AG = -A\rho c_p \kappa \frac{\partial \theta}{\partial z} ,$$ (4.20)

where $\rho c_p = 4\times10^6$ J m^{-3} $^\circ$C^{-1} is the specific heat of sea water per unit volume, G the basin-averaged rate of geothermal heating, κ the vertical diffusivity and $\partial\theta/\partial z$ the vertical gradient of potential temperature evaluated at the top of the bottom water. The various τ terms are the transports into the area A in the horizontal, τ_{in}, out of the area in the horizontal, τ_{out}, and the residual out of the area through the top, τ_{top}. The potential temperature terms that multiply these are the transport weighted mean potential temperatures of these waters. The LHS gives the net heating by water entering and exiting the area in the horizontal, water exiting the area in the vertical, and geothermal heating through the sea floor. The RHS represents the heat transferred by vertical diffusion of potential temperature.

4.4.1   The Western Indian Ocean

In the western Indian Ocean, differences in estimates of transport in and out of the Mascarene and Madagascar Basins are too small to allow calculations there (Subsection 1.2.2), and the transport of deep water entering the Arabian Basin is not well known (Subsection 2.3.4). However, the Somali Basin is an excellent place to perform these calculations, since the only horizontal source of bottom water is through the Amirante Passage and there is no horizontal sink. The temperature and vertical gradient of temperature at the top of the bottom water is fairly uniform. The following is a refinement of previous calculations (Fieux and Swallow, 1988; Barton and Hill, 1989). G=51.8$\pm$10.0 mW m^{-2} (from Fieux and Swallow (1989)). The area of the basin at the 3800 m isobath is estimated from historical bathymetric data with 1° resolution at A=3.37$\pm$.3x10^6 km^2. The transport in is $\tau_{in} = 4.0 \pm$ 1.0x10^6 m^3 s^{-1}, and the potential temperature in is $\theta_{in} = 0.9^\circ$C (these last two quantities are calculated from stations 1-6 from Barton and Hill, (1989)). Since $\tau_{out} = 0$, $\tau_{top} = \tau_{in}$. From the CTD data from CD 86-19 and CD 87-25 $\partial\theta/\partial z =$ 4.29 ± 0.23x10^{-4} $^\circ$C m^{-1} and $\theta_{top} = 1.219 \pm 0.005^\circ$C.

From these numbers the vertical velocity through 3800 m ($\theta \approx 1.2^\circ$C) in the Somali Basin is estimated at w=12x10^{-5} cm s^{-1} with a worst case range of 8.2–

$16\text{x}10^{-5}$ cm s^{-1}. The vertical diffusivity here is $\kappa = 8.6$ cm^2 s^{-1} with a worst case range of 5.3–13 cm^2 s^{-1}. The geothermal heating term G makes only a small contribution to 4.20, reducing the vertical diffusivity by less than 0.05 of the value it would have been in the absence of this term. Another way of thinking about vertical velocity and diffusivity is a residence time, defined as the volume of the basin below the ZVS divided by the volume transport into the basin. This is approximately the time scale over which water entering the basin must heat up sufficiently to rise above the ZVS. The volume of the Somali Basin below 3800 m is estimated at $0.25\text{x}10^{16}$ m^3 from the 1° resolution historical bathymetry. Thus the residence time for bottom water in the Somali Basin is order 20 years.

4.4.2   The Central Pacific Ocean

The calculation can also be performed between 12°S and 10°N in the central basins of the Pacific, since the ZVS does not vary significantly between these latitudes and the potential temperature at that ZVS does not change much in depth north of 12°S. However, the vertical gradient of potential temperature at the ZVS does vary significantly in the region, so the estimate will have more error than that for the Somali Basin if the upwelling is not uniform as assumed. Once again $G = 50 \pm 10$ mW m^{-2} (Lee, 1970). The area of the central basins between 12°S and 10°N at the top of the LCPW (≈ 3600 db) is $2.4\pm0.2\text{x}10^7$ km^2. To the south $\tau_{in} = 12.7 \pm 3.2\text{x}10^6$ m^3 s^{-1} and $\theta_{in} = 0.81$°C [calculated from the CTD stations used by Taft et al. (1990) using their choice of ZVS.] To the north $\tau_{out} = 8.4 \pm 2.1\text{x}10^6$ m^3 s^{-1} and $\theta_{out} = 1.03$°C (estimated using the ZVS's from Section 3.2 for the 10°N transpacific section.) Thus $\tau_{top} = \tau_{in} - \tau_{out} = 4.3\pm5.3\text{x}10^6$ m^3 s^{-1}. The average potential temperature at the top of the LCPW is $\theta_{top} = 1.22$°C (≈ 3600 db) and $\partial\theta/\partial z = 3.7 \pm 0.2\text{x}10^{-4}$ °C m^{-1} at this level using the average of the values from stations at 12°S and 10°N.

From these estimates the area average vertical velocity through the top to the LCPW is $w = 1.8\text{x}10^{-5}$ cm s^{-1} with a worst case range of -0.45–4.4x10^{-5} cm s^{-1}.

The vertical diffusivity is $\kappa = 3.8\,\mathrm{cm}^2\,\mathrm{s}^{-1}$ with a range of $1.5–6.7\,\mathrm{cm}^2\,\mathrm{s}^{-1}$. Once again, the geothermal heating plays a small role in the balance, reducing the vertical diffusivity by less than 0.10 of the value it would be without this term. In this area between 12°S and 10°N the volume of the central basins below the ZVS at 3600 m is estimated at $2.4\mathrm{x}10^{16}\,\mathrm{m}^3$, or about 10 times that of the Somali Basin. The net horizontal inflow to the area is about the same, so the resulting residence time of 200 years is about an order of magnitude longer than that estimated for the Somali Basin. All these calculations of vertical velocity, vertical diffusivity and residence time indicate that bottom water renewal is much slower in the equatorial Pacific Ocean than in the equatorial Indian Ocean.

As noted above (Section 3.2), the numbers for transport at 10°N in the East Mariana Basin are questionable, and differ significantly from those just upstream using U.S.-P.R.C. TOGA CTD data collected at 165°E from 5°S to 10°N. Until the transport of LCPW through the East Mariana Basin is better determined estimates for the near-equatorial vertical velocities and diffusivities in the bottom water of the Pacific will be somewhat uncertain. However, if the results from the analysis of the U.S.-P.R.C. TOGA sections at 165°E are used to determine the transport of LCPW through the East Mariana Basin (see Section 3.2) the amount of water estimated to be moving northward through the East Mariana Basin at 10°N is increased such that as much or even possibly more bottom water exits the area at 10°N as enters at 12°S. It is not feasible for more bottom water to exit the area than enters without unlikely downwelling, so a lower limit for the vertical velocity is effectively zero. However, the bottom water moving out of the area is still warmer than that which entered, so with no vertical velocity the best estimate of vertical diffusivity is cut down to $\kappa = 2.8\,\mathrm{cm}^2\,\mathrm{s}^{-1}$. These estimates for the vertical diffusivity of the bottom water in the central tropical Pacific are only slightly larger than Munk's (1966) estimate for the abyssal North Pacific Ocean.

Chapter 5

Discussion of Theory and Observation

Above, the theory of deep circulation is reviewed along with observations of deep circulation in the western Atlantic, western Indian, and central Pacific Oceans (Chapter 1). The circulation of the deep and bottom water of the Somali Basin and the circulation of the bottom water of the Arabian Basin are described using two recent CTD surveys in the area and previously published results (Chapter 2). In the central Pacific basins the circulation of LCPW and NPDW near the equator is described using a CTD section at 10°N and recently published analysis of observations (Chapter 3). Theory to complement the observations is presented, including a Stommel-Arons framework for the deep circulation modified to use realistic basin boundaries for both oceans, a modification of an inertial DWBC model for the Somali Basin observations, a development of the effect of topography on the circulation of bottom water for the Pacific Ocean observations and upwelling and vertical diffusivity estimates made for the bottom water of both oceans (Chapter 4). Here the observations are cast in light of the theory and the questions resulting from differences among theory and observation are raised.

5.1   The Bottom Water of the Somali Basin

The bottom water of the Somali Basin, $4\pm1\mathrm{x}10^6$ m^3 s^{-1}, enters from the Mascarene Basin through the Amirante Passage below a ZVS of 3800 db ($\theta \approx 1.2°$C) (Barton and Hill, 1989). Here CTD surveys were performed during subsequent northeast and southwest monsoons. These two surveys show similar patterns in the

111

bottom water. The sections near 3°S show a northward flowing DWBC with an average estimated transport of 3.9x10^6 m^3 s^{-1} below a ZVS of $\theta = 1.2°$C, similar to that used to the south in the Amirante Passage. The sections crossing the equator show a northeastward velocity, symmetric and trapped to within $\pm 3/4°$ of the equator, which increases toward the bottom below a similar ZVS. These features suggest that the flow is eastward and not northward. The northern sections reveal a large mass of colder water offshore, east of the Chain Ridge. The bottom water near the coast, west of the Chain Ridge, has the lowest dissolved-oxygen concentrations for $\theta \le 1.2°$C observed in the Somali Basin.

A simple Stommel-Arons framework for the deep circulation using a realistic 3800 m isobath as the basin boundary and introducing the source at the Amirante Passage results in a northward flowing DWBC which steadily loses water to the interior from 8.5°S to 4°N. North of 4°N the DWBC flows southward, fed by the poleward interior flow which re-encounters the western boundary. The model is roughly consistent with the observational result of the northward flow in the south, and, in the northern part of the basin, with the presence of the water of most recent southern origin in the interior. However, the suggestion of the eastward turn in the DWBC at the equator in the observations is a very different result from the northward flow along the western boundary predicted by the model.

However, mass and heat budgets assuming the inflow through the Amirante Passage all escapes vertically through the horizontal area bounded by the 3800 m isobath within the basin yield a basin-averaged vertical velocity of 12±4x10^{-5} cm s^{-1} and a vertical diffusivity of 9±4 cm^2 s^{-1}. These results are considerably higher than other estimates in the Atlantic (Hogg et al., 1982; Whitehead, 1989) or an earlier estimate in the Pacific (Munk, 1966). The upwelling rate is also higher than that of the whole of the Indian Ocean at 2000 m, estimated at 4x10^{-5} cm s^{-1} (Warren, 1981b). The large basin-averaged vertical velocities in the Somali Basin may be related to the eastward turning of the DWBC at the equator, since a concentration of upwelling along the equator will cause the eastward interior flow of the Stommel-Arons framework to concentrate there (Kawase, 1987). Recent numerical studies

112

also show that increased vertical diffusivities are correlated with increased strength of eastward jets of bottom water (Suginohara and Fukasawa, 1988). While the physics underlying this behavior is still obscure, and even controversial (Weaver and Sarachik, 1990), the tight symmetrical trapping of the deep velocity field to the equator, coupled with the high estimates of vertical diffusivity, suggest that the DWBC may indeed turn eastward in a jet at the equator, rather than feeding the interior as indicated by the Stommel-Arons model.

The presence of isobaths parallel to the gentle continental rise in the southern sections suggested the reformulation of an inertial model of a DWBC on a slope (Stommel and Arons, 1972) for the equatorial β–plane to explore such a current in the vicinity of the equator. As long as the decreasing Coriolis parameter can be compensated for by a decrease in the thickness of the jet to keep the potential vorticity of the jet constant, the velocity and relative vorticity of the jet do not become large. However, at a critical latitude just south of the equator, the relative vorticity necessary to keep the potential vorticity negative requires unrealistically large velocities and horizontal shears (changes of about 100 cm s^{-1} over 30 km with 10° of the equator). Either potential vorticity must be dissipated (possibly by bottom friction) or the current will either not cross the equator or become unstable upon entering the northern hemisphere.

At any rate the flow in the bottom water of the Somali Basin does not appear to be influenced by the annual monsoon season in these two data sets, taken during the northeast monsoon of 1986–1987 and the southwest monsoon of 1987. This is in contrast to the circulation of the deep water north of the equator inferred from CTD data taken in April 1985 and 1986 and at the equator inferred from current meter data taken from October 1985 to October 1986 (Schott et al., 1989). It appears from these data sets that the monsoon influence extends to the deep water but not the bottom water. However, the southwest monsoon of 1987 was very weak (Krishnamurti et al., 1989), and it is still possible that the DWBC in the bottom water observed south of the equator extends north of the equator during strong southwest monsoons, such as that of 1964, when observations suggested a

northward flowing DWBC in the bottom water north of the equator (Warren et al., 1966).

5.2 The Deep Water of the Somali and Arabian Basins

The Somali Basin deep water is suggested to be supplied from a branch of the DWBC which runs northward along the Central Indian Ridge and upwelling of bottom water which enters the basin through the Amirante Passage. The DWBC branch turns northeastward to run along the Mascarene Plateau and then runs eastward into the southern interior of the Somali Basin. Some evidence is seen for northward flow near the coast in the northern sections near the level of the sill depth of the Owen Fracture Zone to the north. No explanation for the presence of different sources for the bottom and deep waters of the Somali Basin is attempted. Since the circulation of the deep water in the Somali Basin is only hinted at in the data it is not modeled here.

The DWBC in the Arabian Basin is shown to flow southeastward along the flank of the Carlsberg Ridge. This direction of the DWBC in the Arabian basin is in accord with a simple Stommel-Arons model with a source at the Owen Fracture Zone, supplied by deep water in the Somali Basin. If the source is placed at the other possible inflow, a gap in the Chagos-Laccadive Ridge near 3.5°S, the DWBC in the model flows to the northwest where the sections are located, in the opposite direction from that observed. Thus the bottom water of the Arabian Basin appears to be supplied by the deep water of the Somali Basin through the Owen Fracture Zone.

5.3 The Circulation of LCPW in the Equatorial Pacific

In the equatorial Pacific, the topography is more complicated than that found in the Somali Basin. The single DWBC moveing northward at 12°S (Taft et al., 1990), is observed to have split into two DWBC's by 10°N, each flowing northward

against a ridge at the western side of a basin. The western branch, flowing along the Caroline Islands in the East Mariana Basin, apparently continues northward. Some of the eastern branch, flowing northward along the Marshall Islands in the Central Pacific Basin, seems to be deflected eastward by the Hawaiian Ridge to run along the Clarion Fracture Zone, where it flows back south toward the equator in a broad interior flow in the Northeast Pacific Basin, east of the Line Islands. Upon reaching the equator the water appears to turn westward in a zonal jet, visible from 138°W to 148°W in the PEQUOD White Horse velocity profiles (Ponte and Luyten, 1989) until it reaches the Line Islands, where it is deflected to the south by the Line Islands and observed re-entering the Central Pacific Basin in velocity profiles at 2.5°S, 159°W (Firing, 1989), whence it most likely recirculates northward again as part of the DWBC, rejoining the water moving north from 12°S.

The most curious features of this circulation are the southward interior flow and equatorial westward jet in the Northeast Pacific Basin. The LCPW apparently can run southeastward without downwelling at its top in the Northeast Pacific Basin because of the large southeastward rise in topography from the Clarion Fracture Zone toward a small ridge near the equator to the south and the East Pacific Rise to the east. A southeastward flow running up this slope preserves its potential vorticity by thinning without significant changes in its interface height. Upon reaching the equator this interior flow apparently forms a westward flowing equatorial jet, again perhaps due to bathymetry, which may overcome the effect of planetary-β and allow and eastern boundary current to flow south along the East Pacific Rise to feed this westward jet. Because of the geometry and bathymetry of the basin this jet runs westward to join the DWBC and does not originate from it and run eastward as may occur in the Somali Basin.

The net flow of LCPW at 10°N is smaller than that at 12°S but still northward, as indicated by the Stommel-Arons dynamics. The area average vertical rate of upwelling near 3600 m between 12°S and 10°N is $2 \pm 2 \times 10^{-5}$ cm s^{-1}, much closer to the often quoted estimate of 1.4×10^{-5} cm s^{-1} for the North Pacific (Munk, 1966) than the estimate for the bottom water of the Somali Basin, and the area average

estimate of vertical diffusivity is only a bit high at 4 ± 3 cm^2 s^{-1} compared to Munk's 1.3 cm^2 s^{-1}. It appears that the vertical velocity and diffusivity at the top of the bottom water of the Somali Basin at similar latitudes in the Indian Ocean are much higher than those estimated at the top of the bottom water in the tropical Pacific.

5.4   Conclusions

While the circulation of bottom water away from the equator is broadly consistent with Stommel-Arons dynamics in both the tropical Indian and Pacific Oceans, the data in the Somali Basin suggests that an eastward flowing equatorial deep jet is being fed by the DWBC from the south, and the data in the Pacific show a westward flowing equatorial deep jet which appears to be fed from the north by a southward interior flow influenced by the topography. In the Somali Basin the vertical velocity and diffusivity at the top of the bottom water are estimated to be greater than previous estimates by several fold, but this result does not seem to hold in the Pacific Ocean. These results are in accord with model results, which show DWBC's turning east at the equator when vertical velocity is concentrated about the equator and when vertical diffusivity is large. A model of an inertial DWBC shows that it cannot conserve potential vorticity and continue realistically or stably into the northern hemisphere after crossing the equator. The suggestion of eastward flow at the equator in the bottom water of the Somali Basin argues that this analytical result is in part correct. While the DWBC flowing north in the South Pacific is observed to have crossed the equator and reached 10°N, albeit split into two by the topography, it is partially fed by a recirculation from the north, which presumably helps to eliminate the negative potential vorticity of water entering the region from the south by mixing it with water from the equator and northward. The rough topography in the central Pacific basins may also aid in dissipating potential vorticity. The problem of equatorial dynamics of the DWBC's deserves more study.

REFERENCES

Anderson, D. L. T. and D. W. Moore (1979) Cross-equatorial inertial jets with special relevance to very remote forcing of the Somali Current. *Deep-Sea Research*, **26**, 1–22.

Barton, E. D. and A. E. Hill (1989) Abyssal flow through the Amirante Trench (Western Indian Ocean). *Deep-Sea Research*, **36**, 1121–1126.

Bryden, H. L., D. H. Roemmich and J. A. Church (1990) Ocean heat transport across 24°N in the Pacific. *Deep-Sea Research*, In Press.

Craig, H. (1990) The HELIOS helium 3 section: Implications for the deep water circulation in the North and South Pacific. *EOS, Transactions of the American Geophysical Union*, **71**, 882.

Craig, H., W. S. Broeker and D. Spencer (1981) *GEOSECS Pacific Expedition, Volume 4, Sections and Profiles*. National Science Foundation, Washington, D. C., 251 pp.

Edmond, J. M., Y. Chung and J. G. Sclater (1971) Pacific Bottom Water: Penetration east around Hawaii. *Journal of Geophysical Research*, **76**, 8089–8097.

Edmond, J. M., S. S. Jacobs, A. L. Gordon, A. W. Mantyla and R. F. Weiss (1979) Water column anomalies in dissolved silica over opaline sediments and the origin of the deep silica maximum. *Journal of Geophysical Research*, **84**, 7809–7826.

Eriksen, C. C. (1981) Deep currents and their interpretation as equatorial waves in the western Pacific Ocean. *Journal of Physical Oceanography*, **11**, 48–70.

Eriksen, C. C. (1982) Geostrophic equatorial deep currents. *Journal of Marine Research*, **40** (Suppl.), 143–157.

Fieux, M., F. Schott and J. C. Swallow (1986) Deep boundary currents in the western Indian Ocean revisited. *Deep-Sea Research*, **33**, 415–426.

Fieux, M. and J. C. Swallow (1988) Flow of deep water into the Somali Basin. *Deep-Sea Research*, **35**, 303–309.

Firing, E. (1989) Mean zonal currents below 1500 m near the equator, 159 W. *Journal of Geophysical Research*, **94**, 2023–2028.

GEBCO Charts (1984) General bathymetric chart of the oceans. Published by Canadian Hydrographic Service, Ottowa, Canada, under authority of IHO and IOC (UNESCO), 5th edition.

Hogg, N., P. Biscaye, W. Gardner and W. J. Schmitz, Jr. (1982) On the transport and modification of Antarctic Bottom Water in the Vema Channel. *Journal of Marine Research*, **40** (Suppl.), 231–263.

Johnson, D. A. and J. E. Damuth (1979) Deep thermohaline flow and current-controlled sedimentation in the Amirante Passage: Western Indian Ocean. *Marine Geology*, **33**, 1–44.

Joyce, T. M., B. A. Warren and L. D. Talley (1986) The geothermal heating of the abyssal subarctic Pacific Ocean. *Deep-Sea Research*, **33**, 1003–1015.

Kawase, M. (1987) Establishment of deep ocean circulation driven by deep-water formation. *Journal of Physical Oceanography*, **17**, 2294–2317.

Kearns, E. J., S. R. Emmerson, D. B. Olson, G. Johnson and J. Morrison (1989) *CTD and Bottle Data from RRS Charles Darwin MASAI 86–87*. Data Report, Rosenstiel School of Marine and Atmospheric Science, University of Miami and Woods Hole Oceanographic Institution. Unpublished Manuscript.

Kenyon, K. E. (1983) Sections at 35°N in the Pacific. *Deep-Sea Research*, **30**, 349–369.

Knapp, G. P. and M. C. Stalcup (1987) Progress in the measurement of salinity and oxygen at the Woods Hole Oceanographic Institution. WHOI–87–4, Woods Hole Oceanographic Institution. Unpublished technical report. 27 pp.

Krishnamurti, T. N., H. S. Bedi and M Subramaniam (1989) The Summer Monsoon of 1987. *Journal of Climate*, **2**, 321–340.

Lee, W. H. K. (1970) On the global variations of terrestrial heat-flow. *Phys. Earth Planet. Interiors*, **2**, 332-341.

Lukas, R. and E. Firing (1984) The geostrophic balance of the Pacific Equatorial Undercurrent. *Deep-Sea Research*, **31**, 61–66.

Mantyla, A. W. and J. L. Reid (1983) Abyssal characteristics of the World Ocean waters. *Deep-Sea Research*, **30**, 805–833.

Nof D. (1990) Why are some boundary currents blocked by the equator? *Deep-Sea Research*, **37**, 853–873.

Ponte, R. M. (1988) Observations and Modelling of Deep Equatorial Currents in the Central Pacific. MIT/WHOI, WHOI–88–9.

Ponte, R. M. and J. Luyten (1989) Analysis and interpretation of deep equatorial currents in the central Pacific. *Journal of Physical Oceanography*, **19**, 1025–1038.

Ponte, R. M. and J. Luyten (1990) Deep velocity measurements in the western equatorial Indian Ocean. *Journal of Physical Oceanography*, **20**, 44–52.

Ponte, R. M., J. Luyten and P. L. Richardson (1990) Equatorial deep jets in the Atlantic Ocean. *Deep-Sea Research*, **37**, 711–713.

Quadfasel, D. R. (1980) *A Compilation of current and temperature data from moored instruments during INDEX 1979, R.R.S. Discovery.* Data Report 19, Institute of Oceanographic Sciences, Wormley, Godalming, Surrey. Unpublished Manuscript., 17 pp.

Reid, J. L. (1986) On the total geostrophic circulation of the South Pacific Ocean: Flow patterns, tracers, and transports. *Progress in Oceanography*, **16**, 1–62.

Reid, J. L. and P. F. Lonsdale (1974) On the flow of water through the Samoan Passage. *Journal of Physical Oceanography*, **4**, 58–73.

Schmitz, W. J. and P. L. Richardson (1990) On the sources of the Florida Current. *Deep-Sea Research*, In press.

Schott, F., J. C. Swallow and M. Fieux (1989) Deep currents underneath the equatorial Somali Current. *Deep-Sea Research*, **36**, 1191–1199.

Spencer, D., W. S. Broecker, H. Craig and R. F. Weiss (1982) *GEOSECS Indian Ocean Expedition, Volume 6, Sections and Profiles.* National Science Foundation, Washington, D. C., 140 pp.

Stommel, H. (1948) The westward intensification of wind-driven ocean currents. *Transactions of the American Geophysical Union* **29**, 202–206.

Stommel, H. and A. B. Arons (1960a) On the abyssal circulation of the world ocean-I. Stationary planetary flow patterns on a sphere. *Deep-Sea Research*, **6**, 140–154.

Stommel, H. and A. B. Arons (1960b) On the abyssal circulation of the world ocean-II. An idealized model of the circulation pattern and amplitude in oceanic basins. *Deep-Sea Research*, **6**, 217–233.

Stommel, H. and A. B. Arons (1972) On the abyssal circulation of the world ocean-V. The influence of bottom slope on the broadening of inertial boundary currents. *Deep-Sea Research*, **19**, 707–718.

Stommel, H., A. B. Arons and A. J. Faller (1958) Some examples of stationary planetary flow patterns in bounded basins. *Tellus*, **10**, 179–187.

Suginohara, N. and M. Fukasawa (1988) Set-up of deep circulation in multi-level numerical models. *Journal of the Oceanographical Society of Japan*, **44**, 315–336.

Sverdrup, H. U., M. W. Johnson and R. H. Flemming (1942) *The Oceans: Their Physics, Chemistry, and General Biology.* Prentice Hall, Inc. Englewood Cliffs, New Jersey., 1087 pp.

Swallow, J. C. and R. T. Pollard (1988) Flow of bottom water through the Madagascar Basin. *Deep-Sea Research*, **35**, 303–309.

Taft, B. A., S. P. Hayes, G. E. Frederich and L. A. Codispoti (1990) Flow of Abyssal Water into the Samoa Passage. *Deep-Sea Research*, In Press.

Warren, B. A. (1973) Transpacific hydrographic sections at Lats. 43 S and 28 S: The SCORPIO Expedition-II. Deep water. *Deep-Sea Research*, **20**, 9–38.

Warren, B. A. (1974) Deep flow in the Madagascar and Mascarene Basins. *Deep-Sea Research*, **21**, 1–21.

Warren, B. A. (1977) Deep western boundary current in the eastern Indian Ocean. *Science*, **196**, 53–54.

Warren, B. A. (1978) Bottom water transport through the Southwest Indian Ridge. *Deep-Sea Research*, **25**, 315–321.

Warren, B. A. (1981a) Deep circulation of the World Ocean. In *Evolution of Physical Oceanography, Scientific Surveys in Honor of Henry Stommel*, B. A. Warren and C. Wunsch, editors. The MIT Press, Cambridge, Massachusetts, pp. 6–41.

Warren, B. A. (1981b) Transindian hydrographic section at lat. 18°S: Property distributions and circulation in the South Indian Ocean. *Deep-Sea Research*, **28**, 759–788.

Warren B. A. (1982) The deep water of the Central Indian Basin. *Journal of Marine Research*, **40** (Suppl.), 823–860.

Warren, B. A. and W. B. Owens (1988) Deep currents in the central subarctic Pacific Ocean. *Journal of Physical Oceanography*, **18**, 529–551.

Warren, B., H. Stommel and J. C. Swallow (1966) Water masses and patterns of flow in the Somali Basin during the southwest monsoon of 1964. *Deep-Sea Research*, **13**, 825–860.

Warren, B. A. and A. D. Voorhis (1970) Velocity measurements in the deep western boundary current of the South Pacific. *Nature*, **228**, 849–850.

Weatherly, G. L. and E. A. Kelley (1985) Two views of the cold filament. *Journal of Physical Oceanography*, **15**, 68–81.

Weatherly, G. L. and P. J. Martin (1978) On the structure and dynamics of the oceanic bottom boundary layer. *Journal of Physical Oceanography*, **8**, 557–570.

Weaver, A. J. and E. S. Sarachik (1990) On the importance of vertical resolution in certain ocean circulation models. *Journal of Physical Oceanography*, **20**, 600–609.

Weiss, R. F., J. L. Bullister, R. H. Gammon and M. J. Warner (1985) Atmospheric chlorofluoromethanes in the deep equatorial Atlantic. *Nature*, **314**, 608–610.

Whitehead, J. A. (1989) Surges of Antarctic Bottom Water into the North Atlantic. *Journal of Physical Oceanography*, **19**, 853–861.

Wright, R. (1969) Deep Water movement in the Western Atlantic as determined by the use of a box model. *Deep-Sea Research*, **16** (Suppl.), 433–446.

Wright, W. R. (1970) Northward transport of Antarctic Bottom Water in the western Atlantic Ocean. *Deep-Sea Research*, **17**, 367–371.

Wüst, G. (1935) Schichtung und Zirkulation des Atlantischen Ozeans. Die Stratosphäre. In *Wissenschaftliche Ergebnisse der Deutschen Atlantischen Expedition auf dem Forschungs-und Vermessungsschiff "Meteor" 1925–1927* 6: 1st Part, 2, 180 pp. (*Stratosphere of the Atlantic Ocean* W. J. Emery ed. (1978) Amerind, New Dehli, 112 pp.)

Wüst, G. (1957) Quantitative untersuchungen zur statik und dynamik des Atlantischen Ozeans, Stromgeschwindgkeiten und strommengen in den tiefen des Atlantischen Ozeans unter besonderer berücksichtigung des tiefenund bodenwassers. *Wissenschaftliche Ergebnisse der Deutschen Atlantischen Expedition auf dem Forschungs-und Vermessungsschiff "Meteor" 1925–1927*, VI, Tiel 2, 261–420.

Wyrtki, K (1971) *Oceanographic Atlas of the International Indian Ocean Expedition*. National Science Foundation, Washington, D.C., 531 pp.

Hand contoured section profiles for four variables are presented using depth and distance along the station track for the deep sections from the *R.R.S. Charles Darwin* cruises CD 86–19 and CD 87–25. (See Figure 2.2 for station locations). The vertical scale is exaggerated by a factor of 200 with respect to the horizontal. A short section taken during CD 86–19 off the coast of Somalia is omitted as it was not repeated during CD 87–25 and does not add significantly to the discussion.

All isopleths were found after applying a 10 db (5 points in the 2 db data) boxcar filter to temperature, T, and salinity, S. The contoured variables are potential temperature, θ (in °C), salinity, S (in practical salinity units or psu), dissolved oxygen concentration, O_2 (in $ml\ l^{-1}$) and variably referenced potential density anomaly, stacked-σ (in anomaly units of kg m^{-3}).

The first three variables are self-explanatory. Stacked-σ here refers to the potential density (in g cm^{-3}) with 1 g cm^{-3} subtracted and the result multiplied by 1000 to get anomaly units of kg m^{-3}. The potential density is referenced to the surface for the interval between the surface and roughly 1000 db, 2000 db for the interval between roughly 1000 and 3000 db, and 4000 db for the interval between roughly 3000 db and the bottom. The numerical subscript to σ refers to this reference level in thousands of db. Here the most dense value of σ_0 contoured is 27.4, the lightest and most dense values of σ_2 used are 36.4 and 37.01, and the lightest σ_4 value is 45.83. These limits were chosen to cover the water column, keeping the references roughly within the pressure limits given and maintaining continuity from section profile to section profile. This method of contouring potential density accounts roughly for the variability of the expansion coefficients of temperature and salinity with pressure in density while preserving continuity of isopleths.

Contouring is highly subjective, and in many cases alternative contouring may suggest itself to the reader. Features are connected from station to station whenever possible, perhaps beyond reason in some cases. All isopleths which survive the 10 db boxcar filter are contoured. Contour intervals often are changed in the vertical to accentuate changes in the deep water. Generally the heavy solid lines indicate the largest contour intervals, followed by the light solid lines, with the dashed lines indicating the finest contouring.

The crosses in the water column directly under the station markers indicate the depth to which the CTD data extends for each station. The dots in two of the salinity section profiles of CD 87–25 indicate where bottle data was used to contour salinity after the conductivity cell failed. Below T=3°C the linear T–S relation is used (Section 2.1). Stacked-σ is not contoured above T=3°C in the absence of CTD conductivity data because the bottle data is too coarse to contribute any significant information about the density field. The θ and O_2 fields are contoured as they are not significantly effected by the loss of the conductivity cell.

The section profiles from CD 86–19, taken during the northeast monsoon in December 1986 and January 1987 precede those from CD 87–25, taken during the southwest monsoon in July and August 1987. Section profiles of the four variables

are presented in order θ, S, O_2 and stacked-σ for each of the four sections; the southern section from 4°S 40°E to 2°S 50°E, the equatorial section from 2.5°N 46.5°E to 2°S 50°E, the northern section from 8°N 50.5°E to 2°N 57.5°E, and the Carlsberg Ridge section from 10°N 64°E to 2°N 57.5°E (Figure 2.2).

Figure A.1: Section profile of potential temperature θ (degrees C) for the southern section of CD 86-19.
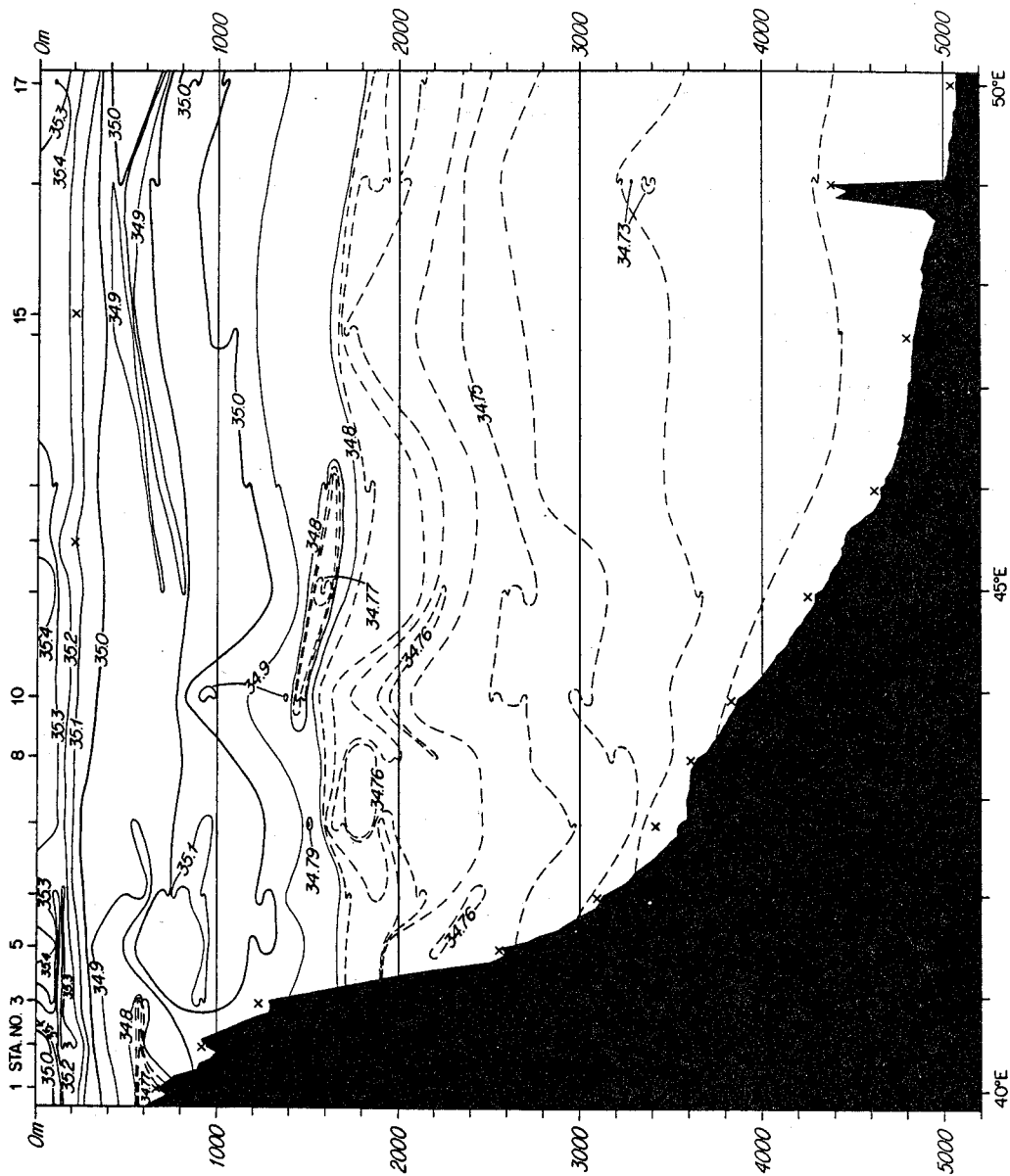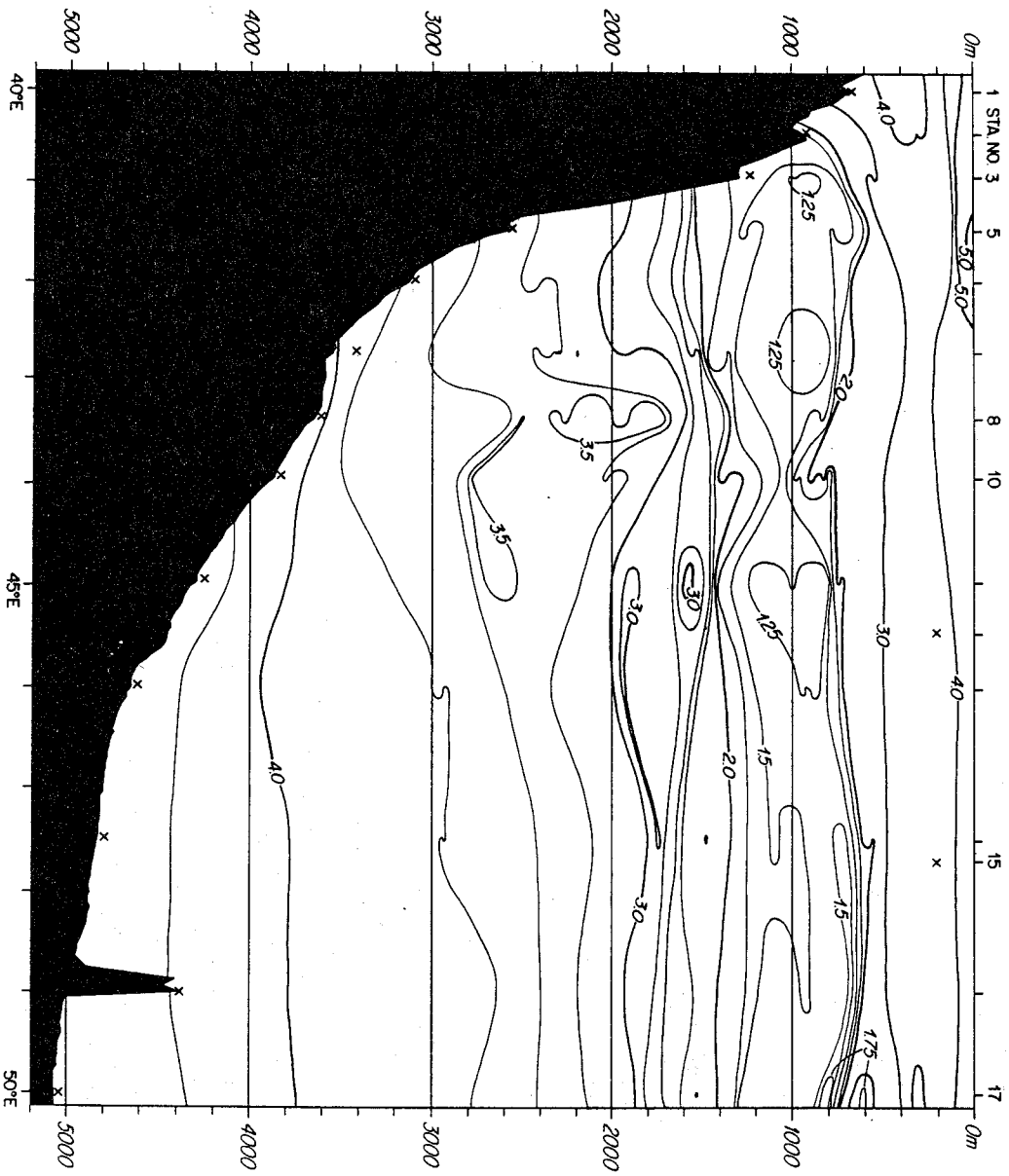
126
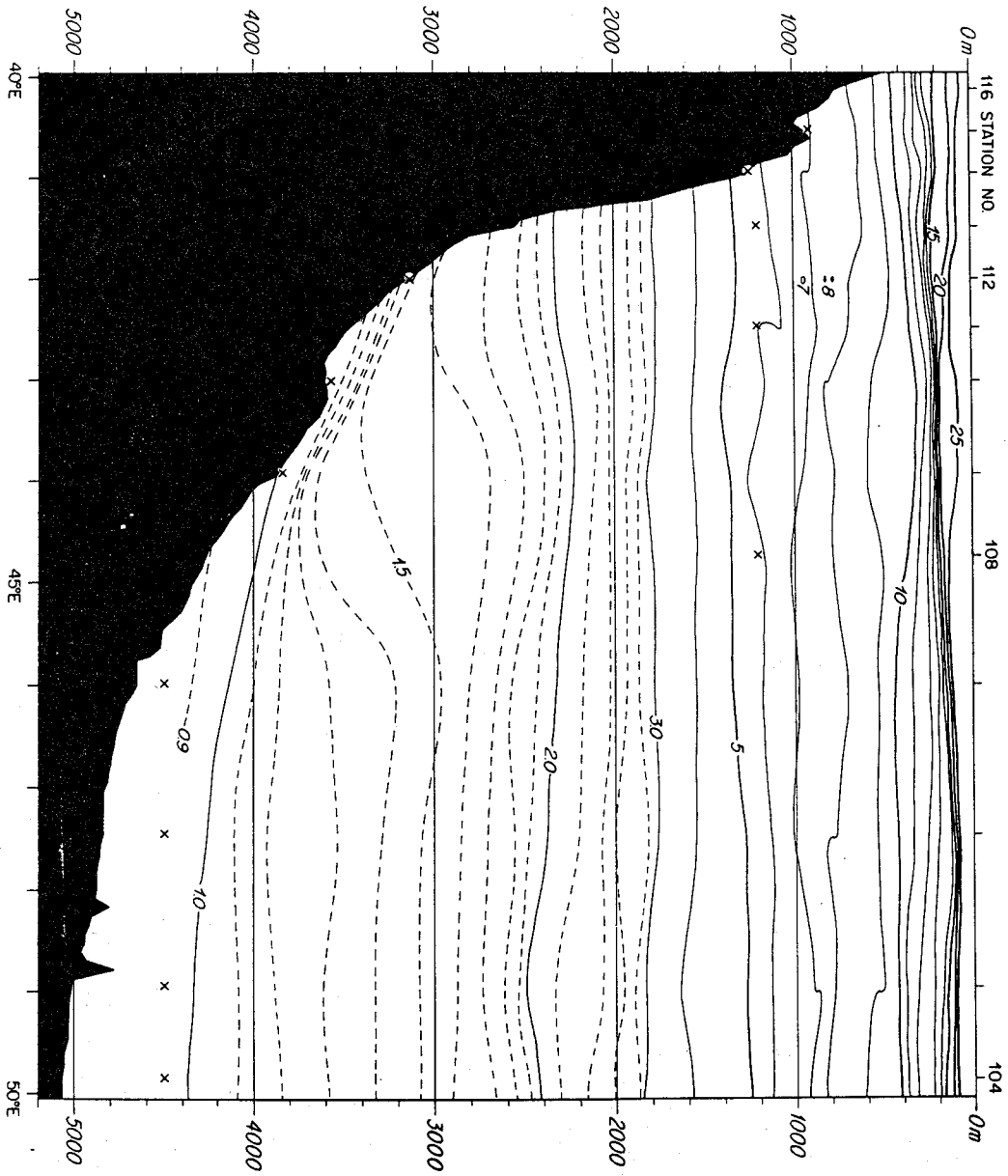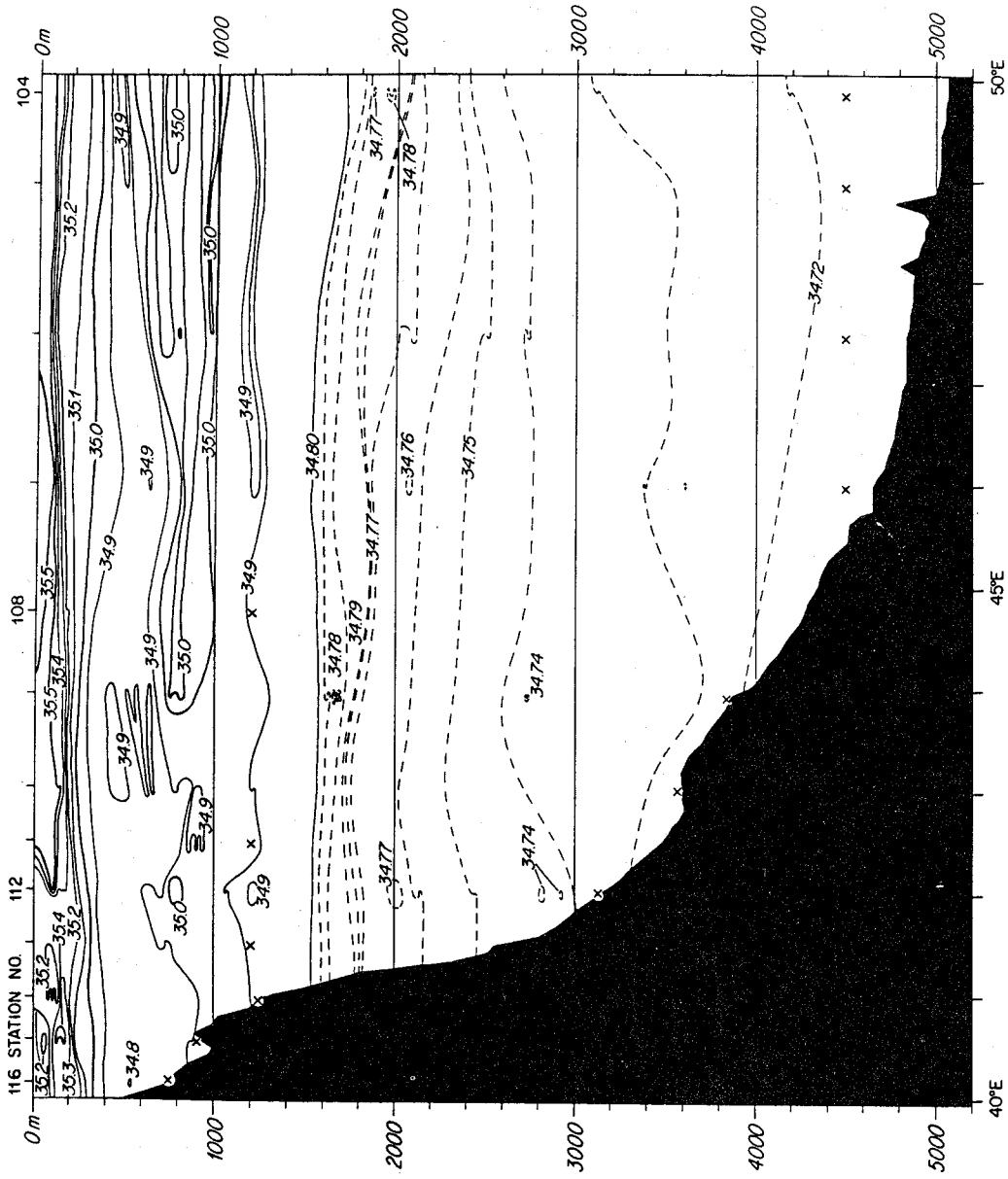
Figure A.2: Section profile of salinity S (psu) for the southern section of CD 86-19.

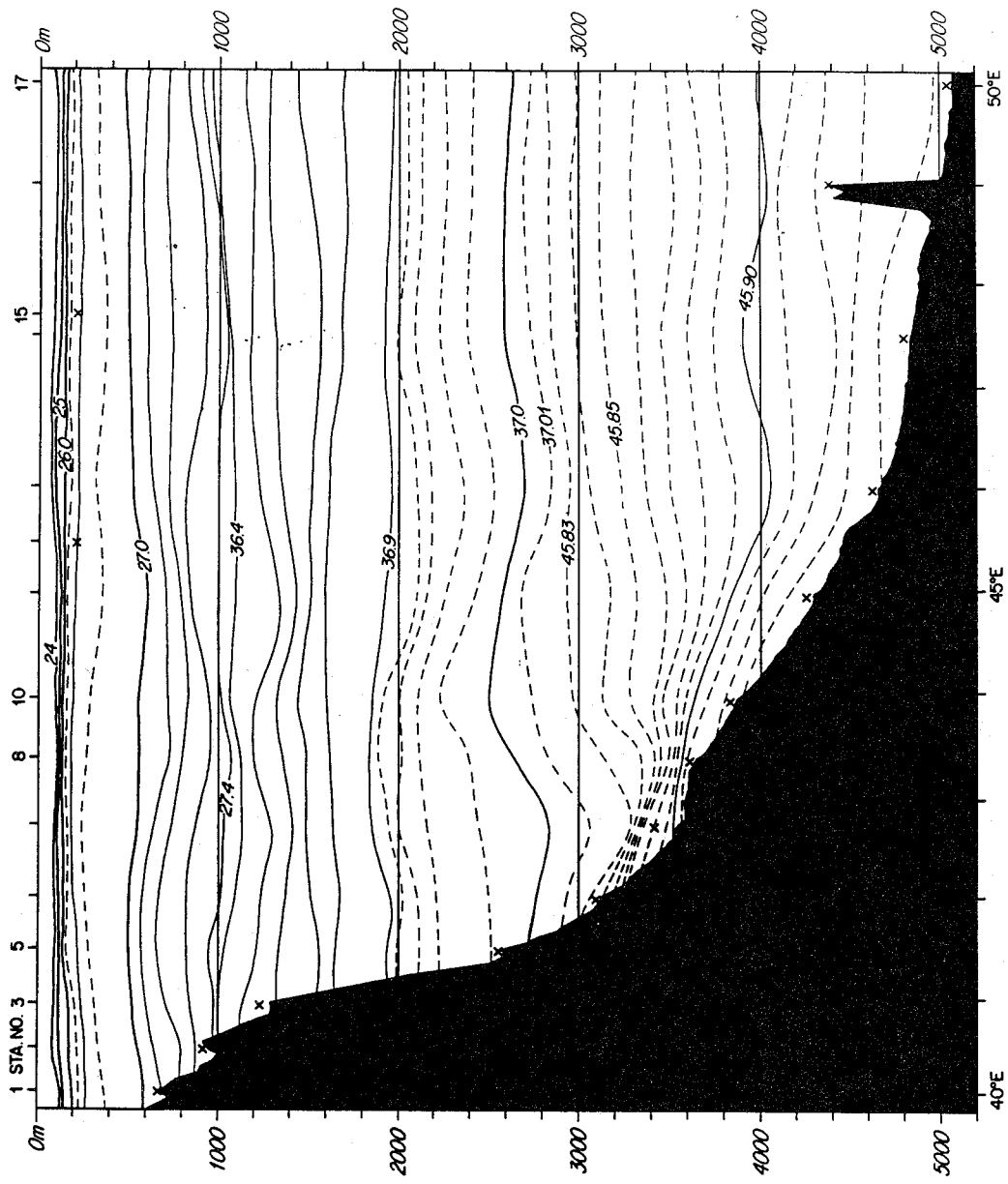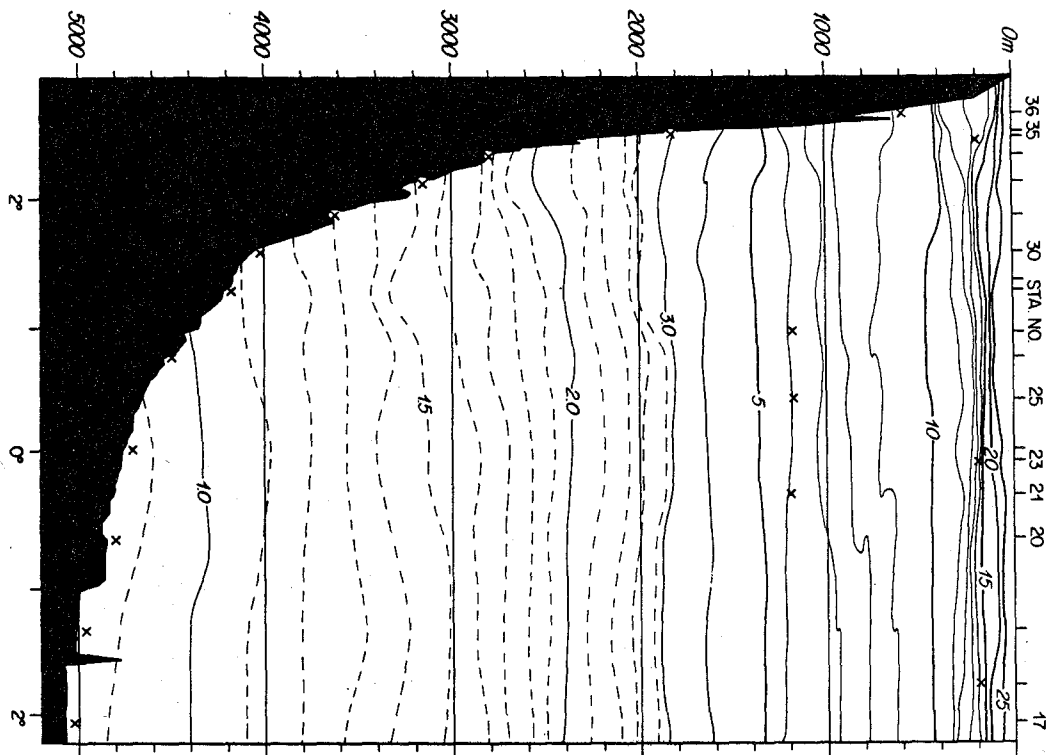Figure A.3: Section profile of dissolved oxygen concentration O_2 ($ml\ l^{-1}$) for the southern section of CD 86–19.
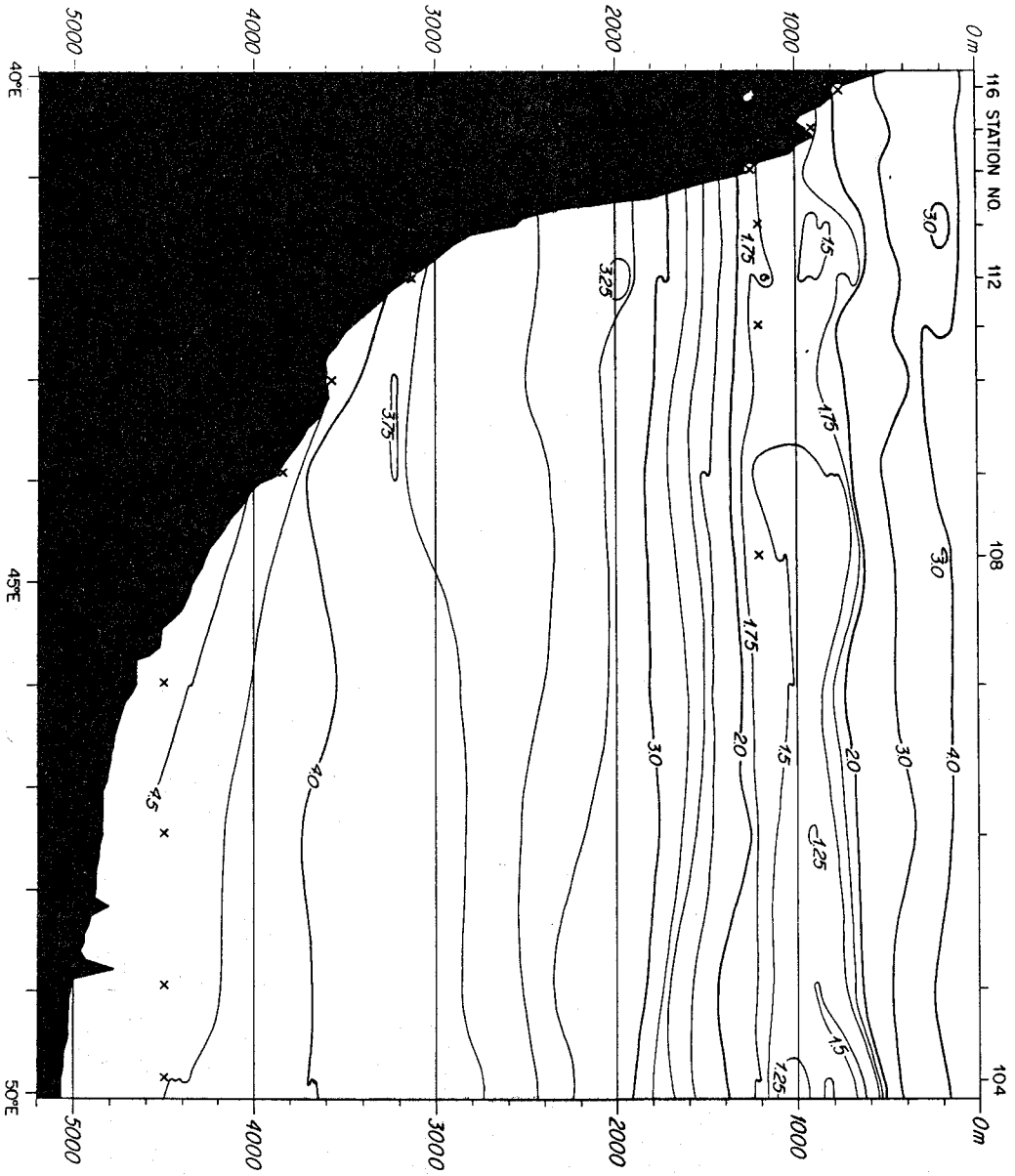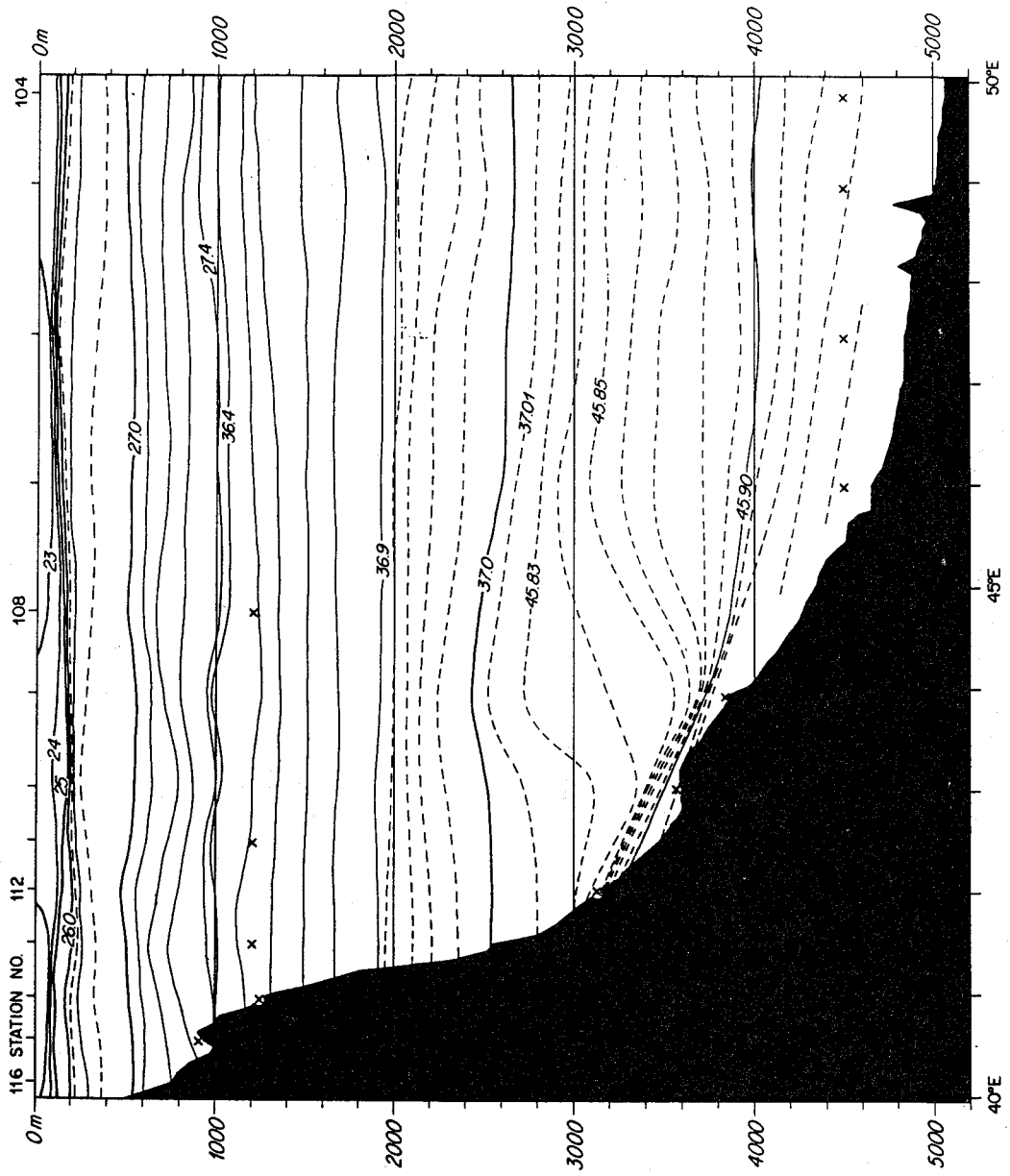
Figure A.4: Section profile of variably referenced potential density anomaly stacked-σ (kg m^{-3}) for the southern section of CD 86–19.

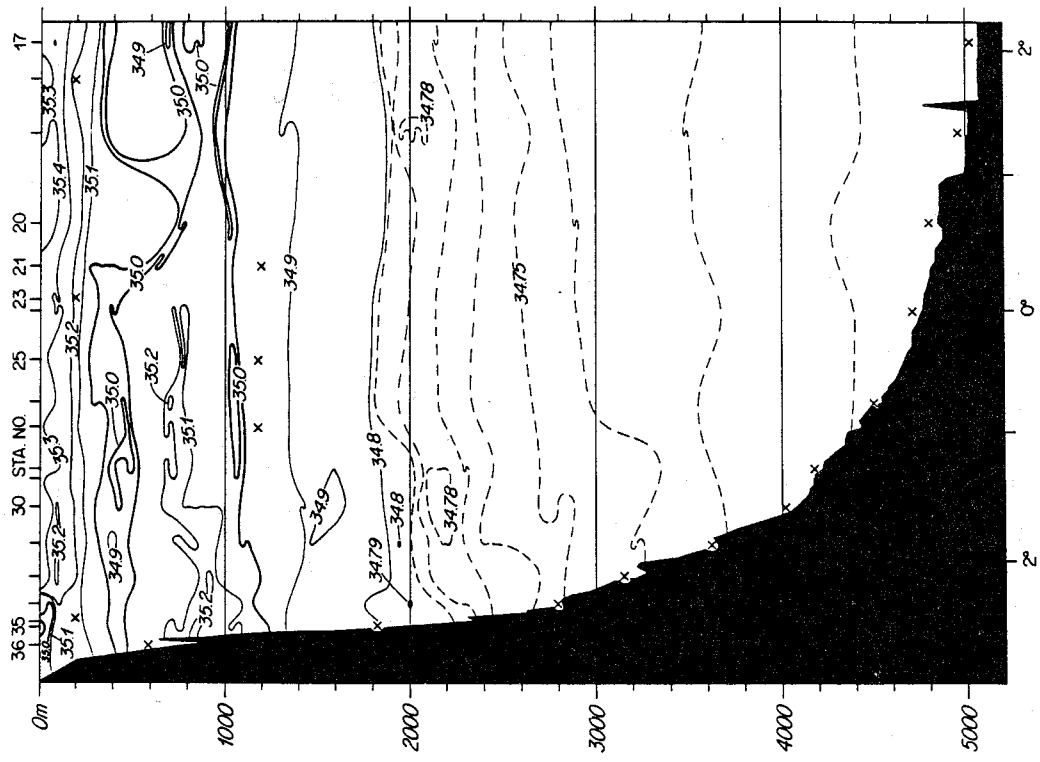Figure A.5: Section profile of potential temperature θ (degrees C) for the equatorial section of CD 86–19.
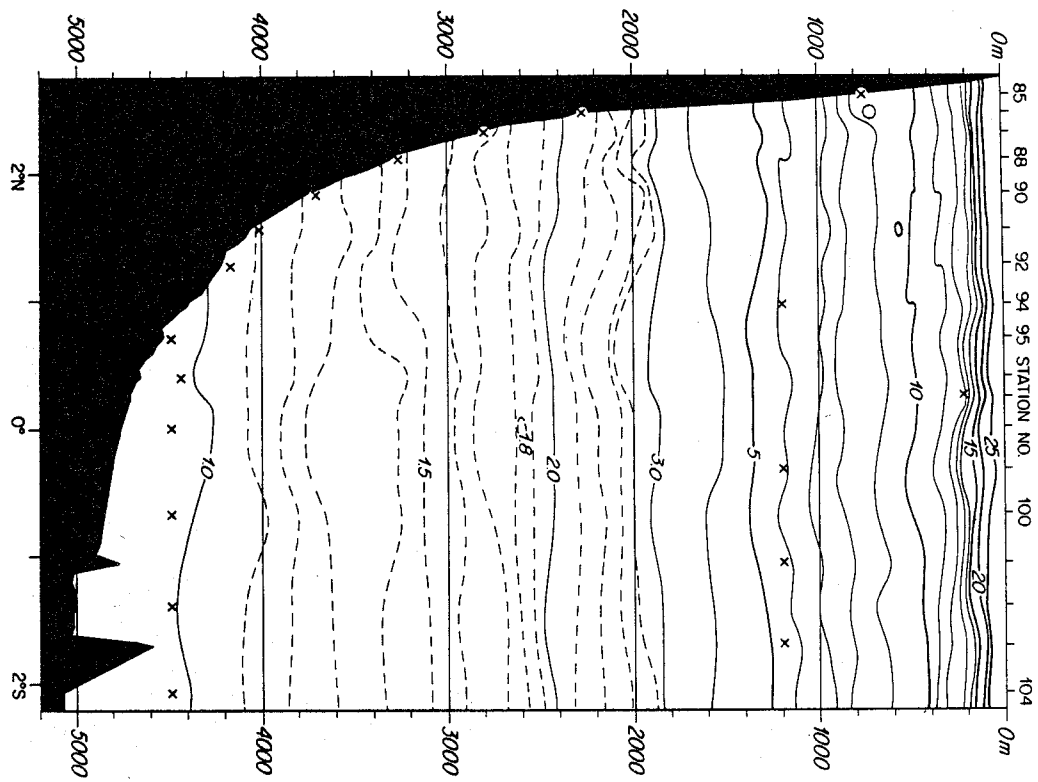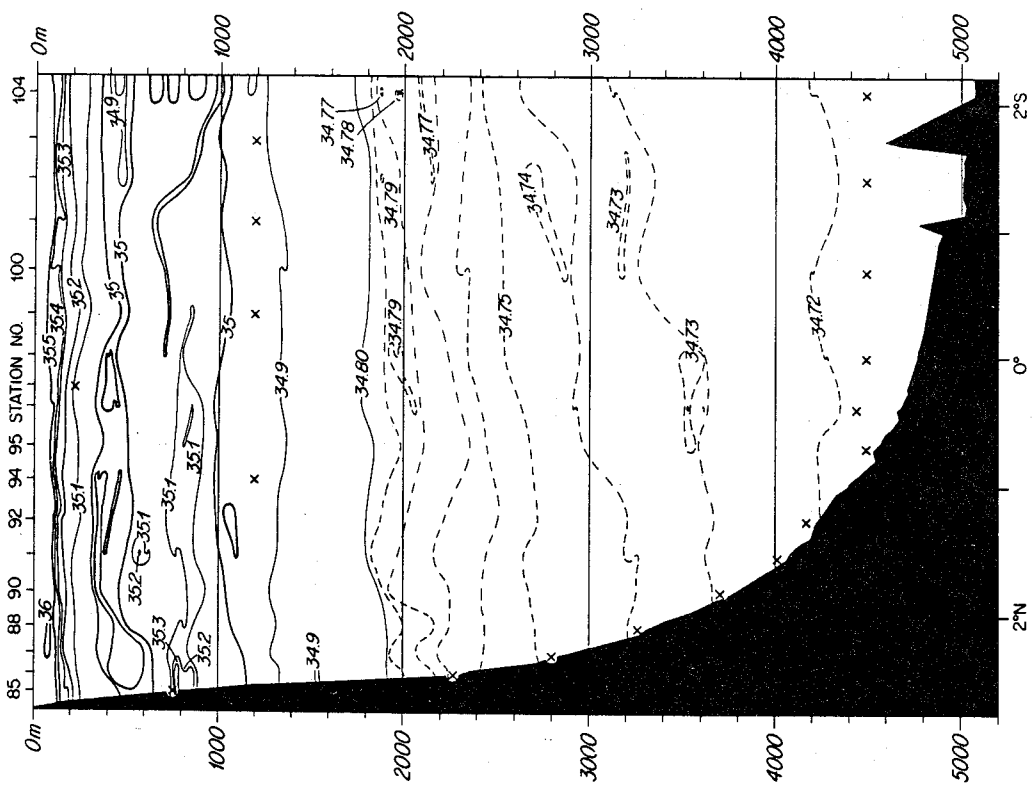
Figure A.6: Section profile of salinity S (psu) for the equatorial section of CD 86–19.

Figure A.7: Section profile of dissolved oxygen concentration O_2 ($ml\ l^{-1}$) for the equatorial section of CD 86–19.
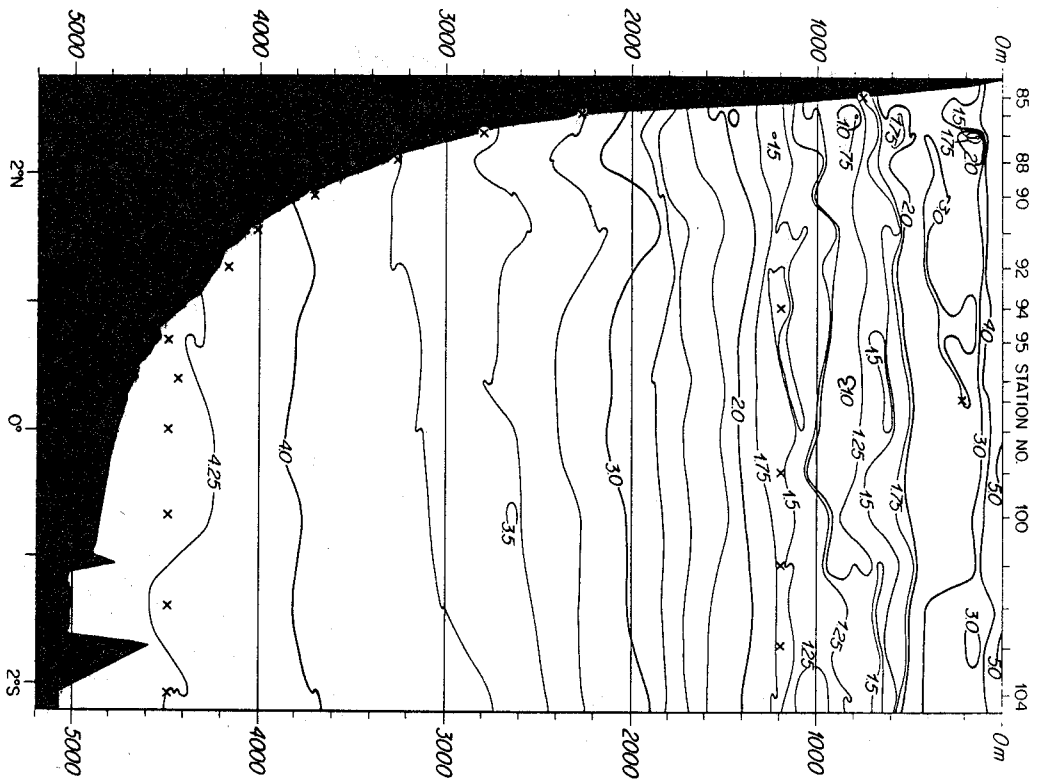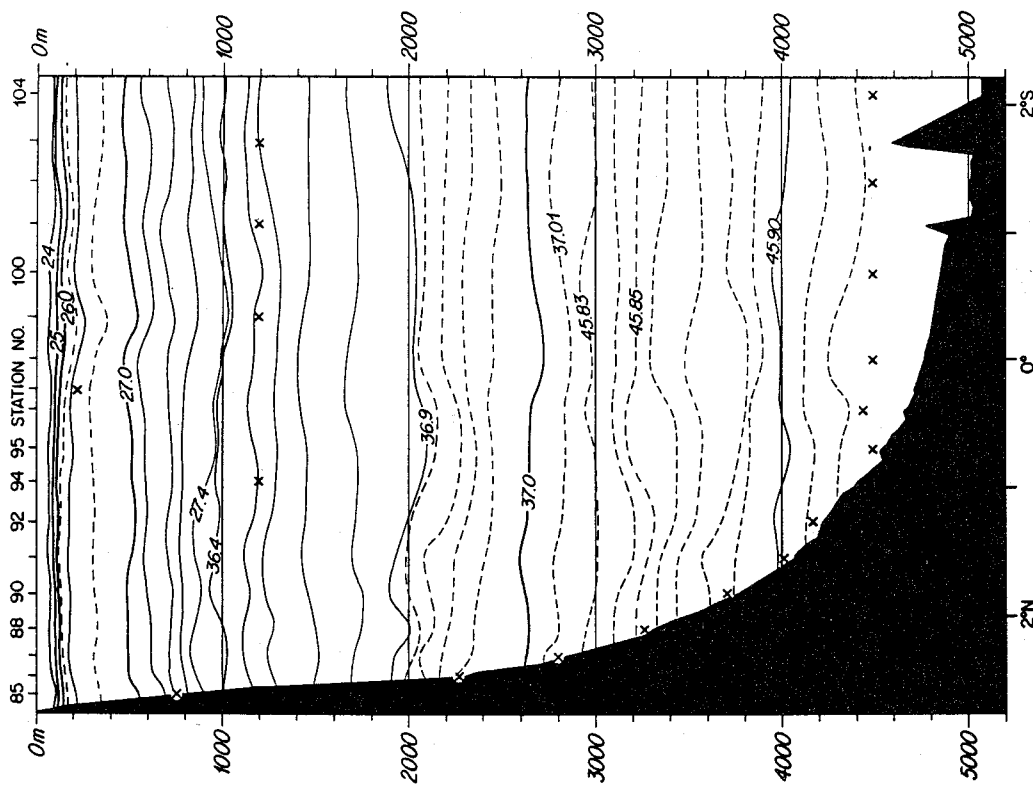
Figure A.8: Section profile of variably referenced potential density anomaly stacked-σ (kg m^{-3}) for the equatorial section of CD 86–19.

133

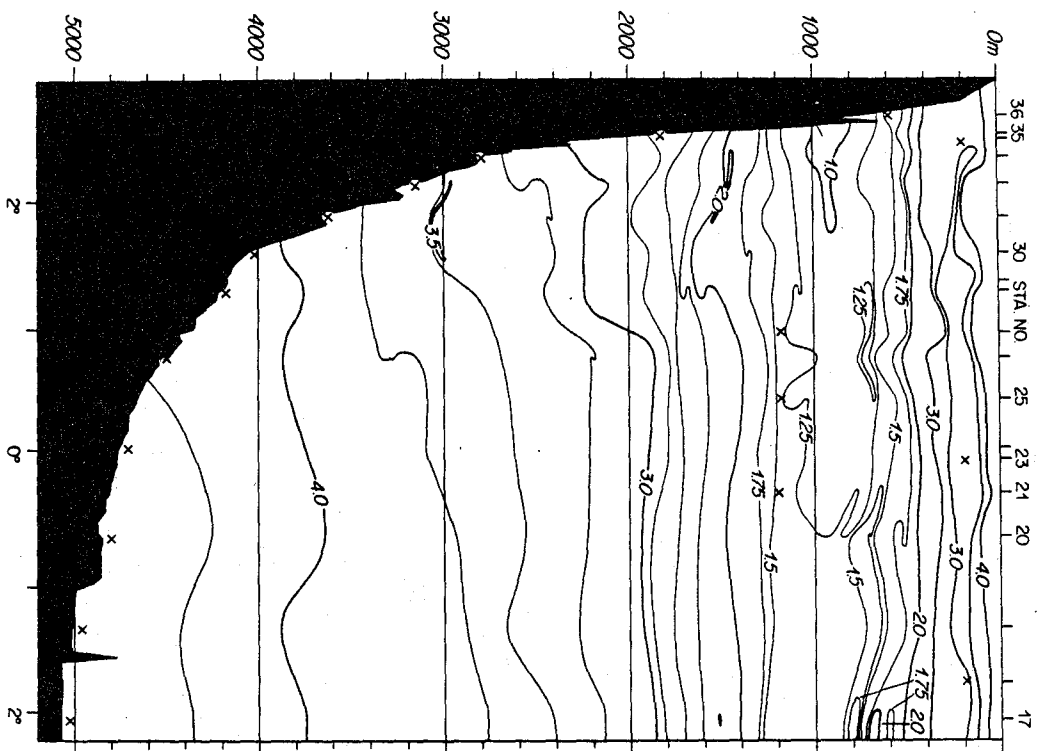Figure A.9: Section profile of potential temperature θ (degrees C) for the northern section of CD 86–19.
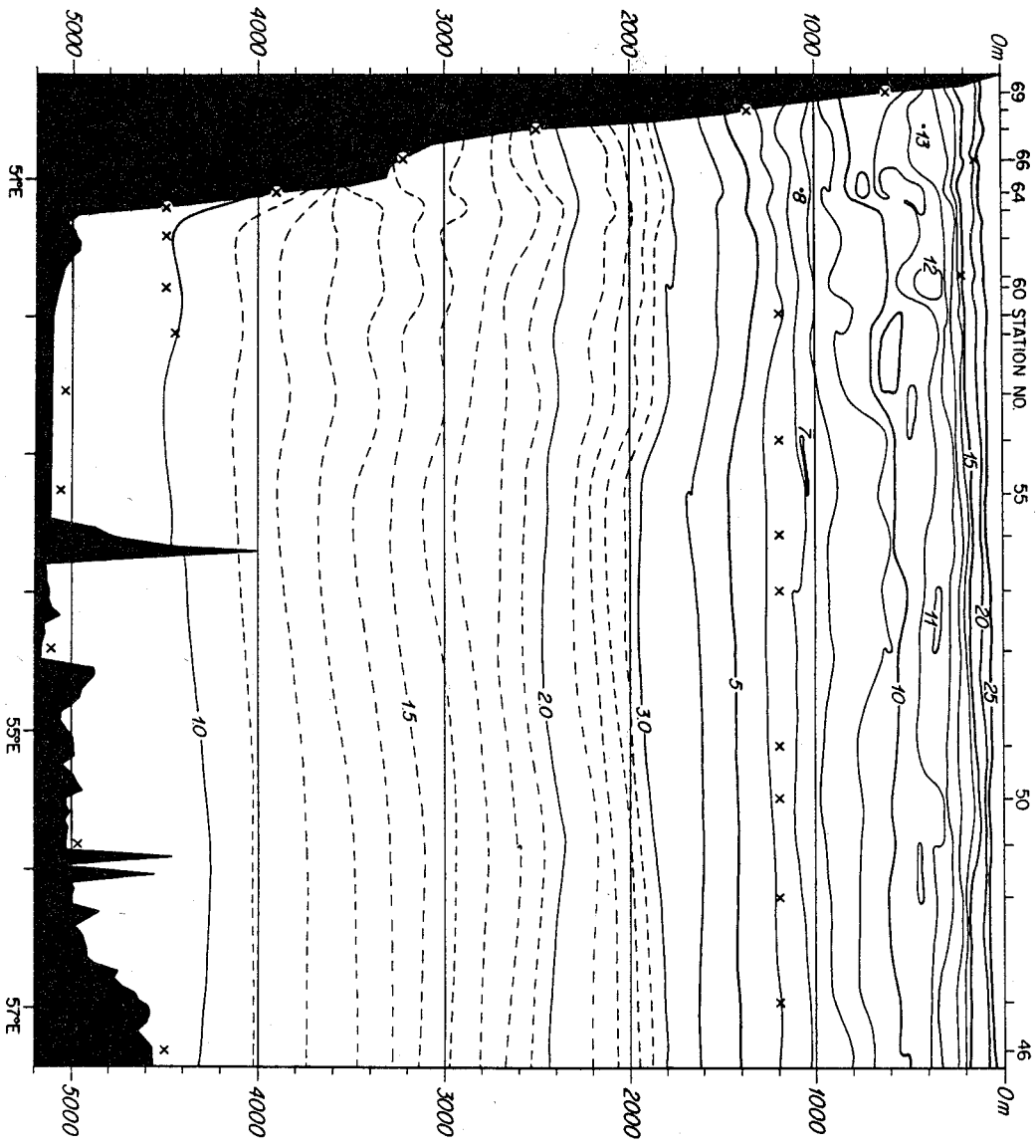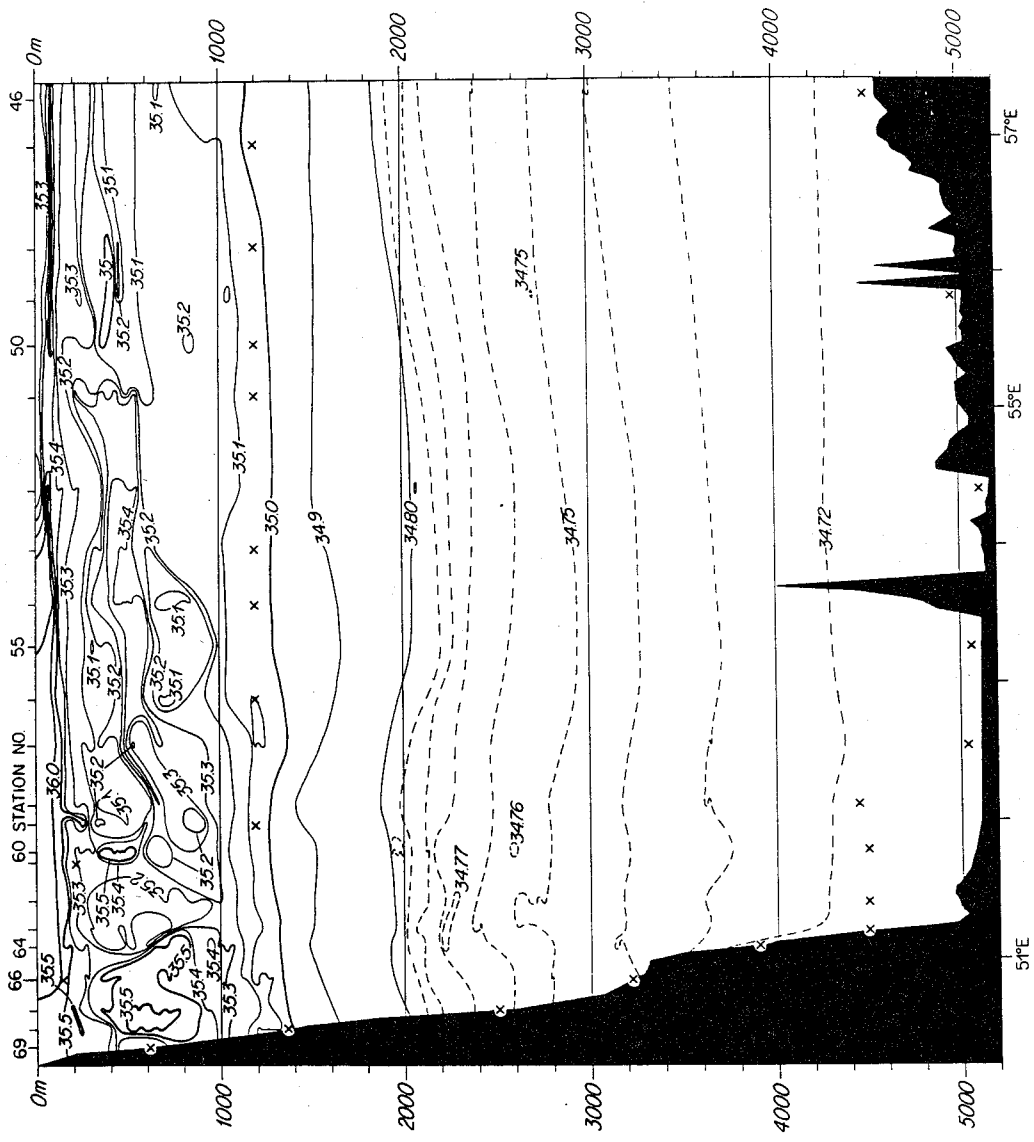
Figure A.10: Section profile of salinity S (psu) for the northern section of CD 86-19.

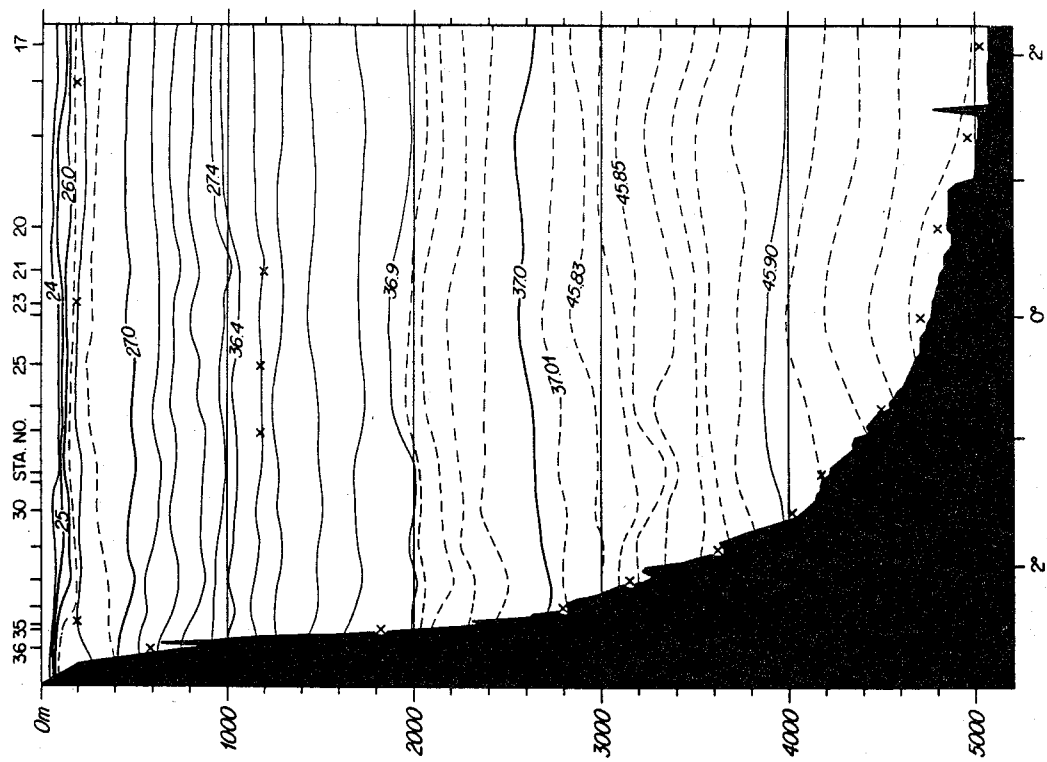Figure A.11: Section profile of dissolved oxygen concentration O_2 ($ml\ l^{-1}$) for the northern section of CD 86–19.
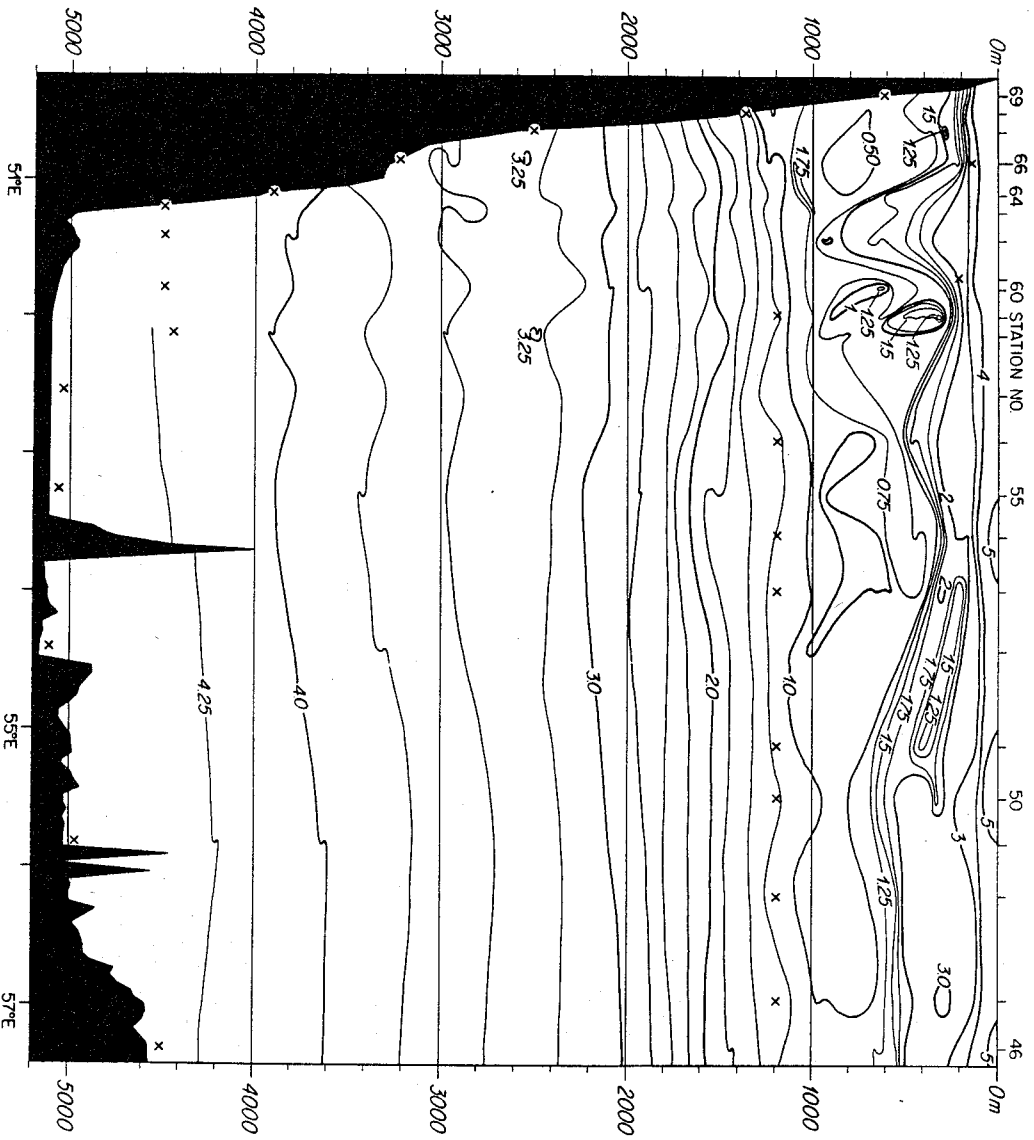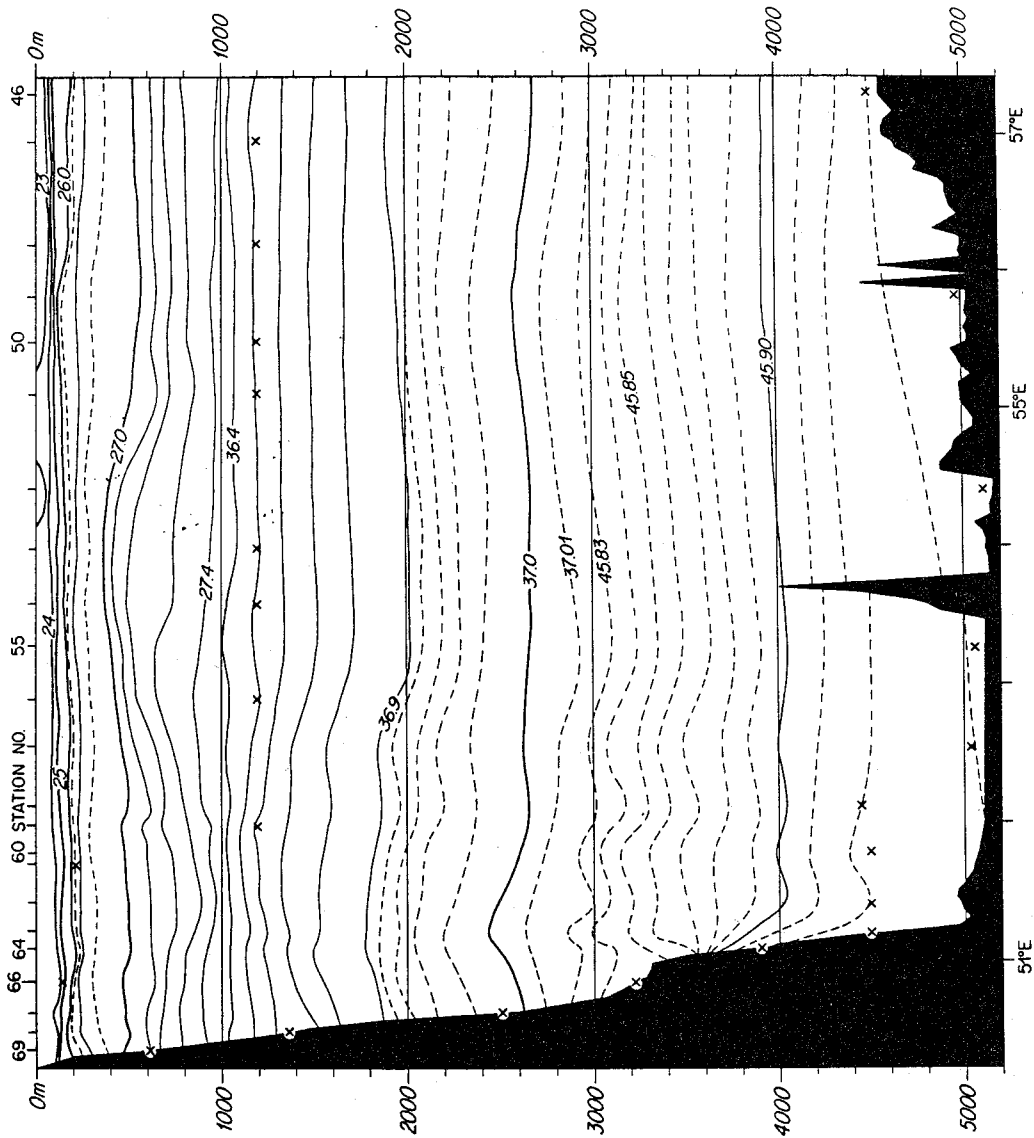
Figure A.12: Section profile of variably referenced potential density anomaly stacked-σ (kg m^{-3}) for the northern section of CD 86–19.

137

Figure A.13: Section profile of potential temperature θ (degrees C) for the Carlsberg Ridge section of CD 86-19.
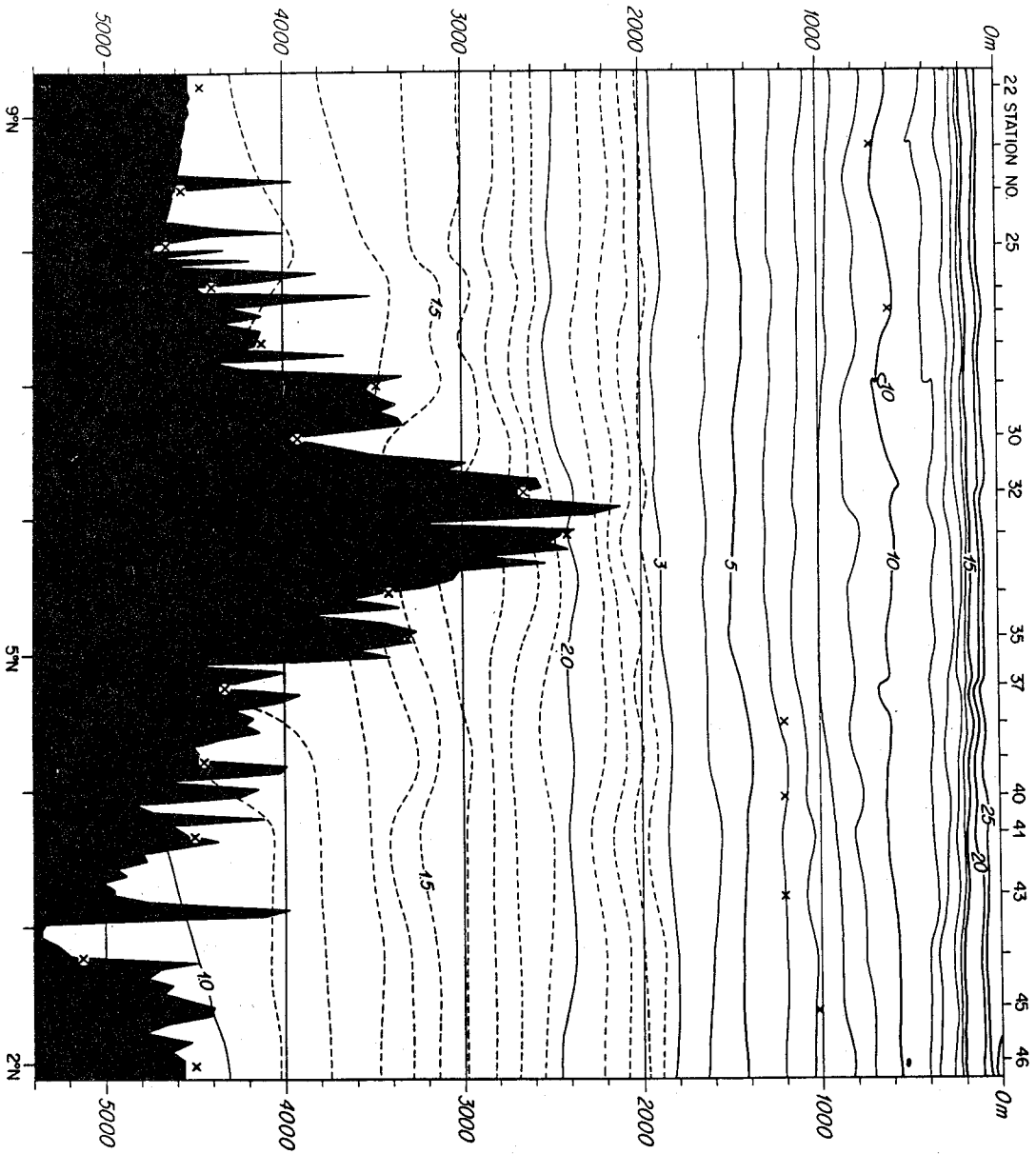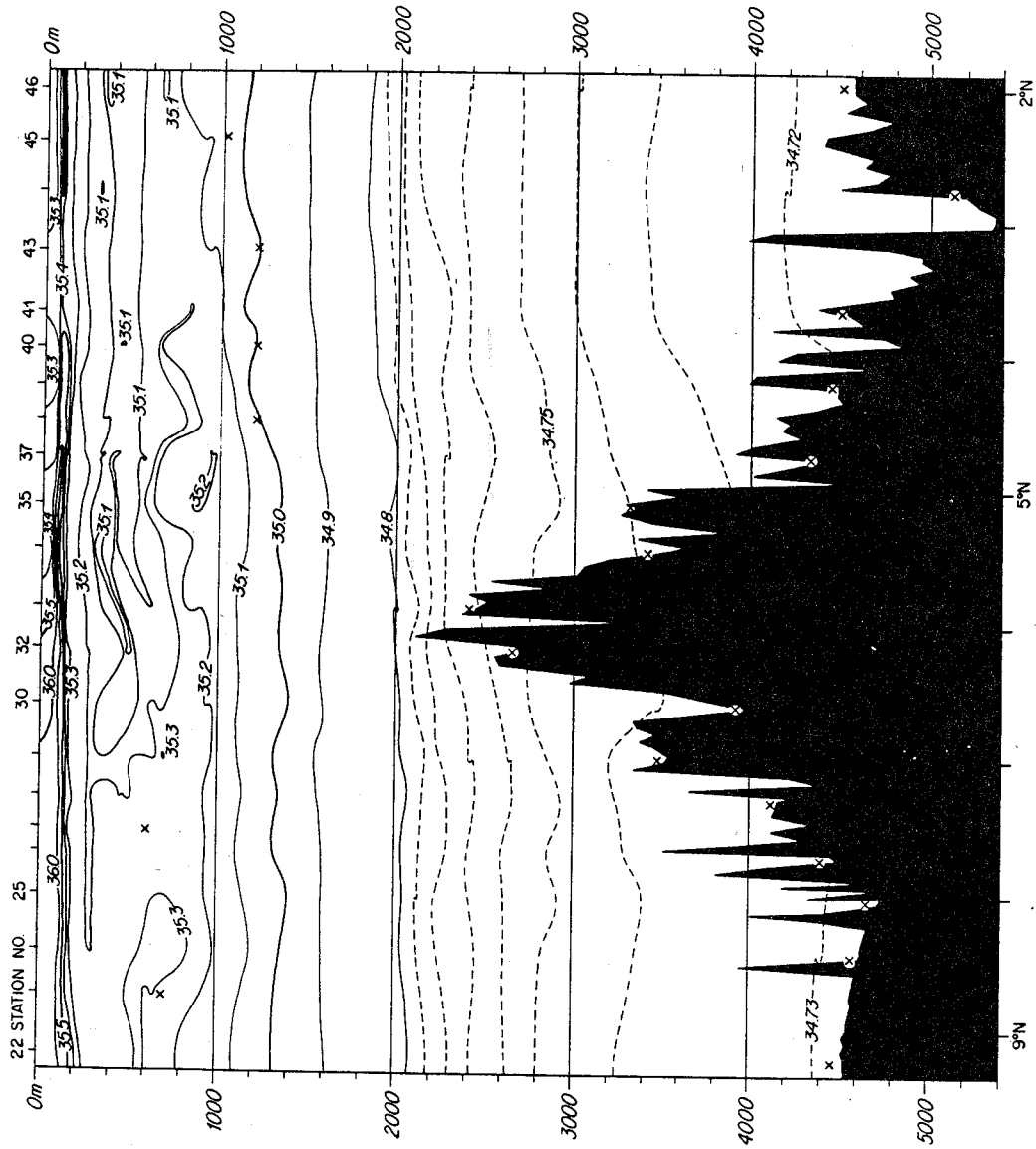
Figure A.14: Section profile of salinity S (psu) for the Carlsberg Ridge section of CD 86-19.

Figure A.15: Section profile of dissolved oxygen concentration O_2 ($ml\ l^{-1}$) for the Carlsberg Ridge section of CD 86–19.
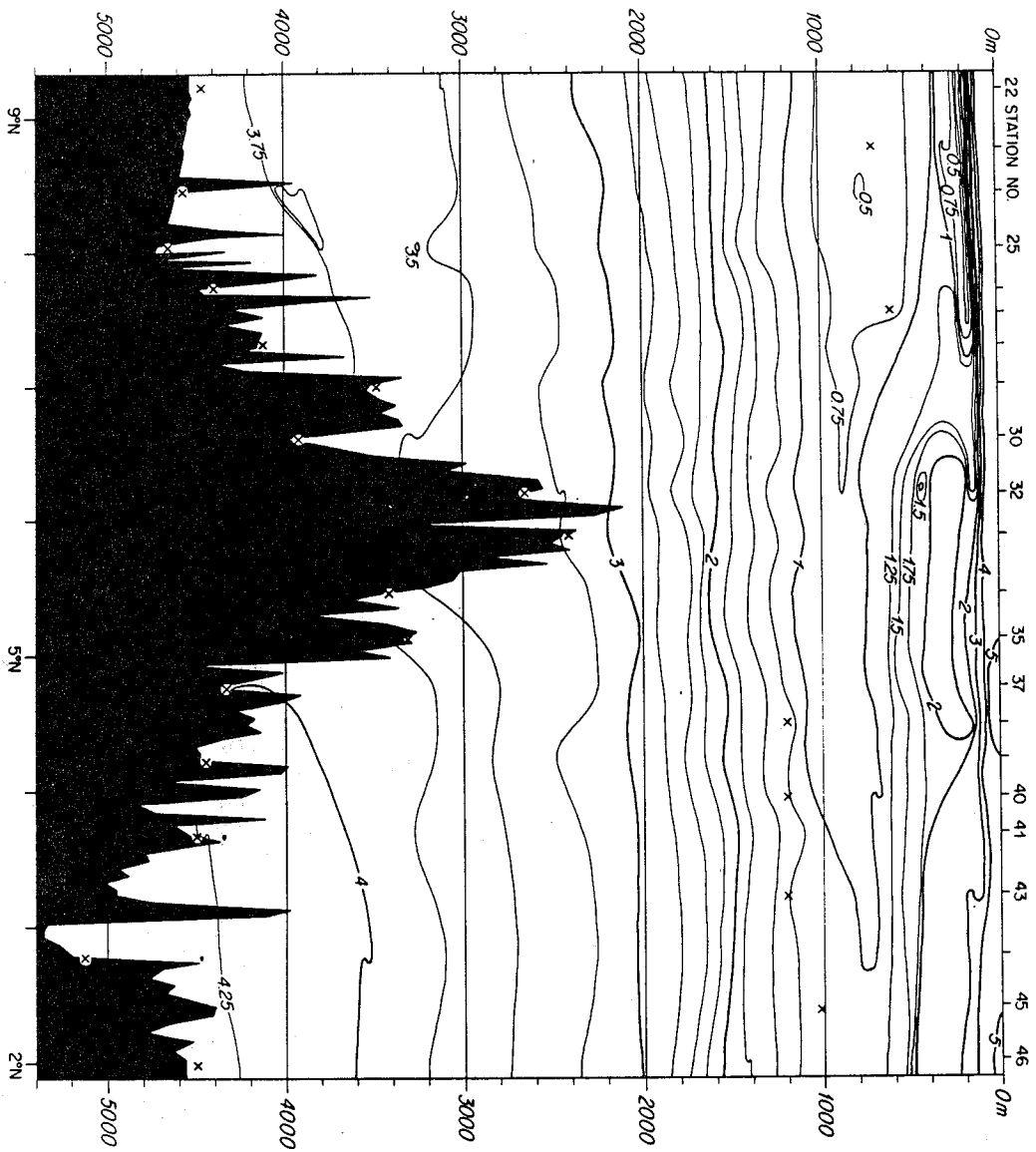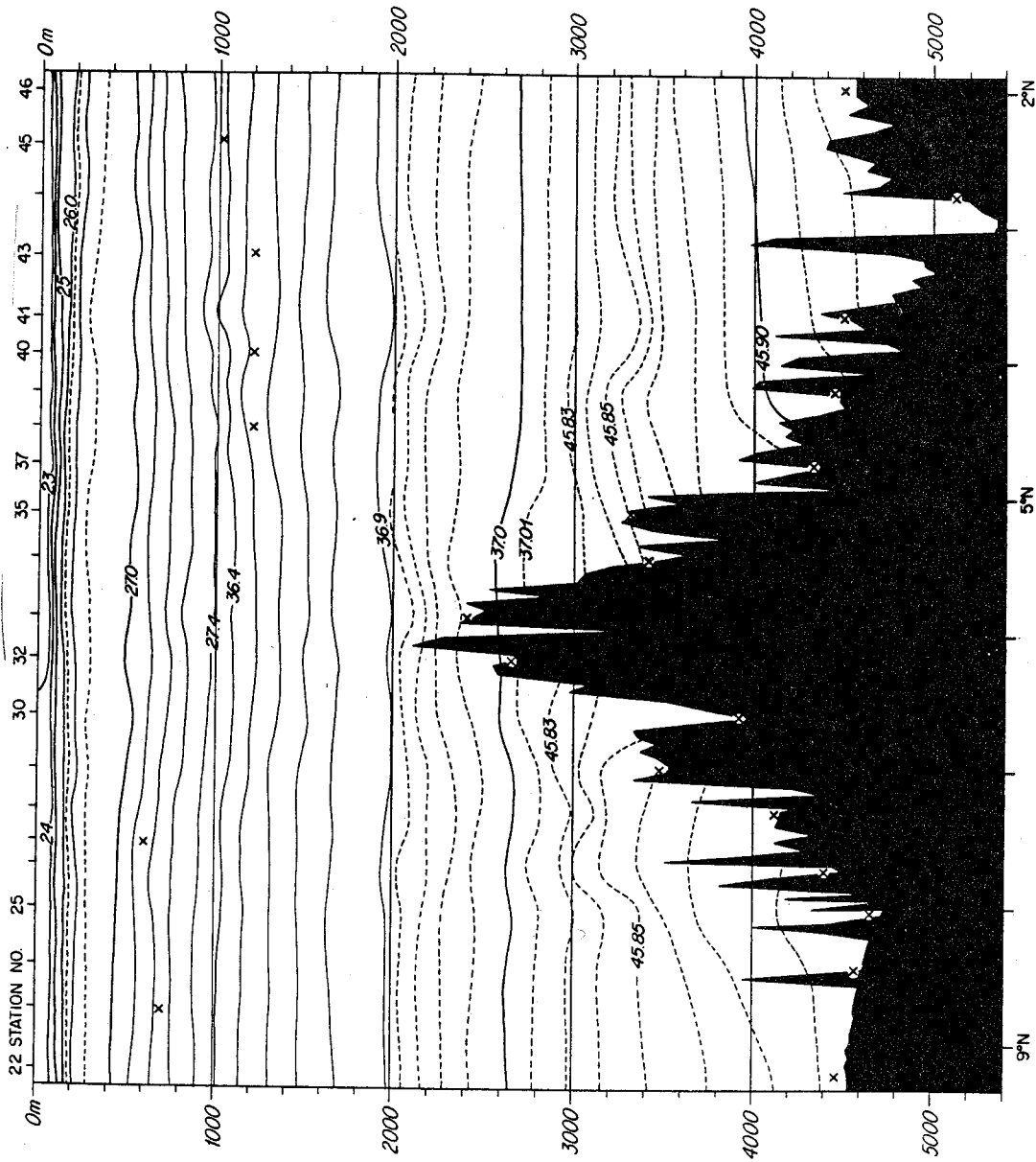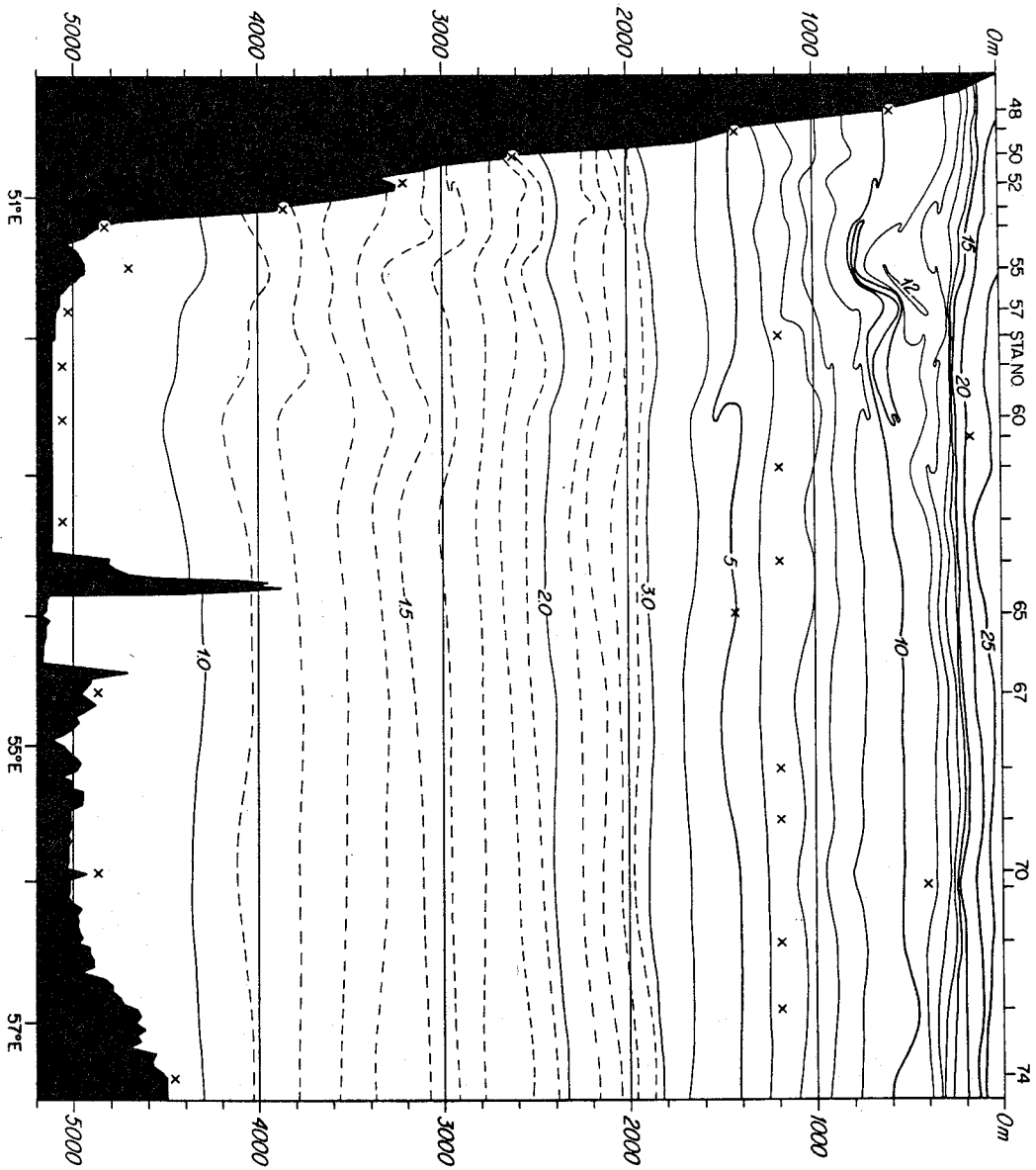
Figure A.16: Section profile of variably referenced potential density anomaly stacked-σ (kg m^{-3}) for the Carlsberg Ridge section of CD 86–19.

141

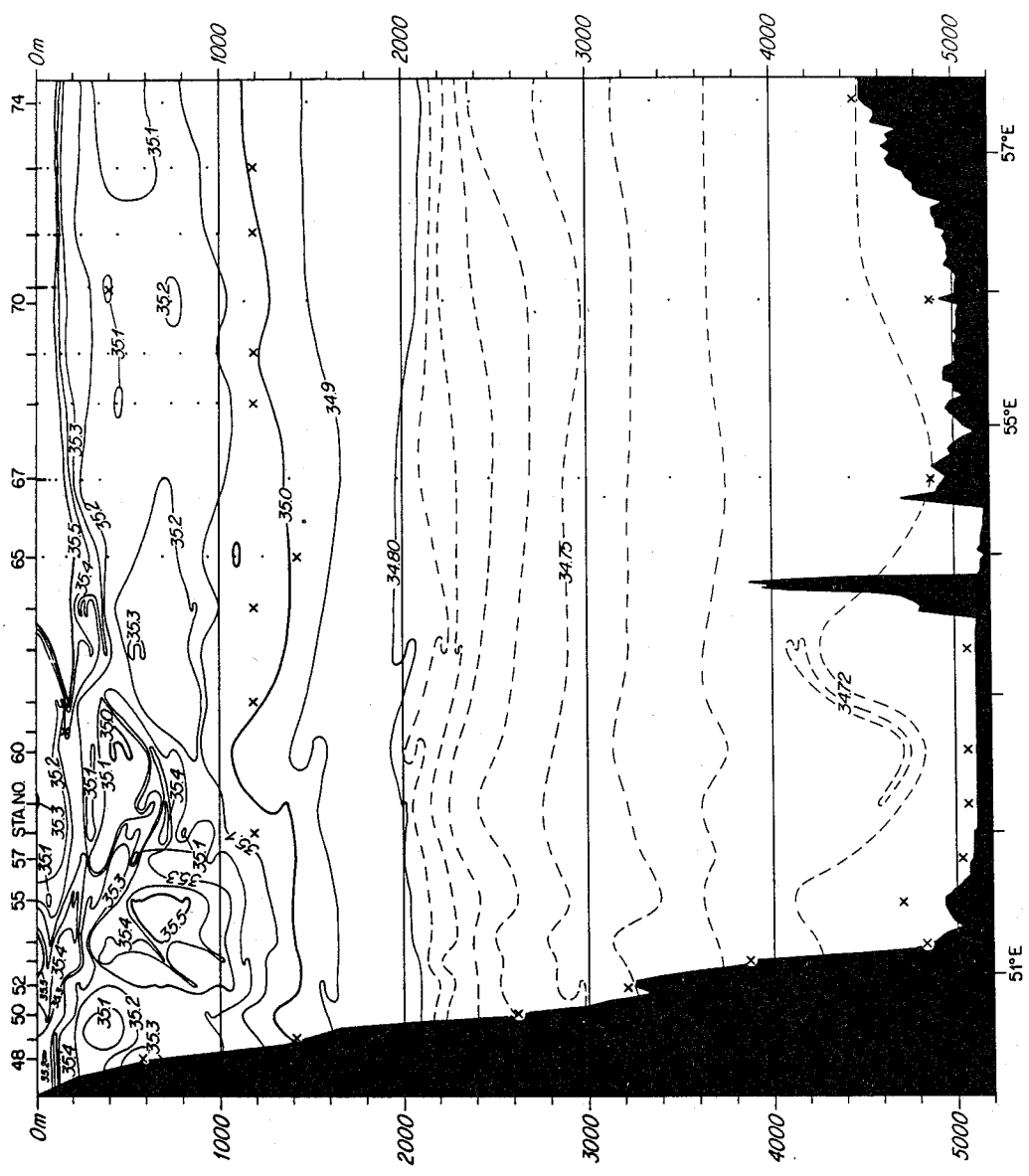Figure A.17: Section profile of potential temperature θ (degrees C) for the southern section of CD 87–25.
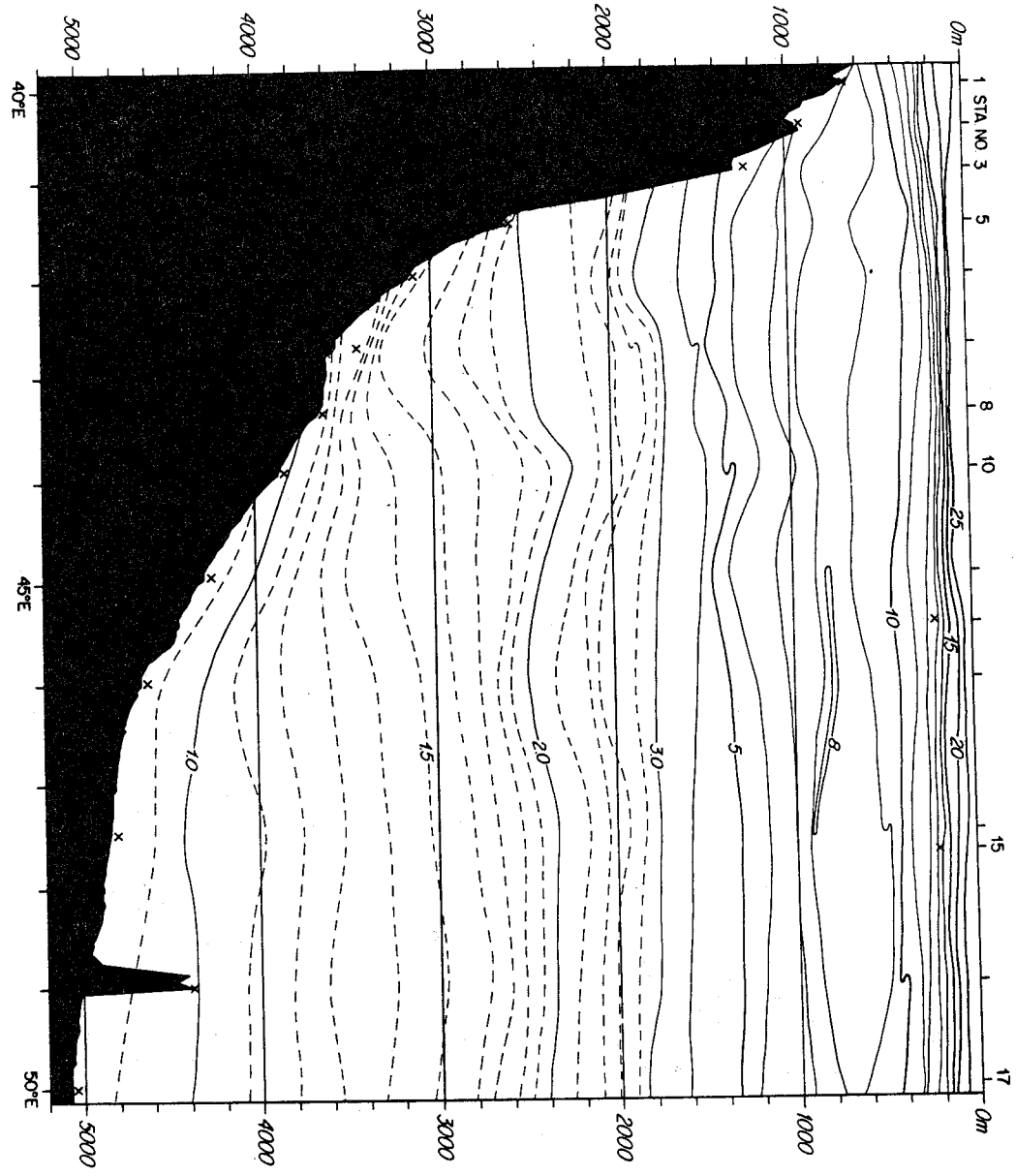
Figure A.18: Section profile of salinity S (psu) for the southern section of CD 87–25.

Figure A.19: Section profile of dissolved oxygen concentration O_2 ($ml\ l^{-1}$) for the southern section of CD 87–25.

Figure A.20: Section profile of variably referenced potential density anomaly stacked-σ (kg m^{-3}) for the southern section of CD 87-25.

Figure A.21: Section profile of potential temperature θ (degrees C) for the equatorial section of CD 87–25.
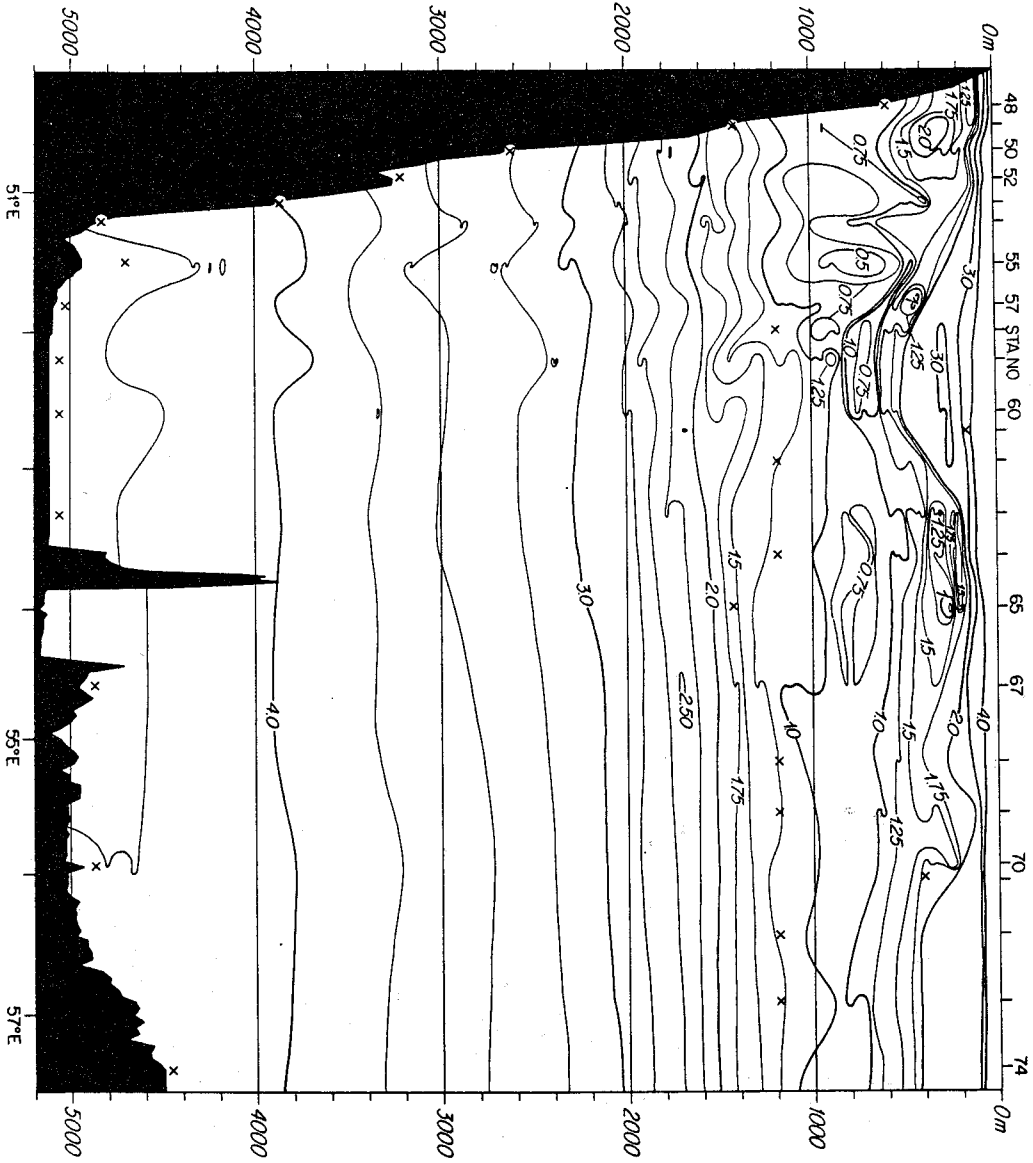
Figure A.22: Section profile of salinity S (psu) for the equatorial section of CD 87−25.

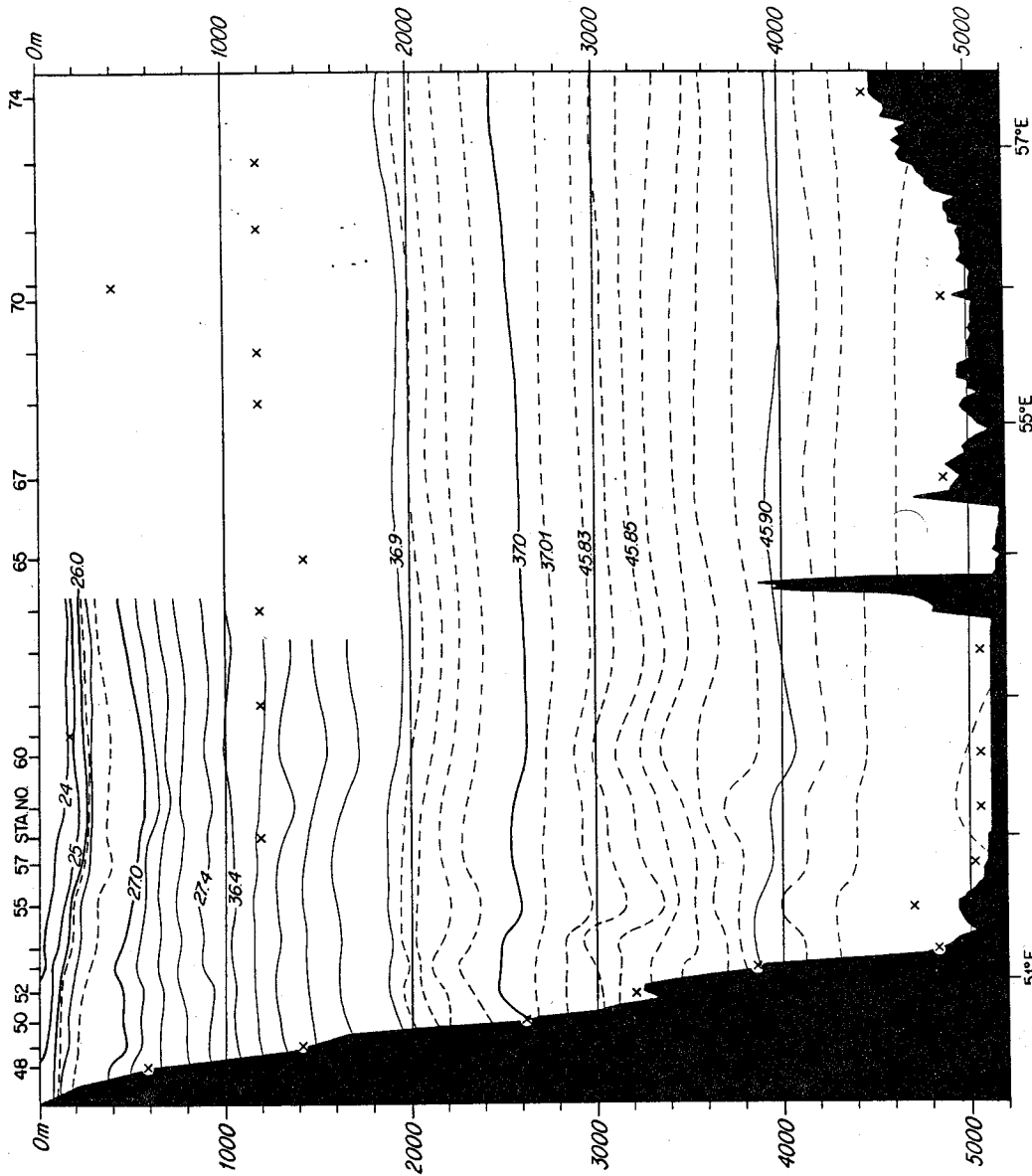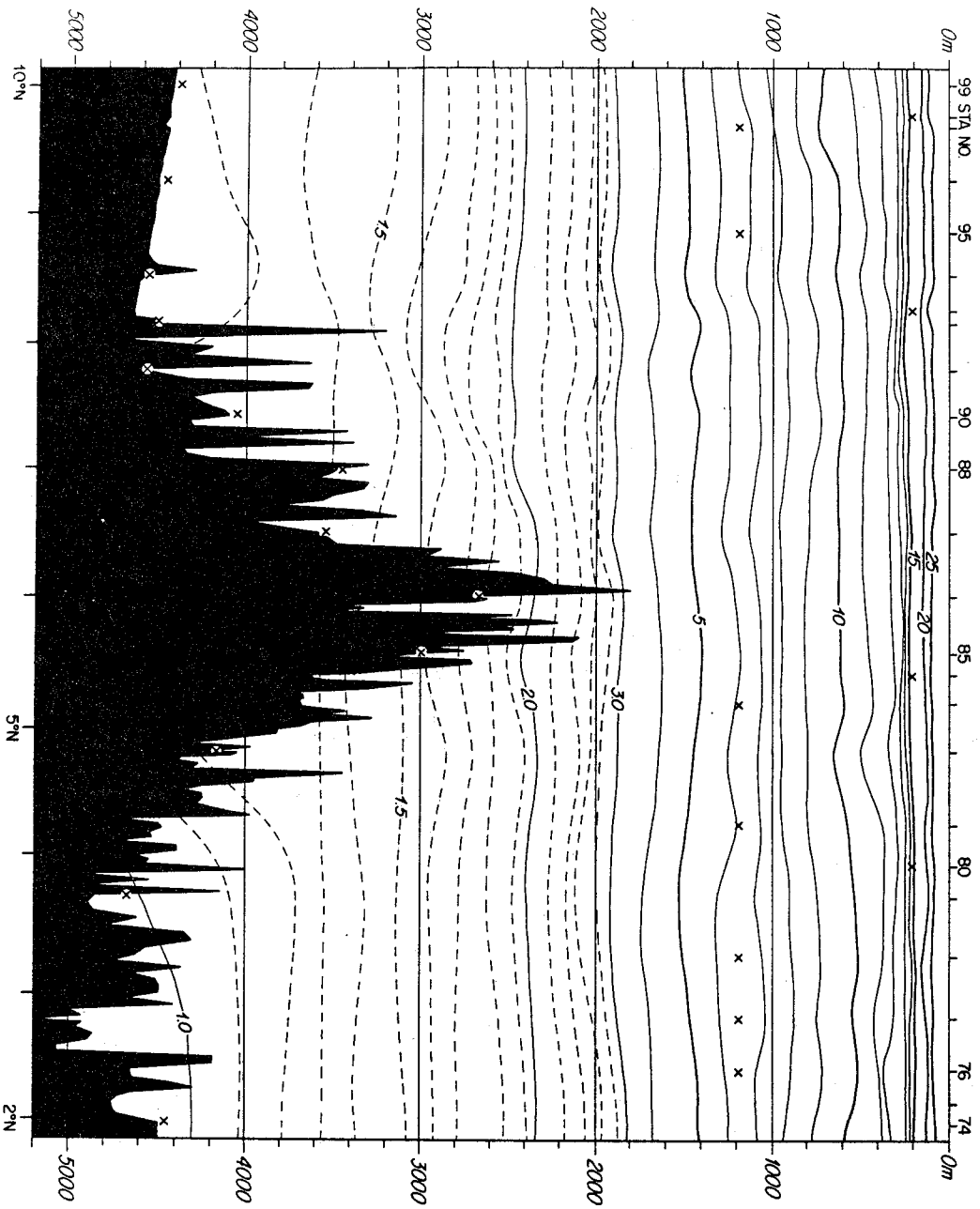Figure A.23: Section profile of dissolved oxygen concentration O_2 ($ml\ l^{-1}$) for the equatorial section of CD 87–25.

Figure A.24: Section profile of variably referenced potential density anomaly stacked−σ (kg m^{-3}) for the equatorial section of CD 87–25.

149

Figure A.25: Section profile of potential temperature θ (degrees C) for the northern section of CD 87–25.

Figure A.26: Section profile of salinity S (psu) for the northern section of CD 87–25. Dots indicate the use of bottle data after the conductivity cell on the CTD failed. Below T=3 the linear T–S relation is used to calculate the salinities. (See text).

151

Figure A.27: Section profile of dissolved oxygen concentration O_2 ($ml\ l^{-1}$) for the northern section of CD 87–25.

Figure A.28: Section profile of variably referenced potential density anomaly stacked-σ (kg m^{-3}) for the northern section of CD 87–25. The area not contoured lacks CTD salinity due to a conductivity cell failure. Below T=3 the linear T–S relation is used to calculate the potential densities. (See text).

Figure A.29: Section profile of potential temperature θ (degrees C) for the Carlsberg Ridge section of CD 87–25.
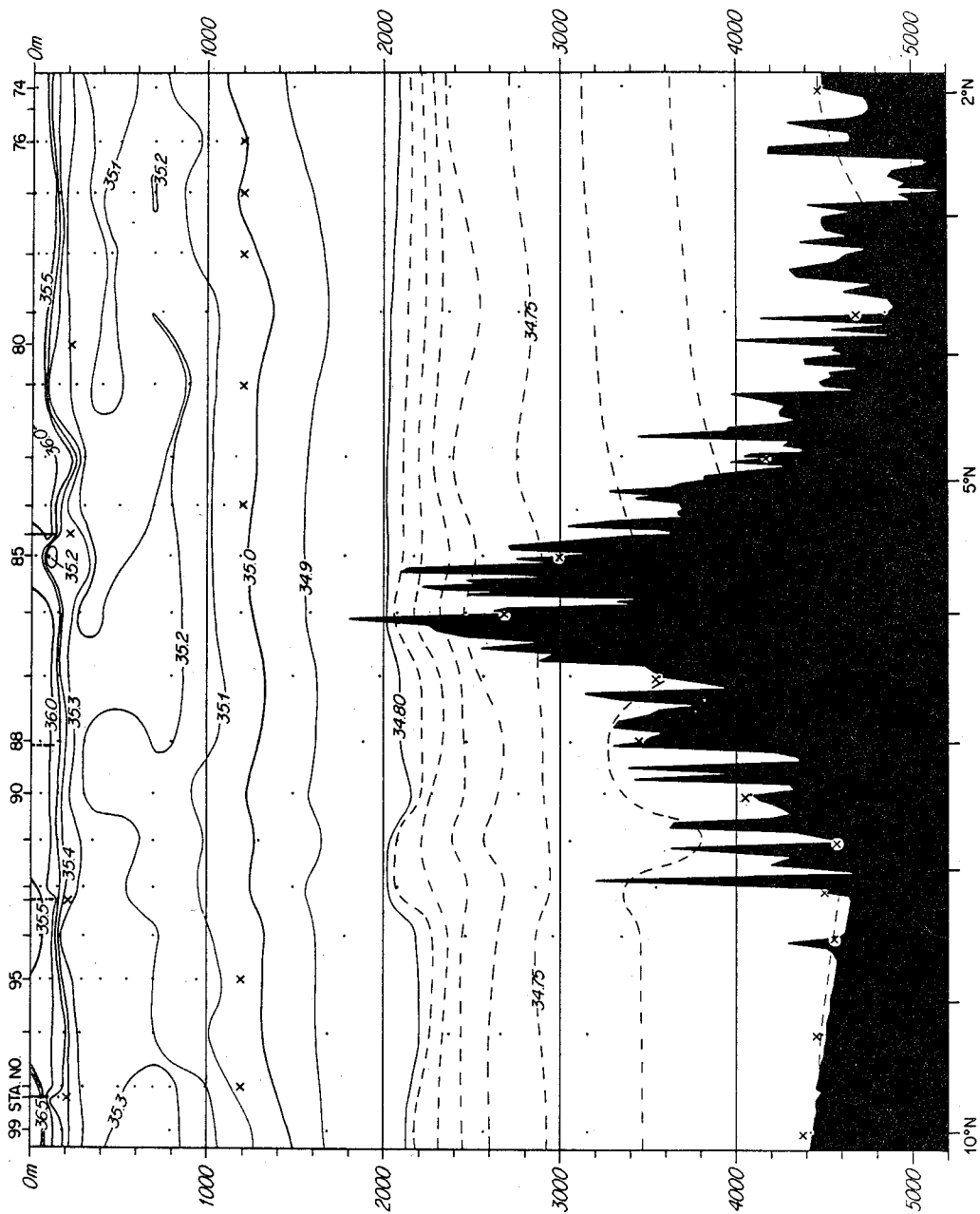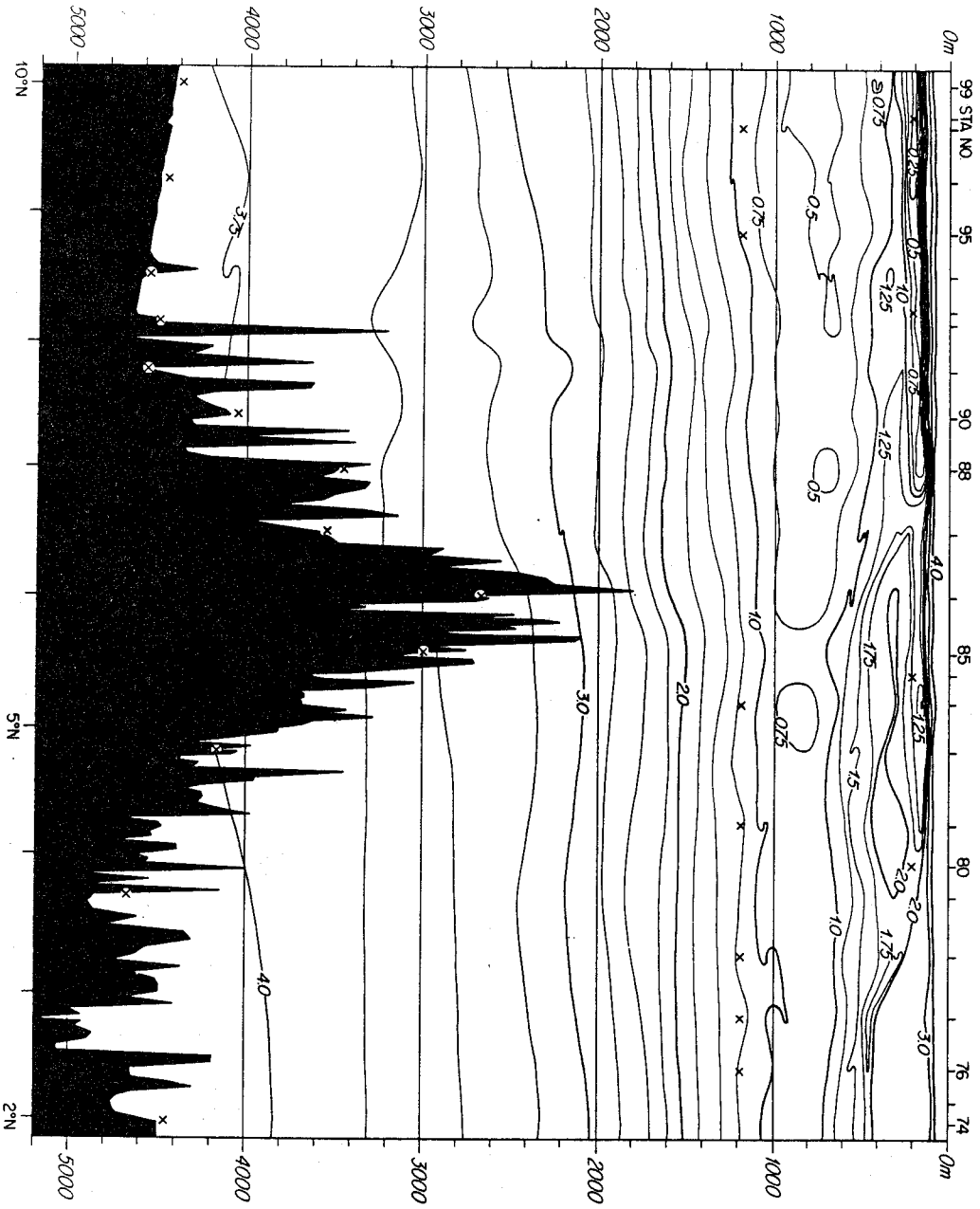
Figure A.30: Section profile of salinity S (psu) for the Carlsberg Ridge section of CD 87–25. Dots indicate the use of bottle data after the conductivity cell on the CTD failed. Below T=3 the linear T–S relation is used to calculate the salinities. (See text).

Figure A.31: Section profile of dissolved oxygen concentration O_2 (ml l^{-1}) for the Carlsberg Ridge section of CD 87–25.
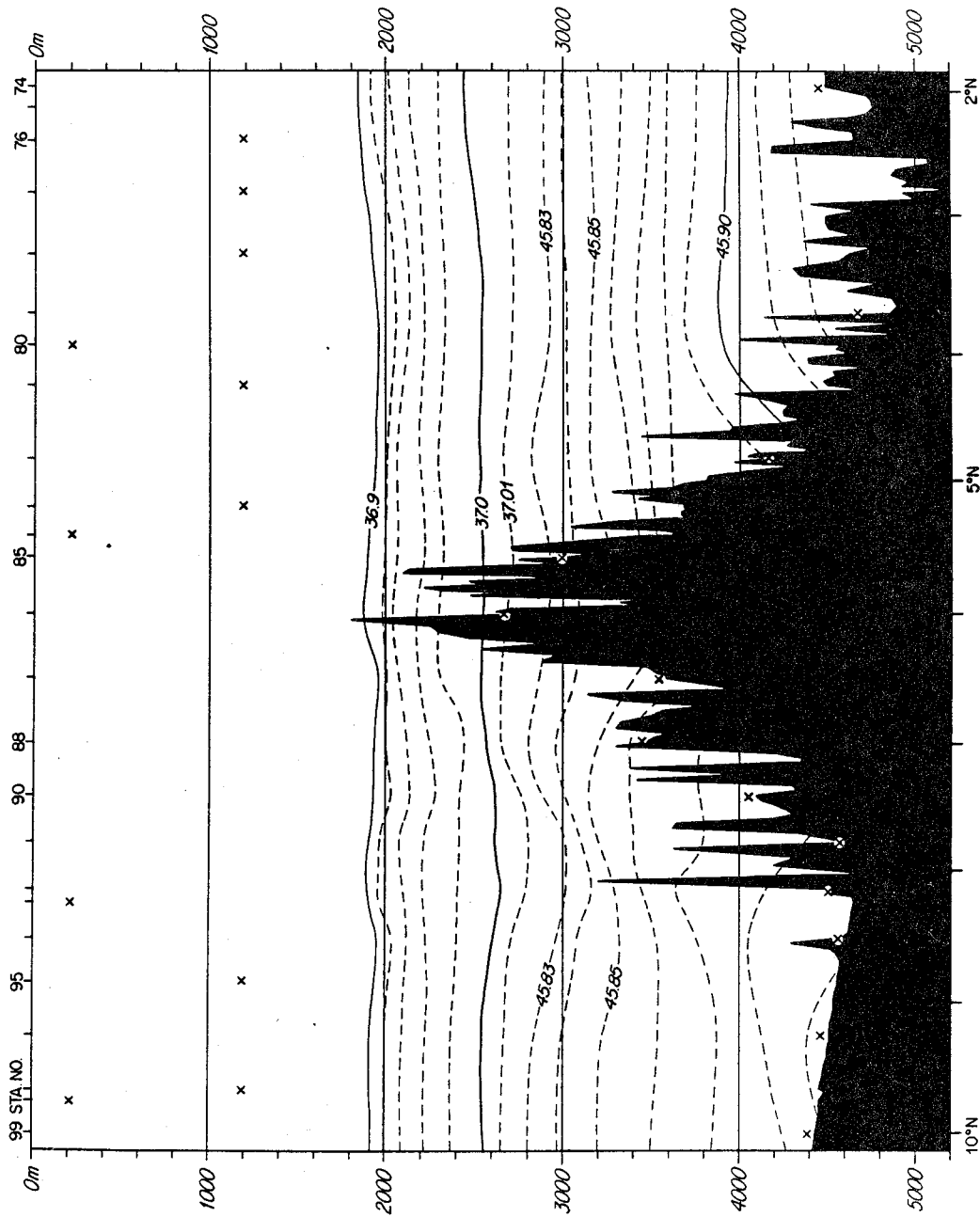
Figure A.32: Section profile of variably referenced potential density anomaly stacked-σ (kg m^{-3}) for the Carlsberg Ridge section of CD 87-25. The area not contoured lacks CTD salinity due to a conductivity cell failure. Below: T=3 the linear T–S relation is used to calculate the potential densities. (See text).